Study of Nitrogen-Brine Two-Phase Flow Behavior under High-Pressure Condition

A Thesis Submitted by

Naoto Shibata

For the degree's award of

Doctor of Philosophy

In Engineering

Division of Energy and Environmental System
Laboratory of Nuclear System Safety
February 2023
Supervised by Prof. Kazuhiro SAWA

Abstract

Gas-liquid two-phase flow, in which the mixture of gas and liquid flows, presents complex flow and heat transfer behavior due to the interactions at the gas-liquid interface. Its flow appears in many industrial systems including nuclear power plants. Furthermore, technological developments have led to the emergence of new industrial systems that handle unconventional gas-liquid two-phase flows, such as gas production from offshore methane hydrates and fusion reactors that utilize superconductivity. While these systems have the advantage of utilizing the knowledge of gas-liquid two-phase flow developed to date, they also pose new challenges arising from the novel system, and gas production from offshore methane hydrates is one of them.

Methane hydrates are the clathrate where methane dominates as a guest molecule. In recent years, these are drawing attention as an alternative to the existing natural energy source such as natural gas and oil. The Japan's Methane Hydrate R&D Program has developed a gas production method from marine gas hydrate, which is expected to deposit significantly in the offshore areas surrounding Japan. To date, the offshore methane hydrate production test has been conducted twice, with the successful gas production from marine gas hydrate using the depressurization method. This method produces gas by dissociating the hydrate through depressurizing the bottom-hole with extracting the liquid present inside the wellbore. With this procedure, the gas production rate highly depends on the bottom-hole pressure, thus, its control is crucial for the stable gas production. Also, assurance of production stability in the long term is necessary for the commercial use. In order to meet this demand, proper specification and design of downhole and control equipment such as gas-liquid separators, water pumps, etc., are essential to stabilize the bottom-hole pressure. To design these devices, determination of the process conditions is necessary considering the flow behavior in the wellbore. In general, there are several mechanistic models for estimating the process condition of wellbore used in the oil & gas industry. Hasan and Kabir model is one of them which can analyze the wellbore with the flow regime and pressure drop of the upward gas-liquid two-phase flow. The pressure drop of internal flow is comprised of gravitational, frictional and acceleration component and the fundamental knowledges are adequate for the oil & gas use, but are few for new application such as the methane hydrates. Thus, the present study has conducted the foundation of nitrogen-brine two-phase flow behavior under low and high-pressure to estimate the process condition using the conventional model. This study includes (1) void fraction and frictional pressure drop model as the foundation study of gas-liquid two phase flow and (2) objective flow regime identification method using machine learning technique.

The experiment is performed with the test facility comprised of the 28 m long test section whose inner diameter of 52.7 mm at low and 2.8 MPaG. In order to obtain the sequential image of the flow regime, high-speed cameras were used. The void fraction and pressure drop were measured with

gamma-ray densitometers and differential pressure.

As the foundation study of gas-liquid two phase flow in chapter 2, the models for the void fraction and frictional pressure drop were derived with non-dimensionalized drift-flux model and two-phase friction multiplier of separate flow model utilizing the of experimental results. The gas velocity of bubbly flow showed good correlation with the existing model under tap water, but was lower for all regions under brine. With the inhibition of coalescence by brine, the gas velocity is lower because of the uniformity of bubble distribution and lower bubble rise velocity due to the reduction in bubble diameter. The frictional pressure drop estimated from the experiment were in good correlation with tap water and the two-phase flow friction multiplier increases with elevated height, while decreases with increased system pressure.

As the study of objective flow regime identification in chapter 3 and 4, the identification method utilizing machine learning technique trained or input with experimental data was established and used to quantify the flow regime. The results in the transition region have quantitatively shown that the transition region exists for the bubbly to slug flow and were in good agreement with Mishima-Ishii's flow regime transition criteria.

With these findings, nitrogen-brine two-phase flow behavior under low and high-pressure has partially found and established the baseline for stimulating the process conditions that reflects the flow behavior in the wellbore. Hence, the present study will contribute to not only the stable gas production through the proper specification and design of downhole and control equipment, but also to the progress of Multiphase flow engineering and to the design of many industrial systems including nuclear power plants.

Acknowledgments

The author wishes to express his sincere gratitude to Professor Kazuhiro Sawa and Associate professor Shuichiro Miwa (University of Tokyo) for invaluable suggestions, and fruitful discussions. Various comments were invaluable for the whole study. The author wants to thank all my colleagues, especially Tetsuro Murayama, Masahiro Takahashi and Hidenori Moriya for their help and intellectual contributions to this work, Kazuhiro Murata for understanding and cooperation of my Admission. This study was part of the activities of MH21-S R&D consortium funded by the Ministry of Economy, Trade and Industry (METI); organized by the National Institute of Advanced Industrial Science and Technology (AIST) and the author is thankful to the project and Dr. Norio Tenma for the support in publication.

Finally, the author sincerely thanks my wife and family for their understanding and continuous support, and my parents for their encouragement.

Nomenclature

C_0	: distribution parameter
j	: superficial velocity [m/s]
v_{gj}	: drift velocity [m/s]
α	: void fraction
ρ	: density [kg/m3]
g	: gravitational acceleration [m/s2]
u_b	: rise velocity of single bubble [m/s]
D	: diameter of the pipe [m]
DH	: hydraulic diameter [m]
R	: bubble radius [m]
σ	: surface tension [kg/s2]
γ'	: surface tension of high pressure and brine [kg/s2]
υ	: number of ions produced upon dissociation
ω	: weighting factor
Δp	: pressure difference [Pa]
p	: pressure [MPa]
P	: pressure [Pa]
c	: molar concentration [mol/L]
μ	: viscosity coefficient [Pa s]
T	: absolute temperature [K]
R_g	: gas constant [Pa L/K mol]
Re	: Reynolds number
Eo	: Eötvös number
f_s	: constant
ϕ	: two-phase friction multiplier
C_{tr}	: molar concentration which coalescence reduces by more than 95% [mol/L]
B	: 1.5 x 10^{-29} [J m]
L	: Length [m]
f'_i	: friction factor for *i* phase during two-phase flow
u'_i	: velocity for *i* phase during two-phase flow
α'	: ratio of hydraulic diameter of gas during two-phase flow to that during single-phase flow
β'	: ratio of hydraulic diameter of liquid during two-phase flow to that during single-phase flow

u : rise velocity [m/s]

υ : kinematic viscosity [m2/s]

$\bar{l}$: Taylor bubble length [m]

Fr : Froude numbers

L : Length of pixel [pixel]

V : Variance-covariance matrix

$x_{i,k}$: Component *k* of image *i*

$\boldsymbol{u_k}$: Component *k* column vector $\{\boldsymbol{x_{1,k}}, \cdots \boldsymbol{x_{i,k}}, \cdots \boldsymbol{x_{l,k}}\}$

λ_k : Contribution of component *k*

V_j : Image *i* cluster of cluster *j*

$\boldsymbol{W}_j$: Centroid column vector of cluster *j*

$\boldsymbol{x}_i$: Component *q* column vector of image *i*

ε_j : Mixing coefficients of cluster *j*

$\boldsymbol{\mu}_j$: Mean column vector of cluster *j*

$\boldsymbol{V}_j$: Variance-covariance matrix of cluster *j*

l : Number of images

T_r : Total image number of class *r*

$C_{r,j}$: Image number of class *r* classified to cluster *j*

Subscripts/superscripts

g : gas phase

f : liquid phase

m : gas-liquid two-phase

b-s : bubbly to slug flow

gam : gamma densitometer

diff : differential pressure

$+$: non-dimensionalized value

SD : small diameter

LD : large diameter

Table of Contents

List of Figures

List of Tables

1 General Introduction

Gas-liquid two-phase flow, in which the mixture of gas and liquid flows, presents complex flow and heat transfer behavior due to the interactions at the gas-liquid interface. Its flow appears in many industrial systems including nuclear power plants. Thus, the study of gas-liquid two-phase flow has been conducted for about 70 years, and the knowledge of basic principles such as flow pattern, pressure drop, and void fraction in the pipe has been developed. Many industrial systems with two-phase flow, including nuclear power plants, have enhanced their systems based on these knowledges and contributed to the societies development. Meanwhile, technological developments have led to the emergence of new industrial systems that handle unconventional gas-liquid two-phase flows, such as gas production from offshore methane hydrates and fusion reactors that utilize superconductivity. While these systems have the advantage of utilizing the knowledge of gas-liquid two-phase flow developed to date, they also pose new challenges arising from the novel system, and gas production from offshore methane hydrates is one of them.

Methane hydrates are the clathrate where methane dominates as a guest molecule. In recent years, these are drawing attention as an alternative to the existing natural energy source such as natural gas and oil. These hydrates exist under low-temperature and high-pressure conditions, and approximately at least 3,000 trillion m^3 of methane is estimated to be reserved in the world (Boswell and Collett, 2011). In a low-temperature and high-pressure environment, the gas hydrate is typically very stable. The gas can be extracted from the gas hydrate either by heating or depressurization, which both turn out to dissociate the hydrates (Moridis et al., 2007; Konno et al., 2010). From 2002 to 2008, a scaled-down gas hydrate dissociation test was conducted using thermal stimulation and depressurization methods at the Mallik site in the Northwest Territories of Canada (Hancock et al., 2005a). The experiment showed that the thermal stimulation method only created a small volume of methane gas; meanwhile, the depressurization method achieved a continuous gas production (Hancock et al., 2005b; Dallimore and Collett, 2005). Based on these experimental results, the world's first attempt to produce offshore methane gas from the marine gas hydrate deposit in Japan's eastern Nankai Trough area was conducted in 2013 using the depressurization method (Hayashi et al., 2010). The methane gas production process was successful for six consecutive days (Konno et al., 2017). Furthermore, the second continuous production of methane gas was carried out in May 2017, and a total of approximately 222,500 m^3 of methane gas was continuously produced for 24 days (Yamamoto et al., 2019).

As the Japan's Methane Hydrate Program, the MH21-S R&D consortium, established in 2019 for R&D of the pore-filling type of methane hydrate, conducts researches on the depressurization method and the production assessment (Fukumoto et al., 2018; Muraoka et al., 2020; Yamamoto and Tenma, 2021). In this method, boreholes are first drilled to the hydrate saturated sandy layers where the methane hydrate is concentrated, at around 280 m below seafloor in a water depth of approximately

1,000 m (Fujii et al., 2015). At 1,280 m below sea level, hydrates are in equilibrium at the pressure of around 13 MPa (Yamamoto et al., 2017), but dissociates when depressurizes. Therefore, current production method produces gas by dissociating the hydrate through depressurizing the bottom-hole with extracting the liquid present inside the wellbore. With this procedure, the gas production rate highly depends on the bottom-hole pressure, thus, its control is crucial for the stable gas production. Also, assurance of production stability in the long term is necessary for the commercial use. In order to meet this demand, proper specification and design of downhole and control equipment such as gas-liquid separators, water pumps, etc., are essential to stabilize the bottom-hole pressure (Yamamoto, 2009; Konno et al., 2010). To design these devices, determination of the process conditions is necessary considering the flow behavior in the wellbore (Kishi et al., 2018). In general, there are several mechanistic models for estimating the process condition of wellbore used in the oil & gas industry (Nwanwe and Duru, 2022). Hasan and Kabir model (Hasan and Kabir, 1988ab; Kabir and Hasan, 1990; Hasan et al., 2010) is one of them which can analyze the wellbore with the flow regime and pressure drop of the upward gas-liquid two-phase flow.

1.1 Mechanical model

The mechanistic model of Hasan and Kabir model is described, hereafter. In general, pressure drop of upward gas-liquid two phase flow is the pressure difference between the top and bottom of section divided by the distance and comprised of following three components (Deng et al., 2019).

$$\left(-\frac{dP}{dz}\right)_n = \frac{P_n - P_{n+1}}{L_n} = \left(\frac{dP_{grav}}{dz}\right)_n + \left(\frac{dP_{fric}}{dz}\right)_n + \left(\frac{dP_{acc}}{dz}\right)_n \tag{1-1}$$

Here, $\left(dP_{grav}/dz\right)_n$, $\left(dP_{fric}/dz\right)_n$ and $(dP_{acc}/dz)_n$ are gravitational, frictional and acceleration component, respectively. The acceleration term is essential in one-component with phase-changing systems and can be neglected in gas and liquid two-component systems rising long length under high pressure conditions but might be effective under atmospheric pressure conditions which is not considered in the present study. The overall pressure drop of wellbore is calculated by applying the equation (1-1) to each divided section of the entire wellbore, as shown in Fig. 1.1 (Ping et al., 2006). The top and bottom boundary pressure in specific section is derived by pressure drop as follows;

$$P_n = P_{n+1} - \left(\frac{dP}{dz}\right)_n L_n \tag{1-2}$$

Since the boundary pressure of other section is derived as well, the following equation is derived with the summation.

$$P_{BHP} = P_{WP} - \sum_{n=1}^{z} \left(\frac{dP}{dz}\right)_n L_n \tag{1-3}$$

Hence, the process condition and bottom-hole pressure can be stimulated by the well-head pressure and pressure drop of the well bore. Note that the formula for pressure drop in the wellbore needs to correspond to the production conditions, therefore in analyzing methane hydrate production methods, pressure drop in brine systems under high pressure conditions is required.

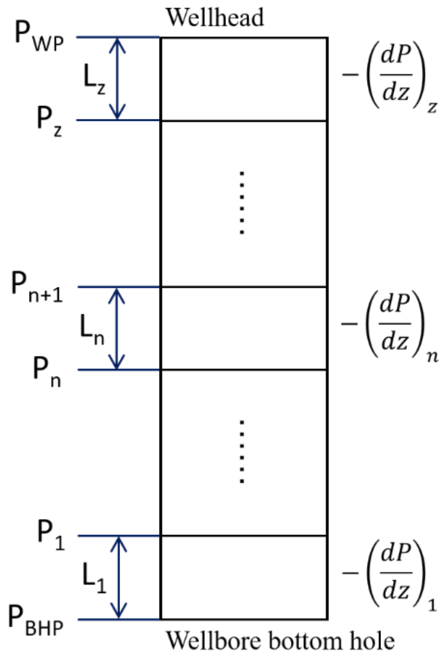

Fig. 1.1. The schematic view of entire wellbore and the pressure drop of each divided section.

The pressure drop for vertical upward two-phase flow is comprised of gravitational and frictional component, as shown in equation (1-1) and each of them are the hydraulic head pressure and frictional pressure drop at the specific section, and for gravitational term is obtained by the following equation.

$$\left(dP_{grav}/dz\right)_n = \{\alpha\rho_g + (1-\alpha)\rho_f\}g \tag{1-4}$$

The equation shows that the term is mainly determined by void fraction, and the Drift flux model are applied for estimating void fraction in Hasan and Kabir model. For frictional term in Hasan and Kabir model is obtained as follows:

$$\left(\frac{dP_{fric}}{dz}\right)_n = \frac{4}{D} f_m \frac{\rho_m}{2} j_m^2 \tag{1-5}$$

where Chen equation (Chen, 1979) is used for the friction factor as follows

$$\frac{1}{\sqrt{f_m}} = 4\log\left[\frac{\epsilon/D}{3.7065} - \frac{5.0452}{Re}\log\left\{\frac{\epsilon^{1.1098}}{2.8257} + \left(\frac{7.149}{Re}\right)^{0.8981}\right\}\right] \tag{1-6}$$

The void fraction and frictional term are calculated for specific section of each elevation.

Since the estimation of void fraction differs depending on flow regime in Drift flux model, the Hasan and Kabir model requires the flow regime and the pressure drop which correspond to the production conditions. The experimental database and the fundamental knowledges of pressure drop are adequate for the oil & gas use owing to the achievement of its industry (Qin et al., 2020), but are few for new application such as the methane hydrates and the experimental data on brine-gas two-phase flow are also scarce. Understanding the pressure drop of gas-liquid two-phase flow in the wellbore is important, especially the effect of the high inlet pressure, presence of the brine, and rising height on pressure drop. Therefore, literature survey of the pressure drop through a long length channel under high-pressure brine conditions were conducted.

1.2 Pressure drop through long channel length

The studies of upward gas-liquid two-phase flow over a long channel length conducted in the past are summarized in Table 1.1. In addition, the specification of apparatus and experimental conditions, as well as obtained results, are tabulated. As can be seen from the table, a number of pressure drop studies were conducted focusing on void fraction distribution and flow regime transitions at atmospheric pressure conditions, but none have focused on pressure drop under high-pressure gas-brine conditions.

Thus, the present study has conducted the foundation of nitrogen-brine two-phase flow behavior under low and high-pressure to estimate the process condition using the conventional model. This study includes (1) void fraction and frictional pressure drop model as the foundation study of gas-liquid two phase flow in chapter 2 and (2) objective flow regime identification method using machine learning technique in chapter 3 and 4. The general conclusion can be found in chapter 5.

Table 1.1. List of upward gas-liquid two-phase flow over long channel length.

Investigators	Type of SI	Operating Conditions	Key Findings
Schmidt et al. (1980)	H=15.2 m D=0.05 m Air – Kerosene	0.107 m/s ≤ j_G ≤ 12.4 m/s 0.015 m/s ≤ j_L ≤ 3.05 m/s P = Atmosphere	Capacitance sensor and pressure gauges were used to measure liquid holdup and local pressure Mathematical model for severe slugging was proposed
Ohnuki et al. (2000)	H=12.3 m D=0.2 m Air – Water	0.03 m/s ≤ j_G ≤ 4.7 m/s 0.06 m/s ≤ j_L ≤ 1.06 m/s P = Atmosphere	Measurement of phase distribution Local void fraction measurement with optical void probe Axial distribution of sectional differential pressure
Guet et al. (2002)	H=18 m D=0.072 m Air – Water	0.03 m/s ≤ j_G ≤ 4.7 m/s 0.1 m/s ≤ j_L ≤ 0.4 m/s P = Atmosphere	Air lift at low Reynolds number Mean bubble vertical chord length with Four-point optical glass fiber probe Effect of bubble size to the transition of flow regime is mentioned
Guet et al. (2003)	H=18 m D=0.072 m Air – Water	0.01 m/s ≤ j_G ≤ 0.3 m/s 0.1 m/s ≤ j_L ≤ 0.4 m/s P = Atmosphere	Gas fraction and vertical chord length of the bubbles were measured with single-optical-fiber probes and four-point optical probe. Theoretical model was proposed to predict the influence on the gaslift efficiency
Shen et al. (2005)	H=24 m D=0.2 m Air – Water	0.03 m/s ≤ j_G ≤ 4.7 m/s 0.1 m/s ≤ j_L ≤ 0.4 m/s P = Atmosphere	Interfacial parameters measurement with optical probes and differential pressure transducers Phase distribution transition was proposed
Shen et al. (2006)	H=12.3 m D=0.2 m Air – Water	0.0322 m/s ≤ j_G ≤ 0.218 m/s 0.144 m/s ≤ j_L ≤ 1.12 m/s P = Atmosphere	Optical four-sensor probe and differential pressure gauges were used to measure void fraction distribution and local differential pressure The two-phase flow in large diameter was discussed

Omebere-Iyari et al. (2007)	H=52 m D=0.189 m Nitrogen – Naphtha	0.09 m/s ≤ j_G ≤ 14.8 m/s 0.004 m/s ≤ j_L ≤ 4 m/s P = 20 bar 0.1 m/s ≤ j_G ≤ 6 m/s 0.004 m/s ≤ j_L ≤ 3 m/s P = 90 bar	Void fraction measurement with gamma densitometers Experimental drift velocity compared with theoretical model Flow regime transition Under high pressure was proposed
Shen et al. (2010)	H=25 m D=0.2 m Air – Water	0.0016 m/s ≤ j_G ≤ 0.093 m/s 0.050 m/s ≤ j_L ≤ 0.311 m/s P = Atmosphere	Hot-film probes, optical multi-sensor probes and differential pressure gauges were used to measure the local void fraction, gas and liquid velocity Appropriate drift flux parameter equation for large diameter pipe is discussed
Shen et al. (2011)	H=26 m D=0.2 m Air – Water	0.052 m/s ≤ j_G ≤ 0.510 m/s 0.050 m/s ≤ j_L ≤ 0.311 m/s P = Atmosphere	Experiment and simulation were compared Void fraction measurement with differential pressure transducers Interfacial drag model was proposed
Shen et al. (2012)	H=26 m D=0.2 m Air – Water	0.0127 m/s ≤ j_G ≤ 0.0254 m/s 0.0505 m/s ≤ j_L ≤ 0.312 m/s P = Atmosphere	Bubbles detected with four-sensor probe Axial and Radial distribution of void fraction and mean diameter measured Interfacial drag model was proposed
Waltrich et al. (2013)	H=42 m D=0.048 m Air – Water	1 m/s ≤ j_G ≤ 29 m/s 0.015 m/s ≤ j_L ≤ 0.315 m/s 1 bar ≤ P ≤ 5.2 bar	Liquid holdup measured with two-wire conductivity probe Measurement of total pressure gradient with pressure transducers

Ali et al. (2014)	H=12.2 m D=0.25 m Air – Water	0.9 m/s $\leq j_G \leq$ 2.2 m/s 0.18 m/s $\leq j_L \leq$ 1.1 m/s P = Atmosphere	Void fraction measurement with differential pressure transducers Flow regime identified with probability mass function derived by void fraction Transition of flow regime for large vertical pipe was proposed
Shen et al. (2015)	H=26 m D=0.2 m Air – Water	0.0178 m/s $\leq j_G \leq$ 0.507 m/s 0.0501 m/s $\leq j_L \leq$ 0.312 m/s P = Atmosphere	Void fraction measured with differential pressure transducers Length of cap bubble measured with optical multi-sensor probes N-shaped axial void fraction change was proposed
Waltrcih et al. (2015a)	H=42 m D=0.048 m Air – Water	5.9 m/s $\leq j_G \leq$ 12.2 m/s 0.013 m/s $\leq j_L \leq$ 0.016 m/s P = Atmosphere	Experiment and model calculation were compared Pressure drop and film thickness were measured with pressure transducers and wire probe sensor Pressure drop model was proposed
Waltrcih et al. (2015b)	H=42 m D=0.05 m Air – Water	0.0127 m/s $\leq j_G \leq$ 0.0254 m/s 0.0505 m/s $\leq j_L \leq$ 0.312 m/s P = Atmosphere	Liquid holdup measured with two-wire conductivity probe Measurement of Axial distribution of liquid holdup and pressure gradient The initiation criteria of Liquid loading onset proposed in the paper was verified.
Alves et al. (2017)	H=42 m D=0.049 m Air – Water	4 m/s $\leq j_G \leq$ 15 m/s 0.017 m/s $\leq j_L \leq$ 0.29 m/s P = Atmosphere	Measured void fraction and pressure drop were compared with the mathematical model Mathematical model predicted well for void fraction and pressure drop

Posada et al. (2017)	H=42 m D=0.048 m Air – Water	4 m/s $\leq j_G \leq$ 21 m/s 0.017 m/s $\leq j_L \leq$ 0.3 m/s P = 130 and 230 kPa	Local liquid holdup and pressure measured with two-wire conductivity probe and pressure transducers The time and height variation of local liquid holdup and pressure on frequency oscillations The flow state of frequency oscillations was evaluated.
Posada et al. (2018)	H=42 m D=0.048 m Air – Water	4 m/s $\leq j_G \leq$ 21 m/s 0.017 m/s $\leq j_L \leq$ 0.3 m/s P = 130 and 210 kPa	Measurement of liquid holdup, pressure gradient and frequency of large liquid structure with pressure transducers, two-wire conductivity probe etc. Flow of low frequency oscillations and steady state were compared The influence of low frequency oscillations to application was discussed

Bibliography

Ali, S.F., Yeung, H., 2014. Two-phase flow patterns in large diameter vertical pipes. Asia-Pacific Journal of Chemical Engineering 9, 105–116. https://doi.org/10.1002/apj.1750

Alves, M.V.C., Waltrich, P.J., Gessner, T.R., Falcone, G., Barbosa, J.R., 2017. Modeling transient churn-annular flows in a long vertical tube. International Journal of Multiphase Flow 89, 399–412. https://doi.org/10.1016/j.ijmultiphaseflow.2016.12.001

Boswell, R., Collett, T.S., 2011. Current perspectives on gas hydrate resources. Energy Environ. Sci. 4, 1206–1215.

Chen, N.H., 1979. An Explicit Equation for Friction Factor in Pipe. Ind. Eng. Chem. Fund. 18, 296–297. https://doi.org/10.1021/i160071a019

Deng, Y.-R., Jin, N.-D., Yang, Q.-Y., Wang, D.-Y., 2019. A Differential Pressure Sensor Coupled with Conductance Sensors to Evaluate Pressure Drop Prediction Models of Gas-Water Two-Phase Flow in a Vertical Small Pipe. Sensors 19, 2723. https://doi.org/10.3390/s19122723

Dallimore S. R., Collett T. S., Summary and implications of the Mallik 2002 gas hydrate production research well program, in Scientific Results from the Mallik 2002 Gas Hydrate Production Well Program, Mackenzie Delta, Northwest Territories, Canada, ed. S. R. Dallimore and T. S. Collett, Geological Survey of Canada Bulletin 2005, 585, 1–36.

Fujii, T., Suzuki, K., Takayama, T., Tamaki, M., Komatsu, Y., Konno, Y., Yoneda, J., Yamamoto, K., Nagao, J., 2015. Geological setting and characterization of a methane hydrate reservoir distributed at the first offshore production test site on the Daini-Atsumi Knoll in the eastern Nankai Trough, Japan. Marine and Petroleum Geology, Gas hydrate drilling in Eastern Nankai 66, 310–322. https://doi.org/10.1016/j.marpetgeo.2015.02.037

Fukumoto, A., Kamada, K., Sato, T., Oyama, H., Torii, H., Kiyono, F., Nagao, J., Temma, N., Narita, H., 2018. Numerical simulation of pore-scale formation of methane hydrate in the sand sediment using the phase-field model. Journal of Natural Gas Science and Engineering 50, 269–281.

Guet, S., Ooms, G., Oliemans, R.V.A., 2002. Influence of bubble size on the transition from low-Re bubbly flow to slug flow in a vertical pipe. Experimental Thermal and Fluid Science 26, 635–641. https://doi.org/10.1016/S0894-1777(02)00172-3

Guet, S., Ooms, G., Oliemans, R.V.A., Mudde, R.F., 2003. Bubble injector effect on the gaslift efficiency. AIChE Journal 49, 2242–2252. https://doi.org/10.1002/aic.690490903

Hasan, A.R., Kabir, C.S., 1988a. Predicting Multiphase Flow Behavior in a Deviated Well. SPE Production Engineering 3, 474–482. https://doi.org/10.2118/15449-PA

Hasan, A.R., Kabir, C.S., 1988b. A Study of Multiphase Flow Behavior in Vertical Wells. SPE Production Engineering 3, 263–272. https://doi.org/10.2118/15138-PA

Hasan, A.R., Kabir, C.S., Sayarpour, M., 2010. Simplified two-phase flow modeling in wellbores. Journal of Petroleum Science and Engineering 72, 42–49. https://doi.org/10.1016/j.petrol.2010.02.007

Hancock S. H., Collett T. S., Dallimore S. R., Satoh T., Inoue T., Huenges E., Weatherill B., 2005a, Overview of thermal stimulation production-test results for the JAPEX/JNOC/GSC et al. Mallik 5L-38 gas hydrate production research well, in Scientific Results from the Mallik 2002 Gas Hydrate Production Well Program, Mackenzie Delta, Northwest Territories, Canada, ed. T. S. Dallimore and T. S. Collett, Geological Survey of Canada Bulletin 585, 135.

Hancock S. H., Dallimore S. R., Collett T. S., Carle D., Weatherill B., Satoh T., Inoue T., 2005b, Overview of pressure drawdown production test results for the JAPEX/JNOC/GSC et al. Mallik 5L-38 gas hydrate production research well, in Scientific Results from the Mallik 2002 Gas Hydrate Production Well Program, Mackenzie Delta, Northwest Territories, Canada, ed. S. R. Dallimore and T. S. Collett, Geological Survey of Canada Bulletin 585, 134.

Hayashi, M., Saeki, T., Inamori, T., Noguchi, S., 2010. The distribution of BSRs related to methane hydrates, offshore Japan. Journal of the Japanese Association for Petroleum Technology 75, 42–53. https://doi.org/10.3720/japt.75.42

Kabir, C.S., Hasan, A.R., 1990. Performance of a two-phase gas/liquid flow model in vertical wells. Journal of Petroleum Science and Engineering 4, 273–289. https://doi.org/10.1016/0920-4105(90)90016-V

Kishi, K., Matsuzawa, M., Ishida, K., Yoshida, H., Matsunaga, T., 2018. The FEED/EPC management of production test system for the second methane hydrate offshore production test in Japan . Journal of the Japanese Association for Petroleum Technology 83, 342–356. https://doi.org/10.3720/japt.83.342

Konno, Y., Masuda, Y., Hariguchi, Y., Kurihara, M., Ouchi, H., 2010. Key Factors for Depressurization-Induced Gas Production from Oceanic Methane Hydrates. Energy Fuels 24, 1736–1744. https://doi.org/10.1021/ef901115h

Konno, Y., Fujii, T., Sato, A., Akamine, K., Naiki, M., Masuda, Y., Yamamoto, K., Nagao, J., 2017. Key Findings of the World's First Offshore Methane Hydrate Production Test off the Coast of Japan: Toward Future Commercial Production. Energy Fuels 31, 2607‑2616.

Moridis, G.J., Kowalsky, M.B., Pruess, K., 2007. Depressurization-Induced Gas Production From Class-1 Hydrate Deposits. SPE Reservoir Evaluation & Engineering 10, 458–481.

Muraoka, M., Yamamoto, Y., Tenma, N., 2020. Simultaneous measurement of water permeability and methane hydrate pore habit using a two-dimensional glass micromodel. Journal of Natural Gas Science and Engineering 77, 103279.

Nwanwe, C.C., Duru, U.I., 2022. Comparison and performance Analysis of Models for Predicting Multiphase flow Behaviours in Wellbores. international journal of petroleum and geoscience engineering 2022, 1–20.

Ohnuki, A.A., Akimoto, H., 2000. Experimental study on transition of flow pattern and phase distribution in upward air–water two-phase flow along a large vertical pipe. https://doi.org/10.1016/S0301-9322(99)00024-5

Omebere-Iyari, N.K., Azzopardi, B.J., Ladam, Y., 2007. Two-phase flow patterns in large diameter vertical pipes at high pressures. AIChE Journal 53, 2493–2504. https://doi.org/10.1002/aic.11288

Ping, L., Wang, Z., Wei, J., 2006. Pressure drop models for gas-liquid two-phase flow and its application in underbalanced drilling* *Supported by program for Changjiang Scholars and Innovative Research Team in University (IRT0411). Journal of Hydrodynamics, Ser. B, Proceedings of the Conference of Global Chinese Scholars on Hydrodynamics 18, 405–411. https://doi.org/10.1016/S1001-6058(06)60086-3

Posada, C., Waltrich, P.J., 2017. Effect of forced flow oscillations on churn and annular flow in a long vertical tube. Experimental Thermal and Fluid Science 81, 345–357. https://doi.org/10.1016/j.expthermflusci.2016.10.015

Posada, C., Waltrich, P.J., 2018. Similarities and differences in churn and annular flow regimes in steady-state and oscillatory flows in a long vertical tube. Experimental Thermal and Fluid Science 93, 272–284. https://doi.org/10.1016/j.expthermflusci.2017.12.025

Qin, H., Dai, J., Liu, X., Yang, G., Pei, Y., Gou, S., Chen, M., 2020. Slip behaviours and evaluation of interpretative model of oil/water two-phase flow in a large-diameter pipe. Journal of Petroleum Science and Engineering 186, 106707. https://doi.org/10.1016/j.petrol.2019.106707

Schmidt, Z., Brill, J.P., Beggs, H.D., 1980. Experimental Study of Severe Slugging in a Two-Phase-Flow Pipeline - Riser Pipe System. Society of Petroleum Engineers Journal 20, 407–414. https://doi.org/10.2118/8306-PA

Shen, X., Mishima, K., Nakamura, H., 2005. Two-phase phase distribution in a vertical large diameter pipe. International Journal of Heat and Mass Transfer 48, 211–225. https://doi.org/10.1016/j.ijheatmasstransfer.2004.06.034

Shen, X., Saito, Y., Mishima, K., Nakamura, H., 2006. A study on the characteristics of upward air–water two-phase flow in a large diameter pipe. Experimental Thermal and Fluid Science 31, 21–36. https://doi.org/10.1016/j.expthermflusci.2006.01.007

Shen, X., Matsui, R., Mishima, K., Nakamura, H., 2010. Distribution parameter and drift velocity for two-phase flow in a large diameter pipe. Nuclear Engineering and Design, The 6th Japan-Korea Symposium on Nuclear Thermal Hydraulics and Safety - NTHAS6 Special Section 240, 3991–4000. https://doi.org/10.1016/j.nucengdes.2010.01.004

Shen, X., Mishima, K., Nakamura, H., 2011. Interfacial Drag Model and Numerical Analysis for Gas-Liquid Two-Phase Flow in a Large Diameter Pipe. Japanese Journal of Multiphase Flow 24, 595–602. https://doi.org/10.3811/jjmf.24.595

Shen, X., Hibiki, T., Nakamura, H., 2012. Developing structure of two-phase flow in a large diameter pipe at low liquid flow rate. International Journal of Heat and Fluid Flow 34, 70–84. https://doi.org/10.1016/j.ijheatfluidflow.2012.02.004

Shen, X., Hibiki, T., Nakamura, H., 2015. Bubbly-to-cap bubbly flow transition in a long-26m vertical large diameter pipe at low liquid flow rate. International Journal of Heat and Fluid Flow 52, 140–155. https://doi.org/10.1016/j.ijheatfluidflow.2015.01.001

Waltrich, P.J., Falcone, G., Barbosa, J.R., 2013. Axial development of annular, churn and slug flows in a long vertical tube. International Journal of Multiphase Flow 57, 38–48. https://doi.org/10.1016/j.ijmultiphaseflow.2013.06.008

Waltrich, P.J., Falcone, G., Barbosa, J.R., 2015a. Liquid transport during gas flow transients applied to liquid loading in long vertical pipes. Experimental Thermal and Fluid Science 68, 652–662. https://doi.org/10.1016/j.expthermflusci.2015.07.004

Waltrich, P.J., Posada, C., Martinez, J., Falcone, G., Barbosa, J.R., 2015b. Experimental investigation on the prediction of liquid loading initiation in gas wells using a long vertical tube. Journal of Natural Gas Science and Engineering 26, 1515–1529. https://doi.org/10.1016/j.jngse.2015.06.023

Yamamoto, K., 2009. Production Techniques for Methane Hydrate Resources and Field Test Programs. Journal of Geography (Chigaku Zasshi) 118, 913–934. https://doi.org/10.5026/jgeography.118.913

Yamamoto, K., Kanno, T., Wang, X.-X., Tamaki, M., Fujii, T., Chee, S.-S., Wang, X.-W., Pimenov, V., Shako, V., 2017. Thermal responses of a gas hydrate-bearing sediment to a depressurization operation. RSC Advances 7, 5554–5577. https://doi.org/10.1039/C6RA26487E

Yamamoto, K., Wang, X.-X., Tamaki, M., Suzuki, K., 2019. The second offshore production of methane hydrate in the Nankai Trough and gas production behavior from a heterogeneous methane hydrate reservoir. RSC Advances 9, 25987–26013. https://doi.org/10.1039/C9RA00755E

Yamamoto, K., Tenma, N., 2021. Development of Methane Hydrate Resources - Issues for Commercialization and Their Current R & D Status. Marine Engineering 56, 244–250. https://doi.org/10.5988/jime.56.244

2 Void fraction and frictional pressure drop model

2.1 Introduction

As described above, none of the study have focused on pressure drop through long channel length under high-pressure gas-brine conditions. Since studying the gravitational and the frictional component is sufficient for understanding the behavior of pressure drop shown in equation (1-1), a literature survey on these terms were conducted.

2.1.1 Gravitational pressure drop

Existing studies of void fraction were first surveyed since the void fraction mainly determines the gravitational term, referring to equation (1-4). As the previous section provides studies of long channel length, this section mainly presents studies of brine conditions. Previously, experiments have been performed to investigate the effect of brine on two-phase flow, mainly in bubble column. Ribeiro Jr. and Mewes (2007) conducted experiments with cylindrical column whose height is 1.25 m and inner diameter is 0.12m for various electrolytes including NaCl. Orvalho et al. (2009) performed bubble column experiments with 2 m height, 0.14 m inner diameter using NaCl and water aqueous solutions. These studies exhibit that gas hold-up increases with the concentration of brine. Mandalahalli et al. (2020) conducted experiments with airlift bubble column whose height is 0.75 m for NaCl salt concentrations of 0-2 mol/L. The study indicates the rise of void fraction is due to an increase in residence time caused by decrease of bubble diameter, and this reduction was attributed to the inhibition of bubble coalescence due to the presence of brine as a continuous phase. Finally, Besagni and Inzoli (2020) carried out counter-current bubble column experiments with 5.3 m height , 0.24 m inner diameter using aqueous solutions of NaCl and ionized water or tap water. This study shows that the presence of brine increases the gas holdup and decrease in the bubble size distribution. According to the study, change in bubble size distribution is caused by the inhibition of bubble coalescence, and the increase in gas hold-up is due to the stabilization of homogeneous flow with the smaller bubbles migrating towards the channel wall. Thus, it is likely that the void fraction of gas-brine two-phase flow may be affected by the presence of brine. While studies of void fraction behaviors are available for bubble column and counter-current flow with brine under an atmospheric pressure, much less attention has been paid to the co-current flow and high-pressure condition. Given the lack of studies on upward gas-brine two-phase flows, no reliable models nor correlations to estimate void fraction with brine effects were found to the authors' knowledge.

2.1.2 Frictional pressure drop

Several studies of frictional pressure drop in two-component upward co-current two-phase flows are surveyed. Sawai et al. (2004) conducted experiments with inner diameter of 0.0258 m and height of 4.2m for superficial liquid velocities of 0.002–0.4 m/s of two-component two-phase flow. Experimental results obtained mainly under low liquid and high gas superficial velocity are compared with the equation proposed by Shiba et al. (1966) to investigate the effect of large waves. Shannak (2008) carried out air-water two-phase flow experiments with an inner diameter of 0.0525 m and a height of 5.9 m for vertical section. This study measured frictional pressure drop using rough pipes and developed a new model along with previous experimental results. Lu et al. (2018) performed experiments with inner diameter of 0.050 m and height of 10.5 m for superficial liquid velocities of 0.070–4 m/s to measure the frictional pressure drop of air-water two-phase flow. Experimental results of gas-liquid two-phase flows with high superficial liquid velocities are compared with Lockhart-Martinelli, and new parameters are presented. Thus, although there are studies on frictional pressure drop of gas-liquid two-phase flows with short channel length under low pressure as described above, fewer studies exist for upward gas-brine two-phase flows over long length under high-pressure.

Hence, while studies of upward gas-liquid two-phase flows over long channel length with pressure drop, void fraction distribution and flow regime transitions are available under atmospheric pressure, no studies exist for pressure drop under prototypic high-pressure brine conditions. Also, studies of void fraction and frictional pressure drop, which is the decomposed element of pressure drop, lacks results with the effect of brine. Therefore, the void fraction and frictional pressure drop of upward gas-brine two-phase flow with high superficial liquid velocity rising long length under high pressure, as the basis for pressure drop, are investigated in the present study.

2.2 Experimental work

2.2.1 Experimental facility

The schematic diagram of the experimental apparatus is shown in Fig. 2.1. The liquid (tapped water) is supplied from the gas-liquid separation tank through a centrifugal pump to the tube inlet, and the gas phase (nitrogen) is supplied from the cylinder through the pressure-reducing valve. The pump can discharge up to 250 L/min of water at a total pump head of 43 m. The two-phase mixture passes through the screen composed of 150 μm pore size mesh and Johnson screen. The gas disperser used in the present study is the same as the one used in the offshore gas production test. Since gas and liquid circulate in the apparatus under high-pressure conditions, the observation tube, gas-liquid separator, and attached piping were designed to withstand the high pressure. A control valve is equipped in the gas emission line to control the flow rate while maintaining pressure. The system pressure was measured using a pressure transmitter (Azbil AT9000 SuperAce) located at the gas-liquid separation tank. The Coriolis flowmeter (Oval corporation ALTImass II TypeU) is used to measure the flow rates for gas and liquid phases. The measurement accuracy of the instrument is within 1% of full scale. A thermocouple (Okazaki Manufacturing AEROPAK) was installed in the gas supply line to measures the reference temperature to calculate the superficial gas velocity. In addition, a gas-liquid separation tank of 785 L was used to ensure sufficient separation of gas and liquid in the salinity condition under high pressure. In the present study, the nitrogen-water two-phase flow mixture flows upward through a 52.7 mm I.D., 28 m long vertical observation tube. Several visualization ports (25 mm in diameter) for observing the flow structure is installed at the tube surface, and a high-speed camera was utilized to record the flow images. The port consists of narrow observation area with sight-glass which is thick enough to withstand the high pressure. The DITECT high-speed cameras (HAS-D71 and HAS-D73) were used to take the sequential images of the flow regime. The non-invasive and non-intrusive gamma densitometer (NanoGray PM-1000 and PH-1100A) was used to obtain the void fraction. The measurement accuracy of the instrument is within 0.3 % of full scale. Differential pressure transmitters (Azbil AT9000 SuperAce and Yokogawa DPharp EJX) were installed to measure the local pressure difference of the tube. The respective measurement accuracies are within 0.1% and 0.075% of Full Scale.

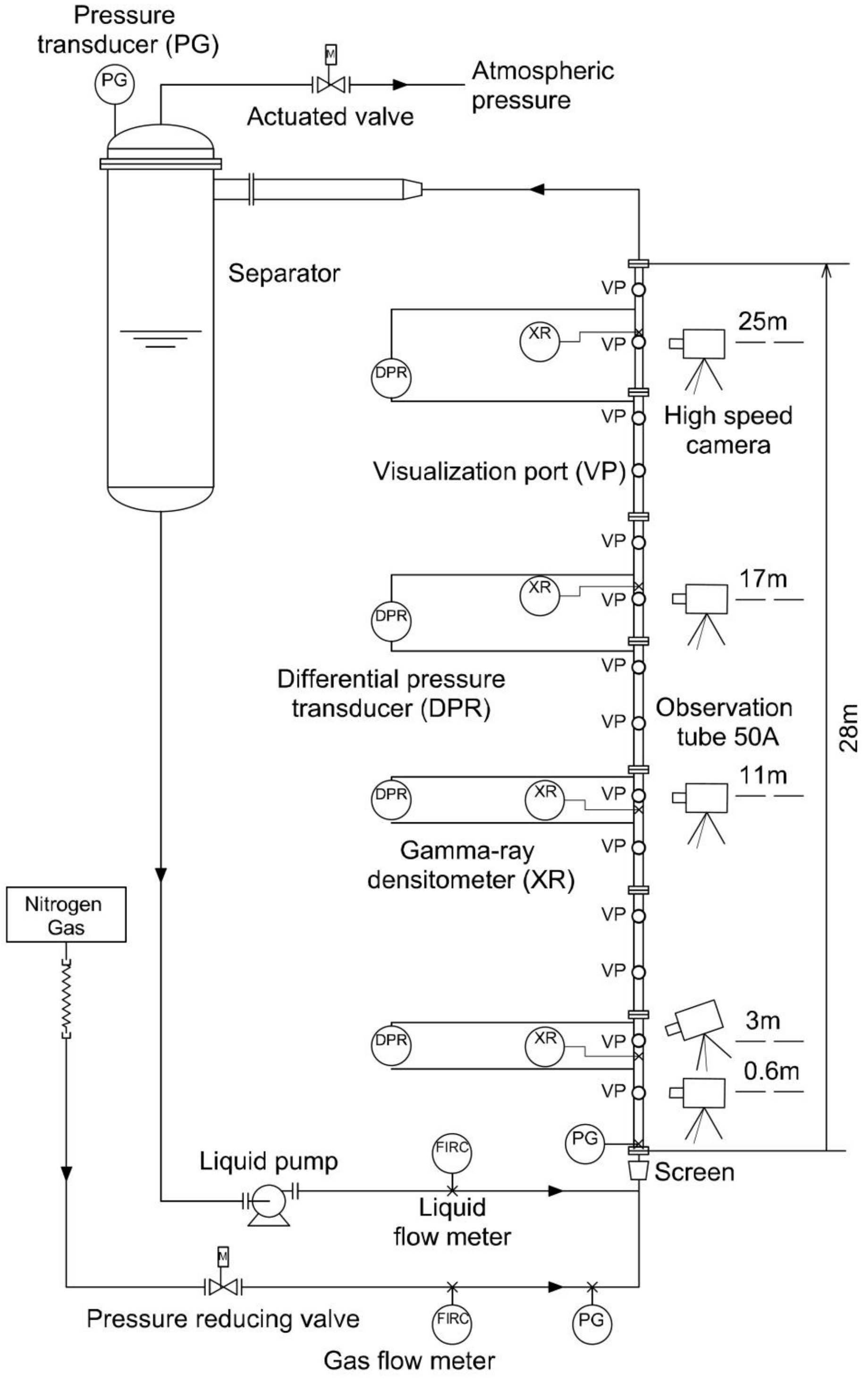

Fig. 2.1. Schematic diagram of apparatus used to obtain experimental data for establishing flow regime identification method.

2.2.2 Experimental condition and procedure

The experimental conditions of the present study are listed in Table 2.1.

Table 2.1. Experiment condition.

Superficial gas velocity (inlet)	0.3 – 3.0 [m/s]
Superficial liquid velocity	0.5 - 2.5 [m/s]
Gas	Nitrogen
Liquid	Tapped water, Brine (3.5 [wt%])
Pressure	0 – 2.8 [MPaG]

The salinity was set to 0 wt% as tap water, and 3.5 wt% as brine considering that 3-3.5 wt% has been simulated for methane hydrate production in previous studies (Jiang et al, 2018; Zhou et al, 2020; Ouchi et al, 2022) and that 3.5 wt% seawater at the seafloor has also been massively lifted. The inlet superficial gas velocities were 0.25 to 3 m/s and the superficial liquid velocities were 0.5 to 2.5 m/s. Both low and 2.8 MPa outlet pressure conditions at gas-liquid separation tank were carried out. This condition was based on the previous studies that the methane gas recovery factor increases at the production pressure of 3 MPa or less (Konno et al, 2014) and that the production pressure is recommended to be closer to the hydrate quadruple point pressure 2.56 MPa (Li et al, 2020). The nitrogen gas was adopted since air has been used as a substitute for methane gas in the past studies of vertically upward gas-liquid two-phase flows (Hironaka et al., 2011), and the difference in the flow behavior is expected to be small given that methane gas and nitrogen are the same nonpolar molecules. The measurement conditions of the gamma densitometer and differential pressure for the present experiment are shown in Table 2.2. Measurement locations of the top and bottom for each differential pressure are also listed.

Table 2.2. Measurement condition for each instrumentation.

	Gamma densitometer	Differential pressure
Accumulated measuring time	120 [sec]	2 [sec]
Measured height	2.7, 10.7, 17.3, 25.6 [m]	2.0-3.9, 10.0-11.9, 15.9-18.0, 23.9-26.1 [m]

In order to obtain steady-state parameters, measurements were time-average for 60 seconds after setting to the specific conditions. The recording conditions of the high-speed camera are tabulated in Table 2.3. The backlight was projected at the visualization port during the recording to capture the image with good resolution. In the experiment, recordings were done at five different elevations. After giving 120 seconds of stabilization time at a given flow condition, the recording was initiated to obtain stable flow images.

Table 2.3. Hi-speed camera setup

Resolution	640×480 [pixel]
	1,280×1,028 [pixel]
Frame speed	2,000 [fps]
Observed height	0.6, 3.0, 11.0, 17.0, 25.3 [m]

In this experiment, the density and pressure drop of gas-liquid two-phase flow was first measured, and the void fraction and frictional pressure drop values were obtained. Then, these values were compared with existing correlations models for the assessment. The experimental void fraction values obtained from the gamma-ray densitometer and differential pressure gauge are expressed as follows:

$$\alpha_{\mathrm{gam}} = (\rho_m - \rho_f)/(\rho_g - \rho_f) \tag{2-1}$$

$$\alpha_{\mathrm{diff}} = \Delta p/\{(\rho_g - \rho_f)gL\} \tag{2-2}$$

Here, the nitrogen gas is evaluated referring to Span et al. (2000) and for the brine, density is measured with gamma-ray densitometer in advance. The void fraction value from the gamma-ray densitometer is obtained by assuming that the volumetric void fraction is equivalent to the cross-sectional void fraction. In order to verify this assumption, the void fraction measured by the differential pressure was used. The frictional pressure drop of the gas-liquid two-phase flow is assumed to be negligibly small due to the low superficial liquid velocity condition.

As for the pressure drop, the following relation is used to estimate the experimental value:

$$\left(-\frac{dP}{dz}\right)_m = \frac{\Delta p}{L} \tag{2-3}$$

Here, the pressure drop consists of frictional and gravitational term that depends on the void fraction, as shown in Equations (1-2) and (1-4), and the acceleration term is not considered in the present study. Thus, the frictional pressure drop can be calculated from the experimental pressure drop and void fraction as follows.

$$\left(\frac{dP_{fric}}{dz}\right)_m = \frac{\Delta p}{L} - \{\alpha\rho_g + (1-\alpha)\rho_f\}g \tag{2-4}$$

2.3 Modeling

2.3.1 Drift flux model approach

Typical models utilized to estimate void fraction in gas-liquid two-phase flows include homogeneous flow models, slip flow models, drift flux models, and separated flow models. Here, the void fractions of gas-liquid two-phase flow are analyzed with the drift flux model. This model was developed by Zuber and Findlay (1965) and Ishii (1977), where the local mean gas velocity is given by

$$j_g/\alpha = C_0\left(j_g + j_f\right) + v_{gj} \tag{2-5}$$

In this experiment, gas density changes with pressure as the gas-liquid two-phase flow rises through the vertical channel. Thus, to reflect this change, the present study utilizes the following dimensionless equation proposed by Hibiki and Ishii (2003)

$$j_g^+/\alpha = C_0 j^+ + v_{gj}^+ \tag{2-6}$$

where

$$j^+ = j_g^+ + j_f^+ \tag{2-7}$$

$$j_g^+ = \frac{j_g}{\left\{\frac{\sigma g\left(\rho_f - \rho_g\right)}{\rho_g^2}\right\}^{1/4}} \tag{2-8}$$

$$j_f^+ = \frac{j_f}{\left\{\frac{\sigma g\left(\rho_f - \rho_g\right)}{\rho_g^2}\right\}^{1/4}} \tag{2-9}$$

$$v_{gj}^+ = \frac{v_{gj}}{\left\{\frac{\sigma g\left(\rho_f - \rho_g\right)}{\rho_g^2}\right\}^{1/4}} \tag{2-10}$$

C_0 is the distribution parameter and v_{gj} is the drift velocity, and these are calculated separately for each flow regime as follows:

Distribution parameter

$$C_0 = 1.2 - 0.2\sqrt{\frac{\rho_g}{\rho_f}} \tag{2-11}$$

Drift velocity in bubbly flow

$$v_{gj} = \sqrt{2}\left\{\frac{\sigma g(\rho_f - \rho_g)}{\rho_f^2}\right\}^{1/4}(1-\alpha)^{1.75} \tag{2-12}$$

Drift velocity in slug flow

$$v_{gj} = 0.35\sqrt{\frac{\sigma g(\rho_f - \rho_g)}{\rho_f}} \tag{2-13}$$

The equation for distribution parameter and drift velocity depends not only on flow regime but also on pipe diameter. Specifically, the equation varies with the following dimensionless diameter.

$$D_H^* = \frac{D_H}{\sqrt{\frac{\sigma}{g\Delta\rho}}} \tag{2-14}$$

Schlegel et al. (2010) have divided the diameters into small and large scales, interpolated with the transition region. Given the pressure and gas density, the dimensionless diameter in the present study is between 19.5 and 19.8, which is in transition region. The distribution parameter and drift velocity are given for transition region as follows:

$$C_0 = \omega_D C_{0,SD} - (1-\omega_D)C_{0,LD} \tag{2-15}$$

$$v_{gj}^+ = \omega_D v_{gj,SD}^+ - (1-\omega_D)v_{gj,LD}^+ \tag{2-16}$$

The distribution parameter and drift velocity for the small diameter are shown in equation (2-11) to (2-13). For the large diameter pipe, drift-flux correlations applicable for the present study are shown as follows (Kataoka and Ishii, 1987; Hibiki and Ishii, 2003):

Distribution parameter in slug flow for large diameter

$$C_0 = [0.6exp\{-1.2(j^+ - 1.8)\} + 1.2]\left(1 - \sqrt{\frac{\rho_g}{\rho_f}}\right) + \sqrt{\frac{\rho_g}{\rho_f}} \quad for\ 1.8 \le \langle j^+ \rangle \tag{2-17}$$

Drift velocity in slug flow for large diameter

Low viscous case $N_{\mu f} \leq 2.25 \times 10^{-3}$ *with* $D_H^* \leq 30$

$$v_{gj}^+ = 0.0019 {D_H^*}^{0.809} \left(\frac{\rho_g}{\rho_f}\right)^{-0.157} N_{\mu f}^{-0.562} \tag{2-18}$$

and for $D_H^* \geq 30$

$$v_{gj}^+ = 0.03 \left(\frac{\rho_g}{\rho_f}\right)^{-0.157} N_{\mu f}^{-0.562} \tag{2-19}$$

where the viscosity number $N_{\mu f}$ *is defined as*

$$N_{\mu f} \equiv \frac{\mu_f}{\left\{\rho_f \sigma \sqrt{\frac{\sigma}{g(\rho_f - \rho_g)}}\right\}^{1/2}} \tag{2-20}$$

Distribution parameter in bubbly flow for large diameter

$$C_0 = exp\left\{0.475 \left(\frac{j_g^+}{j^+}\right)^{1.69}\right\}\left(1 - \sqrt{\frac{\rho_g}{\rho_f}}\right) + \sqrt{\frac{\rho_g}{\rho_f}} \quad for\ 0 < \frac{\langle j_g^+ \rangle}{\langle j^+ \rangle} < 0.9 \tag{2-21}$$

and

$$C_0 = exp\left\{-2.88 \left(\frac{j_g^+}{j^+}\right) + 4.08\right\}\left(1 - \sqrt{\frac{\rho_g}{\rho_f}}\right) + \sqrt{\frac{\rho_g}{\rho_f}} \quad for\ 0.9 < \frac{\langle j_g^+ \rangle}{\langle j^+ \rangle} \tag{2-22}$$

Drift velocity in bubbly flow for large diameter

$$v_{gj}^+ = exp(-1.39 j_g^+) v_{gj,SD}^+ + \{1 - exp(-1.39 j_g^+)\} v_{gj,LD}^+ \tag{2-23}$$

Where $v_{gj,LD}^+$ is equation (2-18) or (2-19). Furthermore, the effects of high pressure and salinity on the surface tension calculated in the dimensionless equation were considered with the approach by Wiegand and Franck (1994), Duchateau and Broseta (2012), and Firouzi and Nguyen (2014), and the following equations were applied.

$$-\gamma_b^0(0) + \gamma_b(0, p) = -0.000533p \tag{2-24}$$

$$\gamma_b^0(c) = 0.001704c + 0.072429 \tag{2-25}$$

$$\gamma_b(c,p) = 0.001704c + 0.072429 - 0.000533p \tag{2-26}$$

Following the equation above, surface tension tends to rise with increasing salinity while declining with increasing pressure

2.3.2 Lockhart-Martinelli approach

There are several approaches for estimating frictional pressure drop in gas-liquid two-phase flows, but the most common approach is to treat two-phase flow as homogeneous flow and the separated flow. Especially, the separated flow model was proposed by Lockhart and Martinelli (1949), which calculates the frictional pressure drop of gas-liquid two-phase flow by multiplying the single-phase frictional pressure drop, such as gas or liquid phase, with the two-phase flow friction multiplier, which are typically expressed as follows:

$$\left(\frac{dP_{fric}}{dz}\right)_n = \phi_f^2 \left(-\frac{dP_{fric}}{dz}\right)_f \tag{2-27}$$

$$\left(-\frac{dP_{fric}}{dz}\right)_f = \frac{4}{D} f_f \frac{\rho_f}{2} j_f^2 \tag{2-28}$$

Here f_i is the Fanning friction factor, which is obtained by the following Blasius form

$$f_i = kRe_i^{-n} \tag{2-29}$$

$$Re_i = \rho_i j_i D/\mu_i \tag{2-30}$$

where i=g or f for gas or liquid, k=16, n=-1 for laminar flow and k=0.046, n=0.2 for turbulent flow. Sharqawy et al. (2010) and Nayar et al. (2016) are referred for the viscosity coefficient of brine. Lockhart and Martinelli proposed the correlation between the two-phase frictional multiplier and the Martinelli parameter (X).

$$X^2 = \left(-\frac{dP_{fric}}{dz}\right)_f \Big/ \left(-\frac{dP_{fric}}{dz}\right)_g \tag{2-31}$$

$$\left(-\frac{dP_{fric}}{dz}\right)_g = \frac{4}{D} f_g \frac{\rho_g}{2} j_g^2 \tag{2-32}$$

Furthermore, Chisholm (1967) proposed the following correlation based on Lockhart and Martinelli approach:

$$\phi_f^2 = 1 + C/X + 1/X^2 \tag{2-33}$$

where C is the Chisholm parameter and assumed by the following equation, but generally the values vary depending on the flow state of each phase as shown in Table 2.4.

$$C = Z + 1/Z \tag{2-34}$$

Where, Z is derived as a function of the density of the gas and liquid, etc as follows;

$$Z = \sqrt{\rho_f f_f' u_f'^2 \alpha' / \rho_g f_g' u_g'^2 \beta'} \tag{2-35}$$

Table 2.4. Variation of parameter C for various flow state.

	Liquid laminar	Liquid turbulent
Gas laminar	5	10
Gas turbulent	12	20

2.4 Results and Discussion

2.4.1 Local pressure and gamma ray densitometer

The wellhead and bottom hole pressure for each height are shown in Fig. 2.2. These pressures are measured at the gas-liquid separation tank and pipe entrance respectively in four different conditions, i.e., low and high-pressure conditions with tap water or brine, and the figure shows the pressures for typical experimental conditions. As shown in Fig. 2.2, the pressure decreases with rising height, and the former studies have shown that the local pressure at each height can be interpolated with the wellhead and the bottom hole pressure (Shen et al, 2015). Furthermore, the bottom hole pressure is comparable to the well head pressure combined with hydraulic head pressure, thus, the local pressure can be estimated by summing the gas-liquid separation tank pressure and the hydraulic head pressure at relevant height, respectively.

The void fraction measured by the gamma ray densitometer is compared with that obtained from the differential pressure as shown in Fig. 2.3. The results are for tap-water, with superficial liquid velocity of 0 to 0.3 m/s and superficial gas velocity of 0.1 to 0.6 m/s under 2.8 MPaG condition. To confirm the assumption that the frictional pressure drop is negligibly small in measuring the void fraction with differential pressure, the frictional pressure drop is calculated with Lockhart-Martinelli approach using flow state of parameter C for all measured conditions. The calculation results showed that average ratio of the frictional pressure drop to the total pressure drop is about 1.0 %. Therefore, the assumption of negligibly small frictional pressure drop is appropriate.

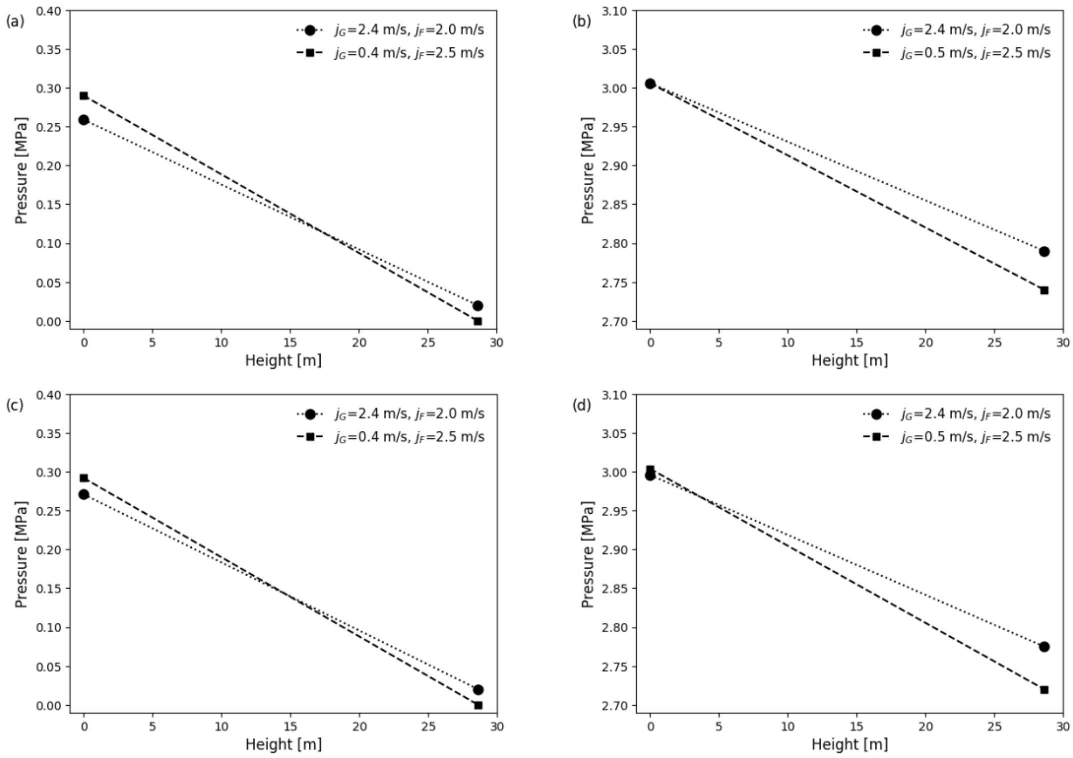

Fig. 2.2. The wellhead and bottom-hole pressure of each height for (a) P=0 MPaG, (b) P=2.8 MPaG of tap water and (c) P=0 MPaG, (d) P=2.8 MPaG of brine.

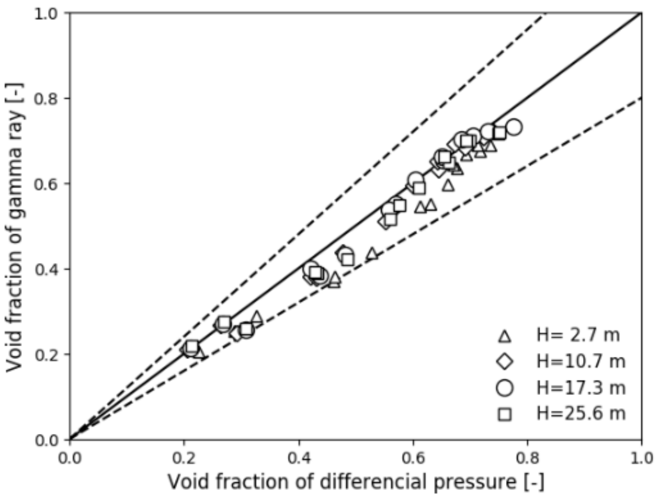

Fig. 2.3. The comparison of void fraction derived from gamma ray densitometer and differential pressure transmitter.

The void fraction of the gamma-ray densitometer relative to that of the differential pressure is located within ±20% in the range 0.2-0.8. Whereas the gamma ray densitometer underestimates the void fraction at around 0.5. This may indicate that the line and time averaging lack adequate detection of bubbles in slug flow.

2.4.2 Flow regime map

The flow regime maps obtained from the observations of each elevation at four different conditions are shown in Fig. 2.4 through Fig. 2.7. These results were visually identified with the aid of high-speed images, the schematic diagram and the two-phase flow conditions which are studied in the past (Wu et al., 2017; Shibata et al., 2022). Local superficial gas velocities were employed to consider the difference in gas density at each elevation. As a comparison with conventional flow regime maps, the well-known Mishima-Ishii's flow regime transition criteria (Mishima and Ishii, 1984) for upward gas-liquid two-phase flow in the round pipe are also shown in the figures, given by the following equation.

$$j_f = \left(\frac{1}{\alpha C_0} - 1\right) j_g + \frac{v_{gj}}{C_0} \tag{2-36}$$

Where C_0 and v_{gj} are equation (2-11) and (2-12), and the critical void fraction (α) of 0.3 is applied for the present flow regime transition criteria of bubbly-slug transition. Physical properties of fluids were determined by each experimental condition.

The obtained results show good agreement with conventional models at all elevation under tap water conditions of low and high pressure (Fig. 2.4 and Fig. 2.5). As the elevation and high-pressure affect the superficial gas velocity through variation of gas density, the use of local superficial gas velocities results in consideration of height and pressure effects. The flow regime in brine condition shows larger local superficial gas velocity transitioning from bubbly to slug flow compared to tap-water (Fig. 2.6 and Fig. 2.7).

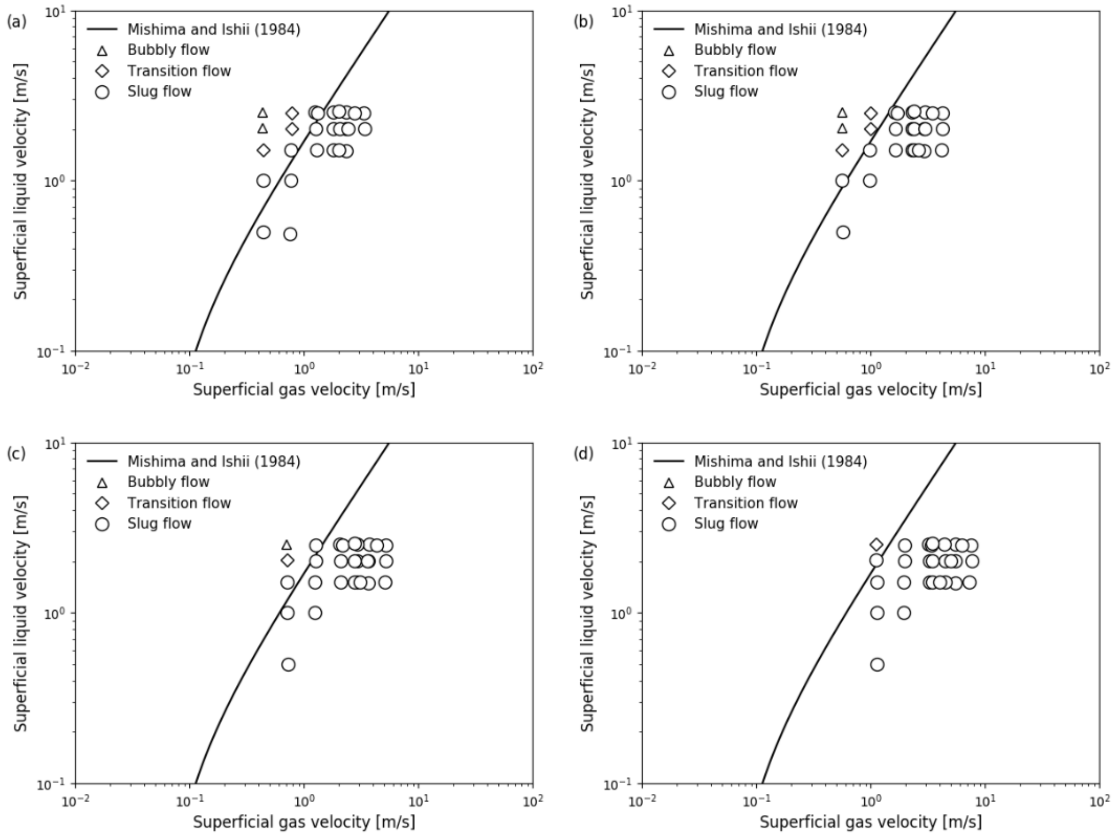

Fig. 2.4. Flow Regime map of P=0 MPaG at (a) 2.7 m, (b) 10.7 m, (c) 17.3 m (d) 25.6 m for tap water in present work.

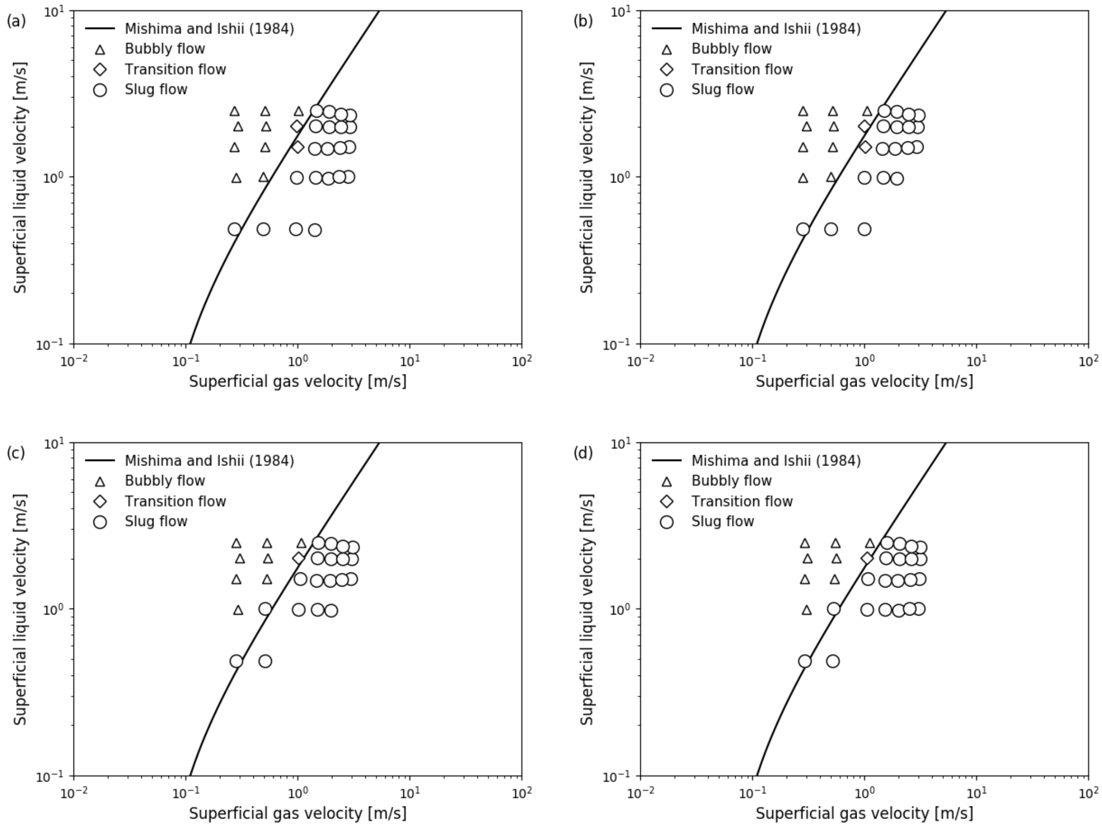

Fig. 2.5. Flow Regime map of P=2.8 MPaG at (a) 2.7 m, (b) 10.7 m, (c) 17.3 m (d) 25.6 m for tap water in present work.

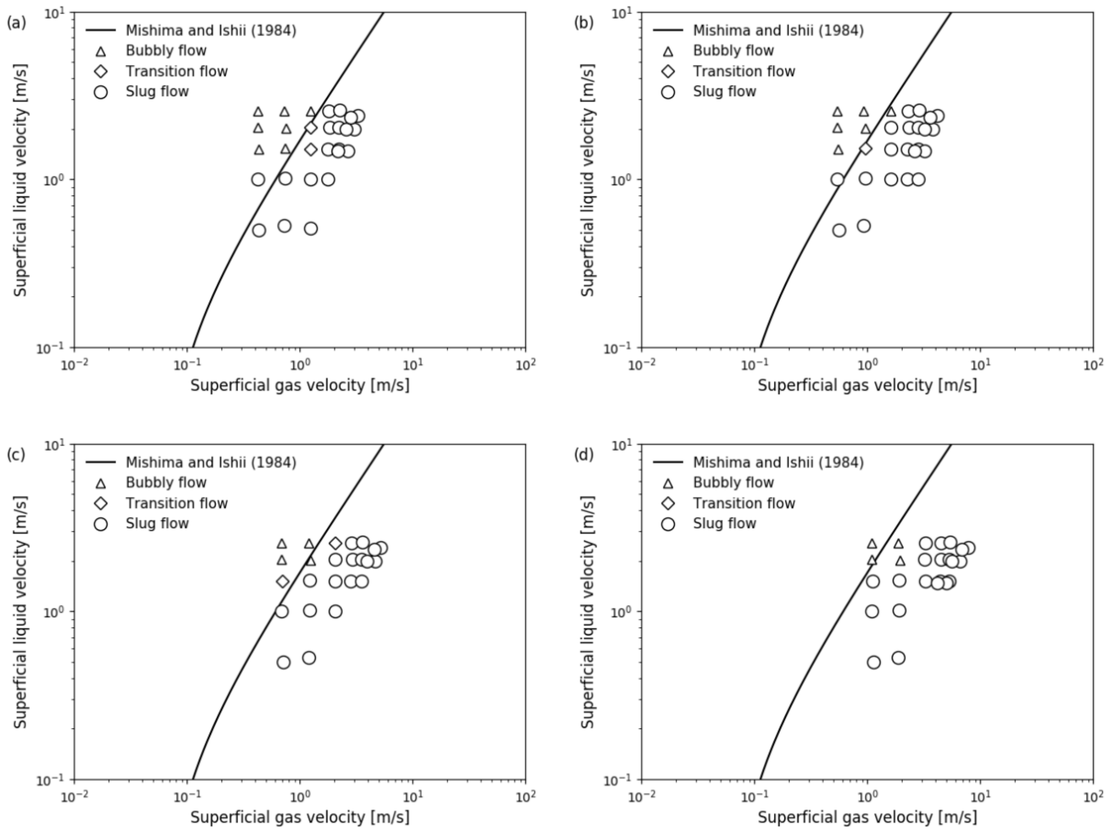

Fig. 2.6. Flow Regime map of P=0 MPaG at (a) 2.7 m, (b) 10.7 m, (c) 17.3 m (d) 25.6 m for brine in present work.

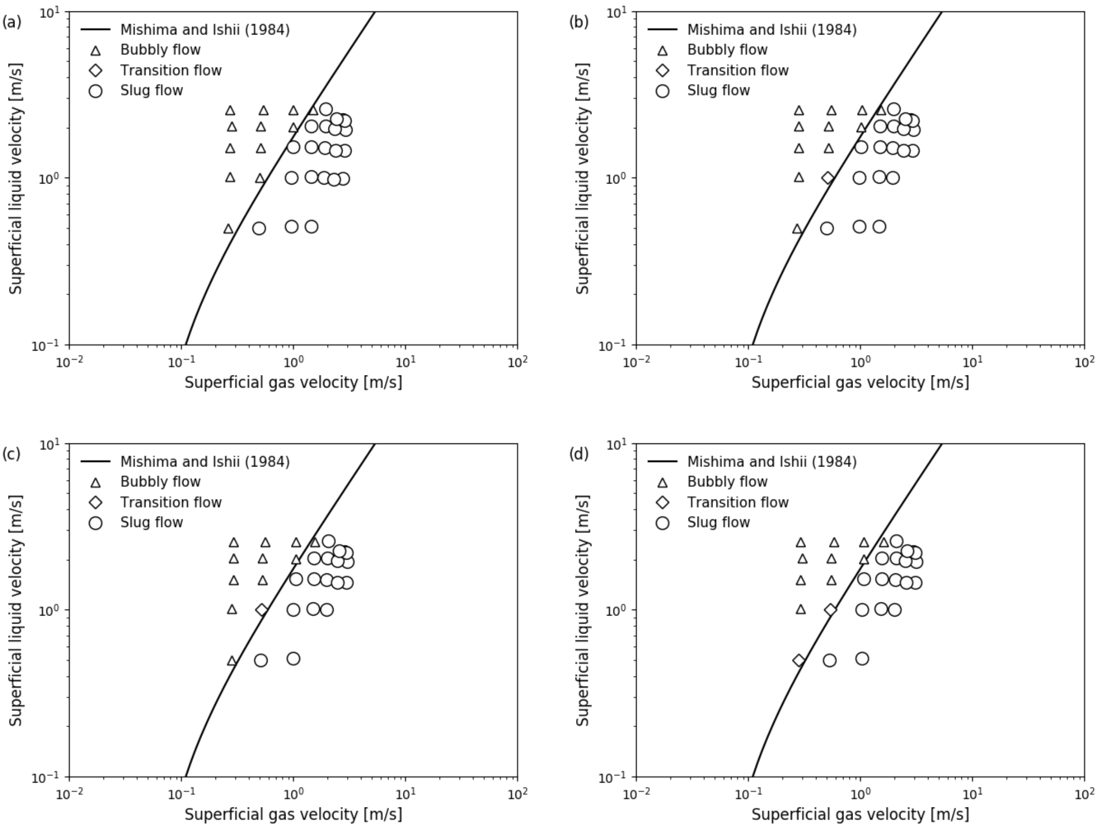

Fig. 2.7. Flow Regime map of P=2.8 MPaG at (a) 2.7 m, (b) 10.7 m, (c) 17.3 m (d) 25.6 m for brine in present work.

The effect of salinity on the flow regime of gas-liquid two-phase flows has been addressed by many researchers. Besagni and Inzoli (2015) indicated from the results of bubble column that the superficial gas velocity of flow regime transition increases with additional salinity, which is due to the inhibition of bubble coalescence (Craig et al., 1993; Del Castillo et al., 2011; Firouzi et al., 2015; Besagni and Inzoli, 2017b). The brine also decreases the distribution of bubble diameters (Besagni and Inzoli, 2017a), and the critical void fraction of bubbly-slug transition increases with the decreasing bubble diameter, implying the increase in superficial gas velocity for bubbly-slug transition (Wu et al., 2017). The present experimental results are consistent with these findings from the previous researchers.

2.4.3 Drift flux model approach

In order to evaluate the experimental results with the drift flux model, the gas velocity against mixture volumetric flux are shown in Fig. 2.8 and Fig. 2.9. The results for superficial liquid velocity of 0.5-2.5 m/s are shown separately for bubbly flow or slug flow, and the equations (2-6), (2-15) and

(2-16) are also shown for each as conventional model. In addition, the local superficial gas velocity is applied to reflect the change in gas density at each elevation which is also shown in the figures. Furthermore, the mixture volumetric flux is faster than the scope of existing model. As shown in Fig. 2.8 and Fig. 2.9, the gas velocity rises with increasing mixture volumetric flux in both bubbly and slug flow conditions. Moreover, since the tendency can be found in the results of different heights, the effect of elevation can be summarized through nondimensionalization,.

For bubbly flow results, low pressure tap water condition of Fig. 2.8 (a) shows good correlation with conventional model. A wide variation of gas velocity is seen in Fig. 2.8 (b) high-pressure tap water condition, and the gas velocity tends to be lower than the existing model in the range of higher mixture volumetric flux. For brine condition, gas velocity is lower than both the tap water results in the low-pressure and the conventional model as shown in Fig. 2.8 (c), and is even lower in the high-pressure condition as shown in Fig. 2.8 (d). Meanwhile, the gas velocity of slug flow tends to be lower than the existing model, regardless of the conditions or superficial liquid velocity.

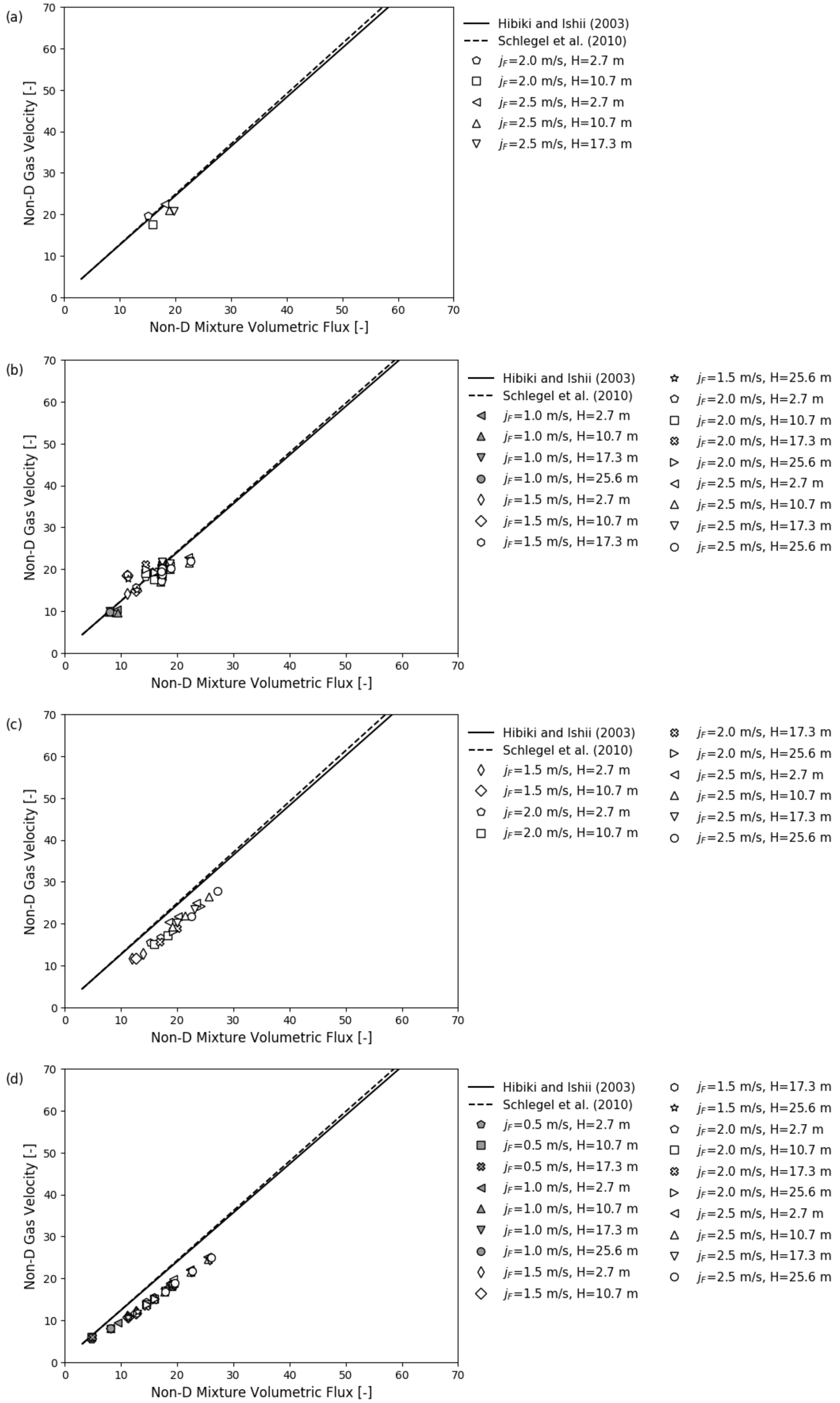

Fig. 2.8. The drift flux model results of bubbly flow all elevation in each condition (a) P=0 MPaG, (b) P=2.8 MPaG for tap water and (c) P=0 MPaG, (d) P=2.8 MPaG for brine.

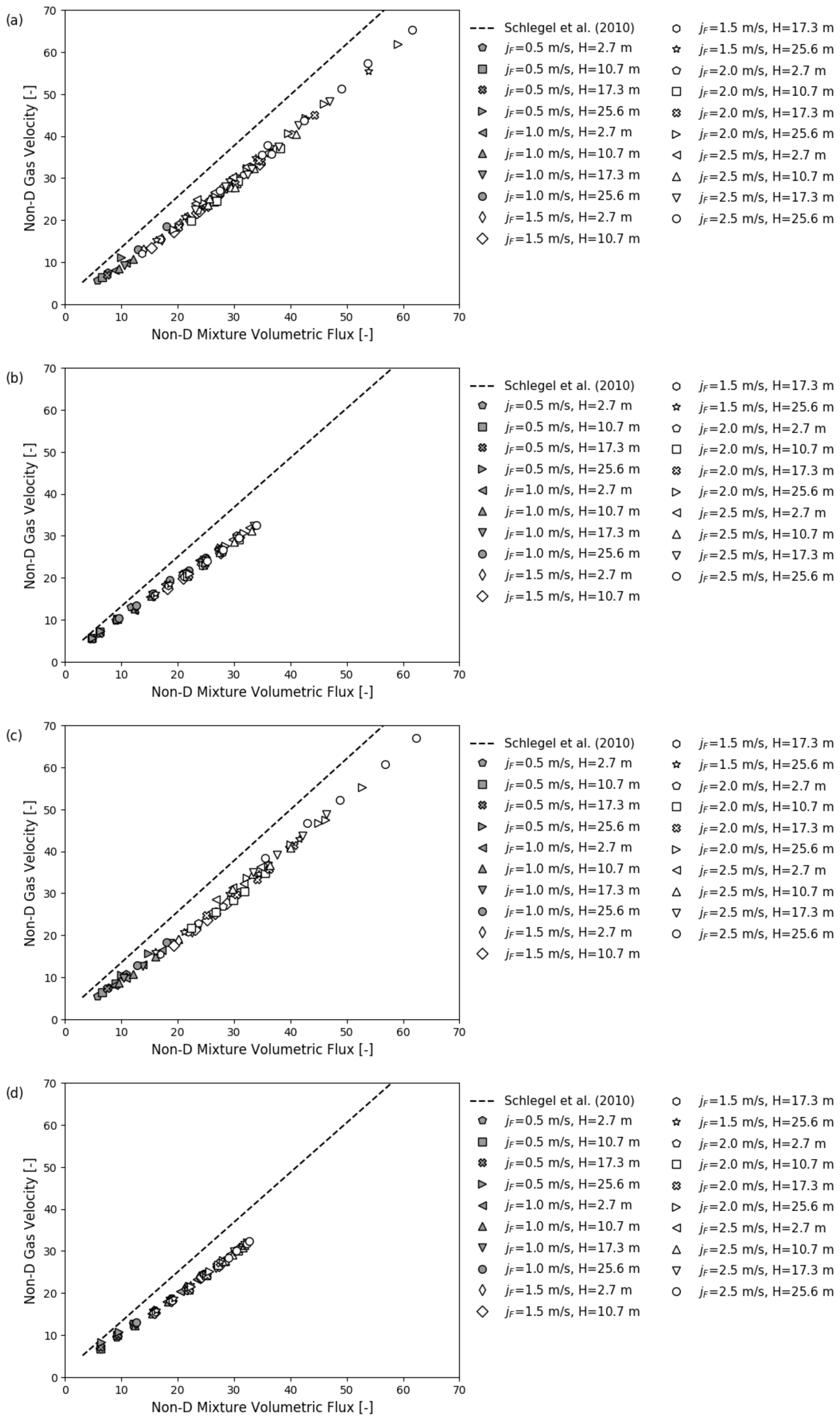

Fig. 2.9. The drift flux model results of slug flow all elevation in each condition (a) P=0 MPaG, (b) P=2.8 MPaG for tap water and (c) P=0 MPaG, (d) P=2.8 MPaG for brine.

2.4.3.1 Model for brine in bubbly flow

Regarding the decrease of gas velocity in brine condition, Quinn et al. (2014) measured the single bubble rise velocity in stagnant solution of inorganic salts. His results showed that bubble rise velocity in high concentrations of brine is lower than that of low concentrations. The reduction of single bubble rise velocity is due to the presence of smaller bubble, and reveals that the decrease in bubble diameters is caused by the inhibition of coalescence attribute to brine. Franken et al. (2019) carried out two-phase natural circulation experiments and showed that the bubble diameter generated in artificial seawater are smaller than those in tap water and that bubble coalescence and formation of slugs are inhibited in the artificial seawater. Therefore, the relationship between salinity and bubble diameter, and between bubble diameter and single bubble rise velocity is important.

First, the following is the correlation between the bubble diameter and the molar concentration C_{tr} at which coalescence is reduced by more than 95% (Marrucci et al., 1967; Marrucci , 1969; Firouzi et al., 2015).

$$C_{tr} = 1.18\upsilon R_g T(\sigma B/R)^{1/2}(\partial\sigma/\partial c)^{-2} \tag{2-37}$$

This correlation indicates that the bubble diameter declines with increasing salinity. The experiment's salinity of 3.5 wt% is 0.61 mol/l hence, the bubble radius is calculated as 0.39 mm based on this correlation. Furthermore, the rise velocity of tiny single bubble in an infinite medium is calculated from the equation of Peebles and Garber (1953) as follows.

$$u_b = 0.33g^{0.76}(\rho_L/\mu_L)^{0.52}R^{1.28} \tag{2-38}$$

From the above equation, bubble rise velocity for the 0.39 mm bubble radius is assumed to be 0.11 m/s. Note that the applicable range of Reynolds number is 2 to 765, and the Reynolds number for a bubble radius of 0.39 mm is 90. Furthermore, Besagni and Inzoli (2017) found that bubbles generated from bubble dispersers in brine moves to the wall surface as they rise, indicating that bubbles are distributed not only in the center but also towards the channel wall. Moreover, the distribution parameter asymptotically approaches unity as the distribution of bubbles becomes uniform from the center to the wall. Therefore, the model with the above single bubble rising rate as the drift velocity and the distribution parameter as unity is shown in the Fig. 2.10 with the experimental results of low and high pressure brine conditions.

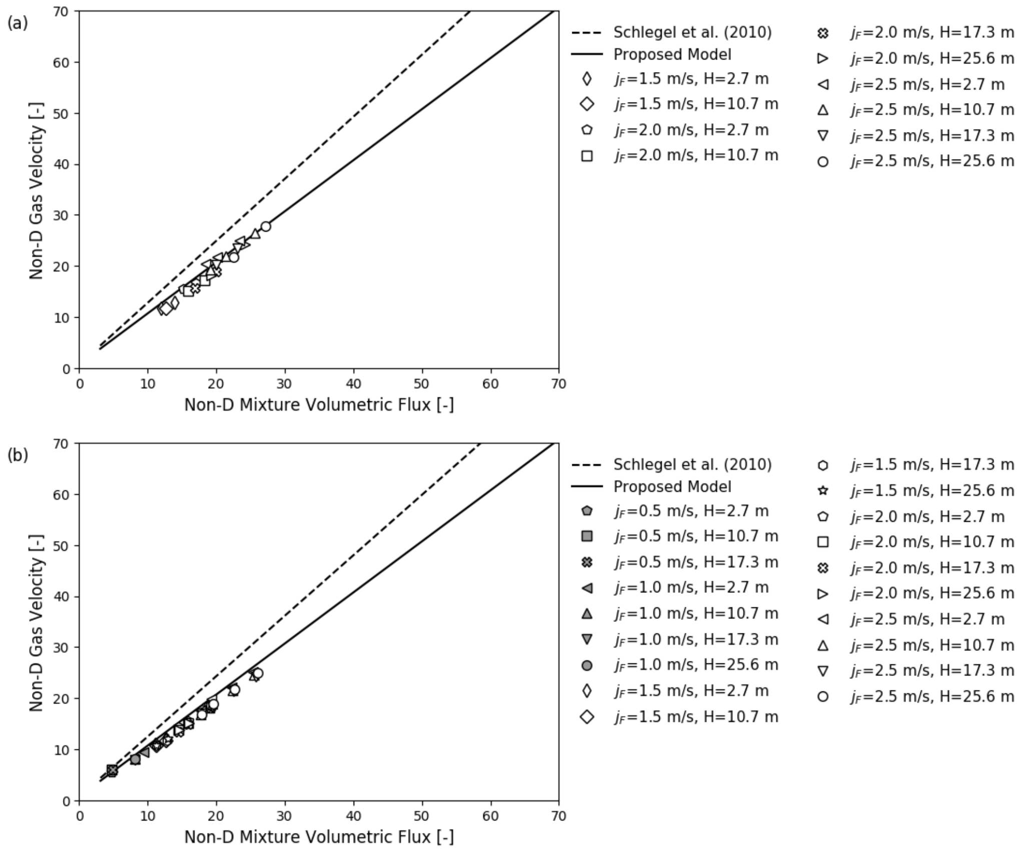

Fig. 2.10. The comparison of proposed model with the results of brine conditions with (a) P=0 MPaG and (b) P=2.8 MPaG.

The result indicates that the proposed model correlates well with the experimental data, thus the bubbly flow in brine condition appears to consist of the rise of small bubbles and the homogenization of bubble distribution. Therefore, the new model with $C_0 = 1$ and $v_{gj} = u_b$, based on equation (2-6), is derived. Meanwhile, although the trend is similar under high-pressure condition, experimental results are slightly lower than the proposed model. Gas-liquid two-phase flows under high-pressure conditions are reported to have smaller bubble diameters than those in atmospheric pressure (Idogawa et al., 1985; Lin et al., 1998), suggesting that the decrease in gas velocity is not only due to the brine but also by the high pressure.

2.4.4 Pressure drop and frictional pressure drops

The results of pressure drop against the local superficial gas velocity measured by differential pressure gauge are shown in Fig. 2.11 and Fig. 2.12. Only the results for slug flow at superficial liquid velocities of 1.5 - 2.5 m/s are presented here.

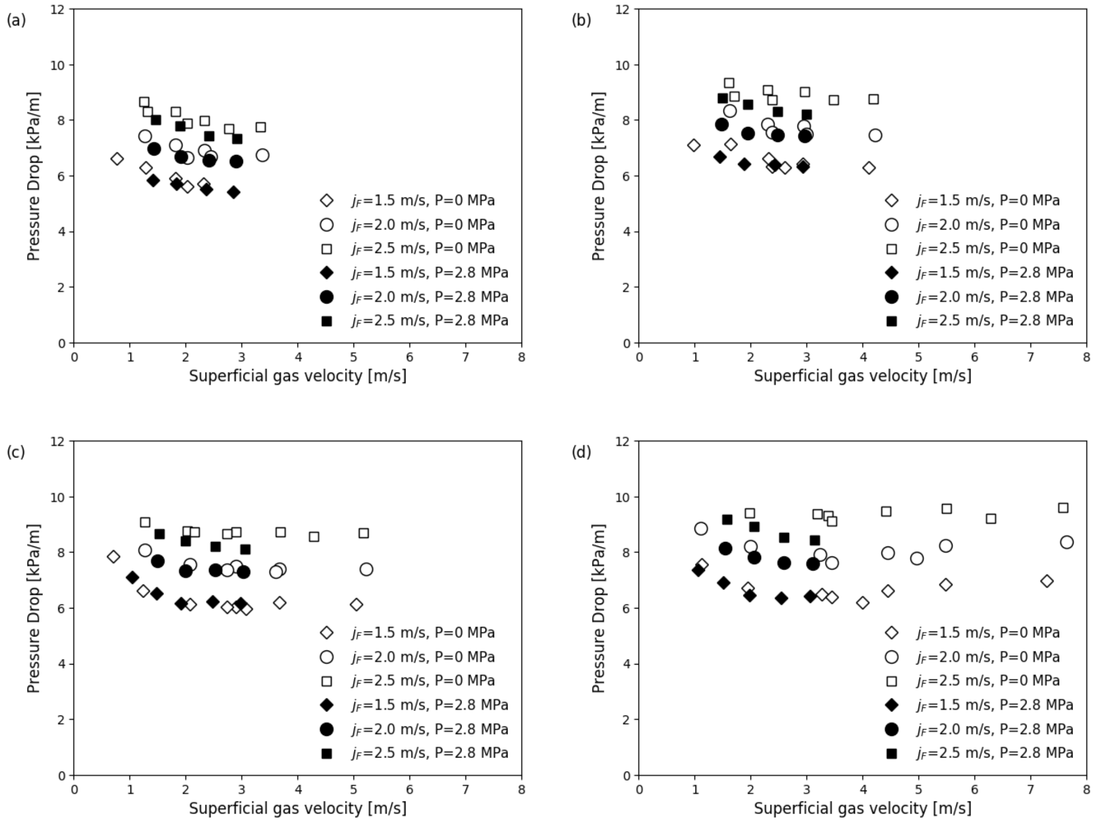

Fig. 2.11. The pressure gradient with tap water at the height of (a) 2.7 m, (b) 10.7 m, (c) 17.3 m and (d) 25.6 m for P=0 MPaG and P=2.8 MPaG in present work.

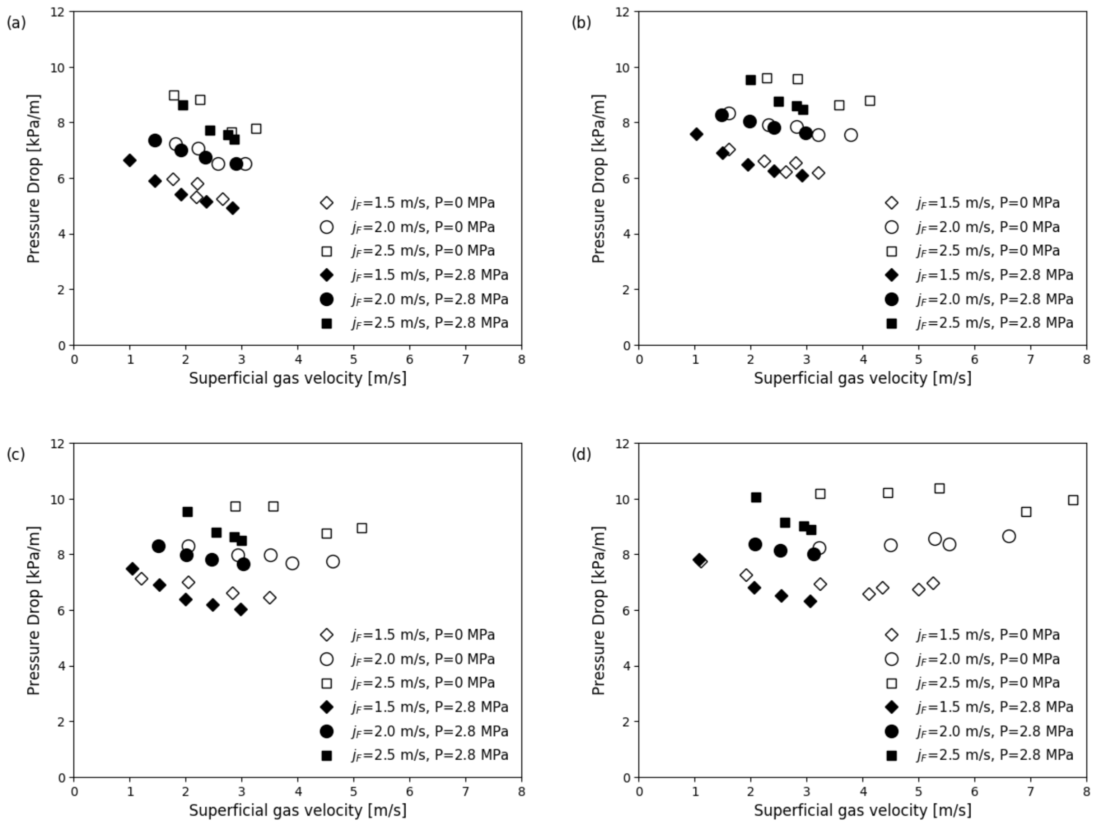

Fig. 2.12. The pressure gradient with brine at the height of (a) 2.7 m, (b) 10.7 m, (c) 17.3 m and (d) 25.6 m for P=0 MPaG and P=2.8 MPaG in present work.

The Fig. 2.11 and Fig. 2.12 shows that the pressure drop behaviors with respect to the superficial liquid velocity or the pipe elevation. Pressure drop slightly increases with salinity and declines with increasing pressure. Furthermore, both effects tend to offset in high-pressure brine conditions. Although the change in local superficial gas velocity is small for high-pressure condition as it rises, the pressure drop of atmospheric pressure condition seems to present an aspect of high-speed range because of the steep increase in local superficial gas velocity.

The frictional pressure drop are derived from the pressure drop and void fraction, and are shown in Fig. 2.13 and Fig. 2.14 with respect to local superficial gas velocity. Furthermore, the results of Lu et al. (2018) for superficial liquid velocity 2 m/s are also shown in Fig. 2.13. Here, the results for slug flow at superficial liquid velocities of 1.5 – 2.5 m/s are presented. The figure indicates that the frictional pressure drop increases with increasing liquid and local gas superficial velocity, or the pipe elevation under all conditions. The results of superficial liquid velocity 2.0 m/s in Fig. 2.13 (a) shows good correlation with the results of Lu et al. (2018) obtained at same liquid velocity. The frictional pressure drop increases with elevation of height regardless of pressure and salinity and barely changes with increasing salinity, and at a high-pressure, it is lower than atmospheric pressure conditions. This suggests that the frictional pressure drop is small depending on the pressure.

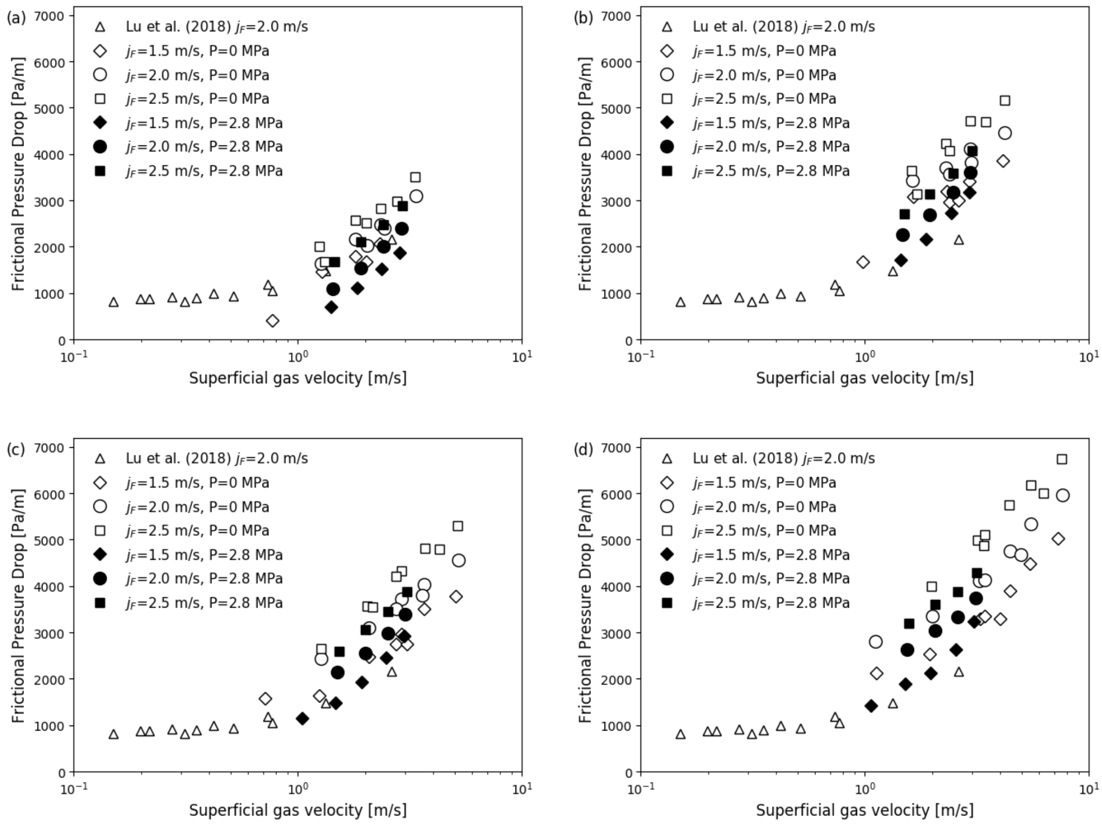

Fig. 2.13. The frictional pressure drop with tap water at the height of (a) 2.7 m, (b) 10.7 m, (c) 17.3 m and (d) 25.6 m for P=0 MPaG and P=2.8 MPaG in present work.

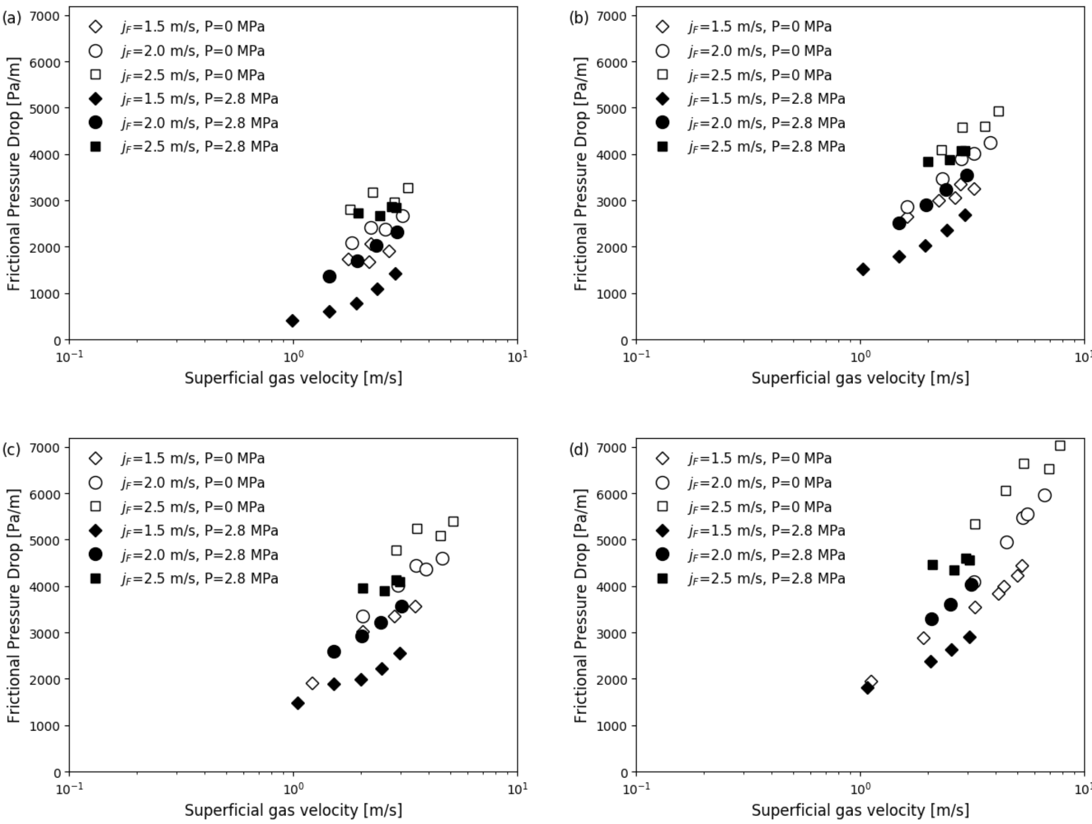

Fig. 2.14. The frictional pressure drop with brine at the height of (a) 2.7 m, (b) 10.7 m, (c) 17.3 m and (d) 25.6 m for P=0 MPaG and P=2.8 MPaG in present work.

2.4.5 Lockhart-Martinelli approach

The two-phase frictional multiplier was calculated with the Lockhart-Martinelli approach from the results of frictional pressure drops and experimental conditions. The results of two-phase frictional multiplier for Martinelli parameter and the calculation of equation (2-33) are shown in Fig. 2.15 through Fig. 2.18. Since both the gas and liquid phases in this experiment are turbulent based on the Reynolds number, C=20 is used for calculation. The parameter C that minimizes the residual sum of squares (RSS) of each results are also shown with the model. Furthermore, the results of Lu et al. (2018) are also shown in Fig. 2.15 (a). The variation of the viscosity coefficient with salinity is included in the calculation of the results. As before, only the results for slug flow at superficial liquid velocities of 1.5 - 2.5 m/s are presented here.

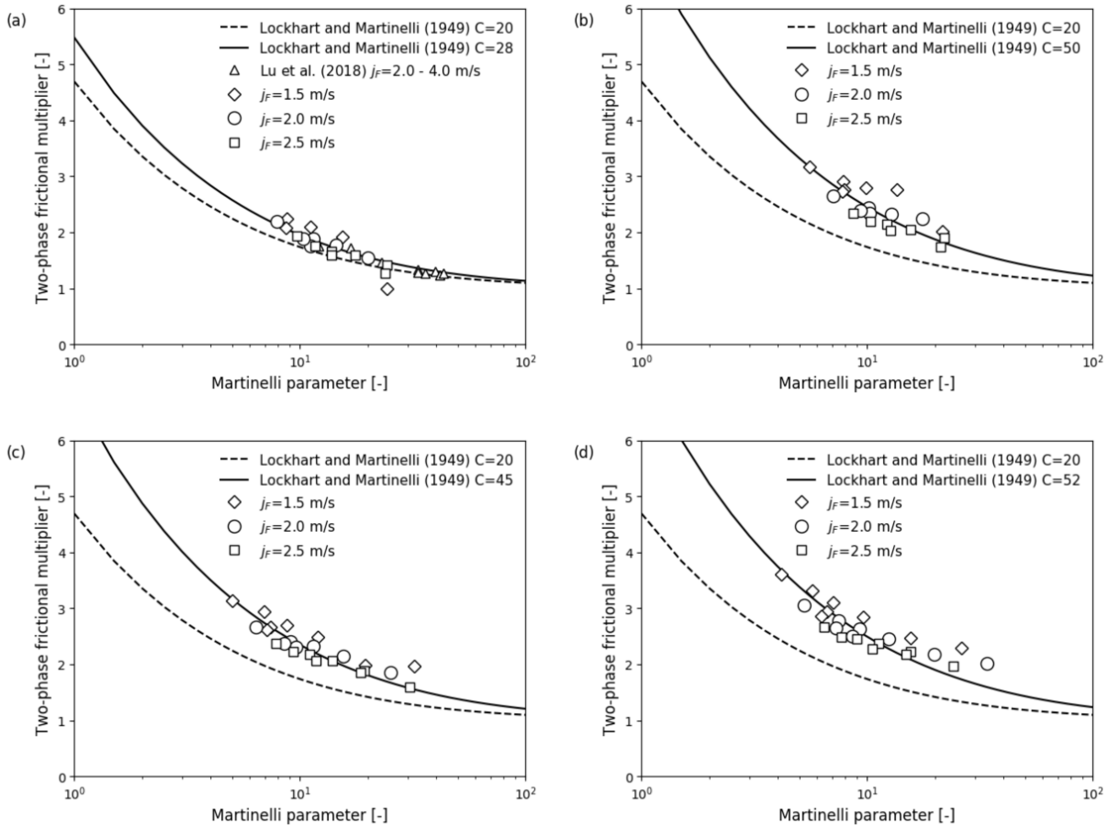

Fig. 2.15. The two-phase frictional multiplier of frictional pressure drops with tap water at the height of (a) 2.7 m, (b) 10.7 m, (c) 17.3 m and (d) 25.6 m for P=0 MPaG in present work. Model of Lockhart and Martinelli (1949), the results of Lu et al. (2018) and the model of optimized parameter C are also shown

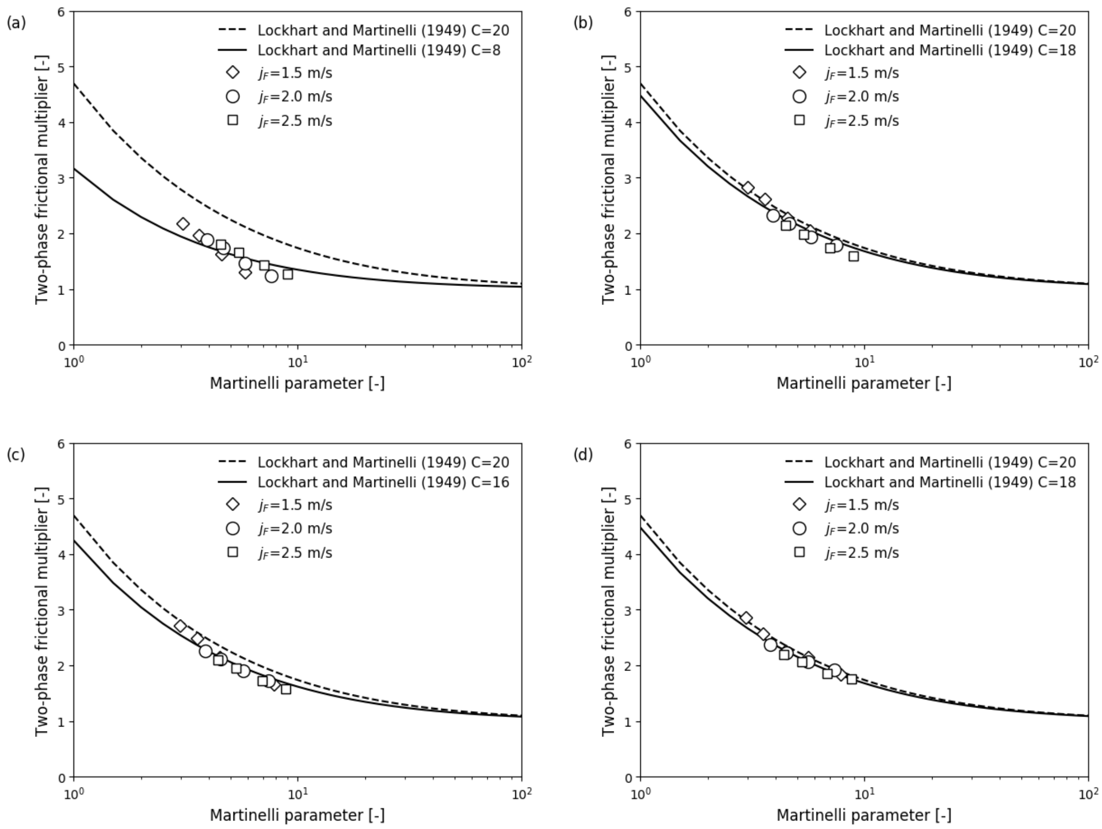

Fig. 2.16. The two-phase frictional multiplier of frictional pressure drops with tap water at the height of (a) 2.7 m, (b) 10.7 m, (c) 17.3 m and (d) 25.6 m for P=2.8 MPaG in present work. The model of optimized parameter C are also shown.

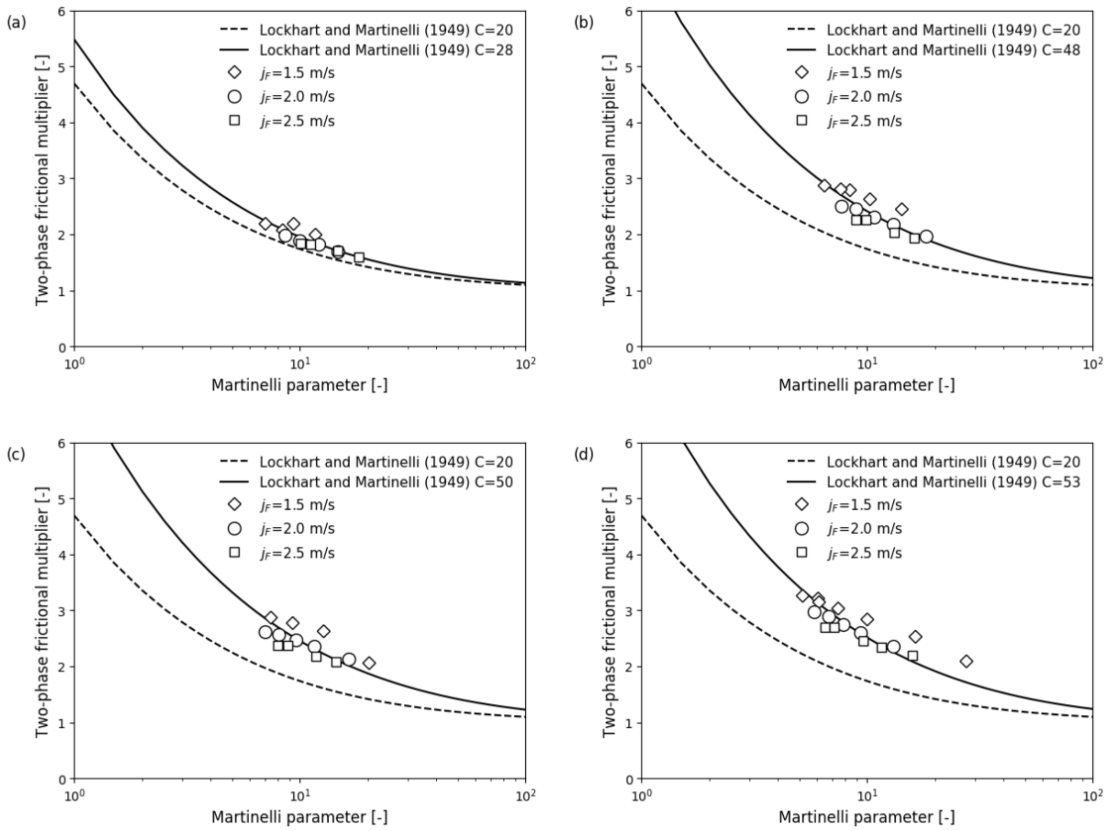

Fig. 2.17. The two-phase frictional multiplier of frictional pressure drops with brine at the height of (a) 2.7 m, (b) 10.7 m, (c) 17.3 m and (d) 25.6 m for P=0 MPaG in present work. The model of optimized parameter C are also shown

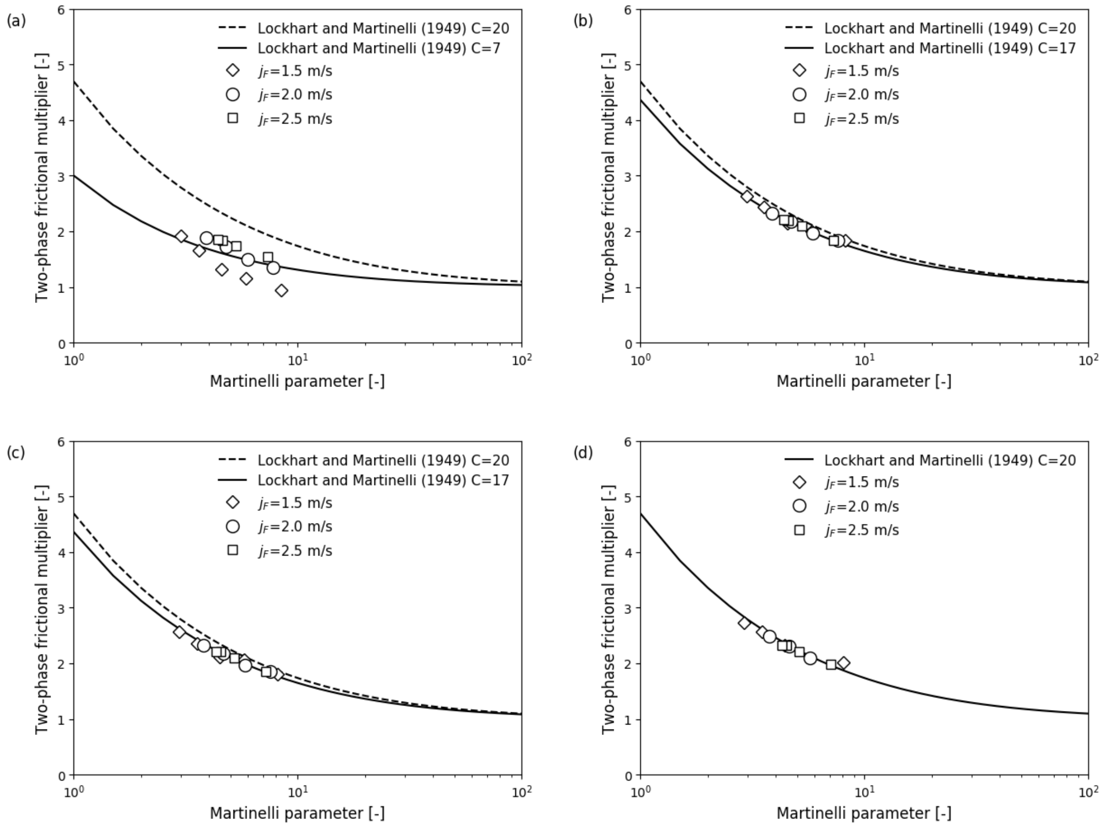

Fig. 2.18. The two-phase frictional multiplier of frictional pressure drops with brine at the height of (a) 2.7 m, (b) 10.7 m, (c) 17.3 m and (d) 25.6 m for P=2.8 MPaG in present work. The model of optimized parameter C are also shown

As shown in the figures, the two-phase frictional multiplier increases as the local superficial gas velocity increases, i.e., as the Martinelli parameter decreases, for all conditions. The conditions in Fig. 2.15 (a) show good correlation with the results of Lu et al. (2018) obtained at superficial liquid velocity of 2-4 m/s and the conventional model, regardless of the superficial liquid velocity. The two-phase frictional multiplier increases with elevation of height, in spite of pressure and salinity and changes slightly with increasing salinity and that under high-pressure is lower than atmospheric pressure conditions. This suggests that compared to the existing model, two-phase frictional multiplier tends to be smaller depending on the pressure.

2.4.5.1 Model for parameter C

Hereafter, the relationship between the optimal parameter C for each condition and equation (2-34) is discussed and the new model is proposed. Chisholm (1967) indicates that Z is a parameter that depends on the density of gas and liquid, etc. Here, in order to incorporate the results of brine and high-pressure conditions, Z is redefined as a function of not only the gas and liquid density, but also the Eötvös number, viscosity number which is equation (2-20), and the constant f_s.

$$Z' = EoN_{\mu f} f_s \left(\rho_f / \rho_g\right)^{1/2} \tag{2-39}$$

To establish the new model, the newly defined Z' was substituted into Z in equation (2-34) to obtain the constant f_s that reproduces the optimum parameters C of experiment results for tap water and brine using the minimum value of RSS. As a result, the constants for tap water and brine are 3 and 2.8 each, and their correlation are shown in Fig. 2.19. Thus, a new equation for frictional pressure drops considering salinity and pressure, based on equation (2-34) was established by using this new parameter Z' which is equation (2-39).

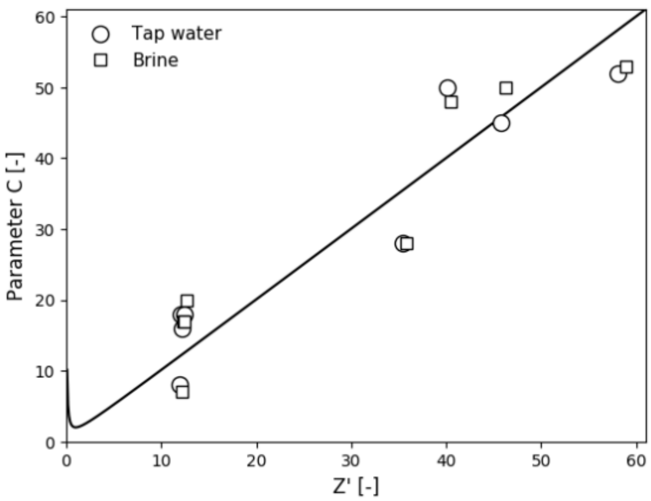

Fig. 2.19. The correlation of optimum parameter C and parameter Z'

2.5 Conclusions

This is the rare study that investigated the void fraction and pressure drop of nitrogen-brine two-phase flows with high superficial gas velocity that rise long length under high-pressure conditions, which considers the offshore methane hydrate production test. The experiment is conducted with j_g =0.25-3 m/s of inlet superficial gas velocity and superficial liquid velocity of j_f = 0.5-2.5 m/s under low and high pressure (0-2.8 MPaG) condition, and the elevation ranges from 2.7 - 25.3 m. The results of void fraction and frictional pressure drop were compared with conventional models and a new model for high-pressure brine is also developed with these results. Based on these results, the following conclusions were drawn and expected to contribute to the studies of production engineering here after:

1. The flow regime of upward gas-liquid two-phase flow shows good correlation with the conventional model in tap water condition, meanwhile, the transitioning superficial gas velocity of bubbly to slug flow in brine is faster than tap water condition. This is due to the increase of critical void fraction that transits from bubbly to slug flow resulting from the decrease of bubble diameter caused by added salts.
2. The void fraction obtained from experiments under certain conditions is compared with conventional drift-flux model. The gas velocity of bubbly flow showed good correlation with the existing model under low-pressure tap water conditions, but was lower for all regions under brine. With the inhibition of coalescence by brine, the gas velocity is lower than the conventional model because of the uniformity of bubble distribution and lower bubble rise velocity due to the reduction in bubble diameter. Thus, a new model with $C_0 = 1$ and $v_{gj} = u_b$ based on dimensionless drift flux model, is proposed.
3. The frictional pressure drop estimated from the experiment were compared with conventional model as two-phase flow friction multiplier, and a good correlation was attained at low elevation under low-pressure tap water conditions. The two-phase flow friction multiplier increases with elevated height, while decreases with increased system pressure, and the new model with Z' based on Chisholm parameter was developed to reflect this result.

Bibliography

Besagni, G., Inzoli, F., 2015. Influence of electrolyte concentration on holdup, flow regime transition and local flow properties in a large scale bubble column. J. Phys.: Conf. Ser. 655, 012039. https://doi.org/10.1088/1742-6596/655/1/012039

Besagni, G., Inzoli, F., 2017a. The effect of electrolyte concentration on counter-current gas–liquid bubble column fluid dynamics: Gas holdup, flow regime transition and bubble size distributions. Chemical Engineering Research and Design 118, 170–193. https://doi.org/10.1016/j.cherd.2016.12.012

Besagni, G., Inzoli, F., 2017b. The effect of liquid phase properties on bubble column fluid dynamics: Gas holdup, flow regime transition, bubble size distributions and shapes, interfacial areas and foaming phenomena. Chemical Engineering Science, 13th International Conference on Gas-Liquid and Gas-Liquid-Solid Reactor Engineering 170, 270–296. https://doi.org/10.1016/j.ces.2017.03.043

Chisholm, D., 1967. A theoretical basis for the Lockhart-Martinelli correlation for two-phase flow. International Journal of Heat and Mass Transfer 10, 1767–1778. https://doi.org/10.1016/0017-9310(67)90047-6

Craig, V.S.J., Ninham, B.W., Pashley, R.M., 1993. Effect of electrolytes on bubble coalescence. Nature 364, 317–319. https://doi.org/10.1038/364317a0

Del Castillo, L.A., Ohnishi, S., Horn, R.G., 2011. Inhibition of bubble coalescence: effects of salt concentration and speed of approach. J Colloid Interface Sci 356, 316–324. https://doi.org/10.1016/j.jcis.2010.12.057

Duchateau, C., Broseta, D., 2012. A simple method for determining brine–gas interfacial tensions. Advances in Water Resources 42, 30–36. https://doi.org/10.1016/j.advwatres.2012.03.008

Firouzi, M., Nguyen, A.V., 2014. Novel Methodology for Predicting the Critical Salt Concentration of Bubble Coalescence Inhibition. J. Phys. Chem. C 118, 1021–1026. https://doi.org/10.1021/jp409473g

Firouzi, M., Howes, T., Nguyen, A.V., 2015. A quantitative review of the transition salt concentration for inhibiting bubble coalescence. Advances in Colloid and Interface Science, Reinhard Miller, Honorary Issue 222, 305–318. https://doi.org/10.1016/j.cis.2014.07.005

Franken, D., Ahmed, Z., Eckels, Seth, Eckels, Steven, Bindra, H., 2019. Impact of dissolved salts on two-phase flow and boiling heat transfer in a natural circulation loop. Chemical Engineering Science 206, 463–470. https://doi.org/10.1016/j.ces.2019.05.046

Hibiki, T., Ishii, M., 2003. One-dimensional drift–flux model for two-phase flow in a large diameter pipe. International Journal of Heat and Mass Transfer 46, 1773–1790. https://doi.org/10.1016/S0017-9310(02)00473-8

Hironaka, S., Fujisawa, Y., Manabe, S., Inoue, G., Matsukuma, Y., Minemoto, M., 2011. Study on the Drag Force Coefficient between Gas and Liquid on the Gas-Lift System to Recover the Methane Hydrate. Journal of Power and Energy Systems 5, 388–399. https://doi.org/10.1299/jpes.5.388

Idogawa, K., Ikeda, K., Fukuda, T., Morooka, S., 1985. Behavior of Bubbles in a Bubble Column under High Pressure for Air-Water System. Kagaku Kogaku Ronbunshu 11, 253–258. https://doi.org/10.1252/kakoronbunshu.11.253

Ishii, M., 1977. ONE-DIMENSIONAL DRIFT-FLUX MODEL AND CONSTITUTIVE EQUATIONS FOR RELATIVE MOTION BETWEEN PHASES IN VARIOUS TWO-PHASE FLOW REGIMES. ANL 77, 67.

Jiang, M., Liu, J., Kwok, C.Y., Shen, Z., 2018. Exploring the undrained cyclic behavior of methane-hydrate-bearing sediments using CFD–DEM. Comptes Rendus Mécanique 346, 815–832. https://doi.org/10.1016/j.crme.2018.05.007

Kataoka, I., Ishii, M., 1987. Drift flux model for large diameter pipe and new correlation for pool void fraction. International Journal of Heat and Mass Transfer 30, 1927–1939. https://doi.org/10.1016/0017-9310(87)90251-1

Konno, Y., Jin, Y., Shinjou, K., Nagao, J., 2014. Experimental evaluation of the gas recovery factor of methane hydrate in sandy sediment. RSC Adv. 4, 51666–51675. https://doi.org/10.1039/C4RA08822K

Li, X.-Y., Li, X.-S., Wang, Y., Zhang, Y., 2020. Optimization of the Production Pressure for Hydrate Dissociation by Depressurization. Energy Fuels 34, 4296–4306. https://doi.org/10.1021/acs.energyfuels.0c00076

Lin, T.-J., Tsuchiya, K., Fan, L.-S., 1998. Bubble flow characteristics in bubble columns at elevated pressure and temperature. AIChE Journal 44, 545–560. https://doi.org/10.1002/aic.690440306

Lu, C., Kong, R., Qiao, S., Larimer, J., Kim, S., Bajorek, S., Tien, K., Hoxie, C., 2018. Frictional pressure drop analysis for horizontal and vertical air-water two-phase flows in different pipe sizes. Nuclear Engineering and Design 332, 147–161. https://doi.org/10.1016/j.nucengdes.2018.03.036

Mandalahalli, M.M., Wagner, E.C., Portela, L.M., Mudde, R.F., 2020. Electrolyte effects on recirculating dense bubbly flow: An experimental study using X-ray imaging. AIChE Journal 66, e16696. https://doi.org/10.1002/aic.16696

Marrucci, G., Nicodemo, L., 1967. Coalescence of gas bubbles in aqueous solutions of inorganic electrolytes. Chemical Engineering Science 22, 1257–1265. https://doi.org/10.1016/0009-2509(67)80190-8

Marrucci, G., 1969. A theory of coalescence. Chemical Engineering Science 24, 975–985. https://doi.org/10.1016/0009-2509(69)87006-5

Mishima, K., Ishii, M., 1984. Flow regime transition criteria for upward two-phase flow in vertical tubes. International Journal of Heat and Mass Transfer 27, 723–737. https://doi.org/10.1016/0017-9310(84)90142-X

Nayar, K.G., Sharqawy, M.H., Banchik, L.D., Lienhard V, J.H., 2016. Thermophysical properties of seawater: A review and new correlations that include pressure dependence. Desalination 390, 1–24. https://doi.org/10.1016/j.desal.2016.02.024

Orvalho, S., Ruzicka, M.C., Drahos, J., 2009. Bubble Column with Electrolytes: Gas Holdup and Flow Regimes. Ind. Eng. Chem. Res. 48, 8237–8243. https://doi.org/10.1021/ie900263d

Ouchi, H., Yamamoto, K., Akamine, K., Kano, S., Naiki, M., Tamaki, M., Ohtsuki, S., Kanno, T., Tenma, N., 2022. Numerical History-Matching of Modeling and Actual Gas Production Behavior and Causes of the Discrepancy of the Nankai Trough Gas-Hydrate Production Test Cases. Energy Fuels 36, 210–226. https://doi.org/10.1021/acs.energyfuels.1c02931

Peebles, F.N., Garber, H.J., 1953. Studies on the motion of gas bubbles in liquids. Chem. Eng. Prog. 49, 88–97.

Quinn, J.J., Maldonado, M., Gomez, C.O., Finch, J.A., 2014. Experimental study on the shape–velocity relationship of an ellipsoidal bubble in inorganic salt solutions. Minerals Engineering 55, 5–10. https://doi.org/10.1016/j.mineng.2013.09.003

Ribeiro Jr., C.P., Mewes, D., 2007. The influence of electrolytes on gas hold-up and regime transition in bubble columns. Chemical Engineering Science 62, 4501–4509. https://doi.org/10.1016/j.ces.2007.05.032

Sawai, T., Kaji, M., Kasugai, T., Nakashima, H., Mori, T., 2004. Gas–liquid interfacial structure and pressure drop characteristics of churn flow. Experimental Thermal and Fluid Science 28, 597–606. https://doi.org/10.1016/j.expthermflusci.2003.09.003

Schlegel, J., Hibiki, T., Ishii, M., 2010. Development of a comprehensive set of drift-flux constitutive models for pipes of various hydraulic diameters. Progress in Nuclear Energy 52, 666–677. https://doi.org/10.1016/j.pnucene.2010.03.007

Shannak, B.A., 2008. Frictional pressure drop of gas liquid two-phase flow in pipes. Nuclear Engineering and Design 238, 3277–3284. https://doi.org/10.1016/j.nucengdes.2008.08.015

Sharqawy, M.H., Lienhard, J.H., Zubair, S.M., 2010. Thermophysical properties of seawater: a review of existing correlations and data. Desalination and Water Treatment 16, 354–380. https://doi.org/10.5004/dwt.2010.1079

Shiba, M., Yamazaki, Y., 1966. Pressure Drop of Vertical Air-Water Flow. Transactions of the Japan Society of Mechanical Engineers 32, 1231–1238. https://doi.org/10.1299/kikai1938.32.1231

Shibata, N., Miwa, S., Sawa, K., Takahashi, M., Murayama, T., Tenma, N., 2022. Identification of high-pressure two-phase flow regime transition using image processing and deep learning. Journal of Natural Gas Science and Engineering 102, 104560. https://doi.org/10.1016/j.jngse.2022.104560

Wiegand, G., Franck, E.U., 1994. Interfacial tension between water and non-polar fluids up to 473 K and 2800 bar. Berichte der Bunsengesellschaft für physikalische Chemie 98, 809–817. https://doi.org/10.1002/bbpc.19940980608

Wu, B., Firouzi, M., Mitchell, T., Rufford, T.E., Leonardi, C., Towler, B., 2017. A critical review of flow maps for gas-liquid flows in vertical pipes and annuli. Chemical Engineering Journal 326, 350–377. https://doi.org/10.1016/j.cej.2017.05.135

Zhou, M., Soga, K., Yamamoto, K., 2020. Upscaling techniques for fully coupled THM simulation and application to hydrate gas production tests. Computers and Geotechnics 124, 103596. https://doi.org/10.1016/j.compgeo.2020.103596

Zuber, N., Findlay, J.A., 1965. Average Volumetric Concentration in Two-Phase Flow Systems. Journal of Heat Transfer 87, 453–468. https://doi.org/10.1115/1.3689137

3 Objective flow regime identification with supervised learning

3.1 Introduction

Approaches to identify the flow regime includes differential pressure fluctuation, measurement of void fraction fluctuation and flow photography (Wu et al, 2017). The differential pressure fluctuation is the simple method, but due to the influence of gas entering the impulse line, the identification of flow regime becomes difficult. Measuring the fluctuation of void fraction, which includes probability density function (PDF), can provide identification results that are less subjective than flow photography, but in the case of using electrode probe or impedance meter to measure the void fraction, the effect of intrusiveness to gas-liquid two-phase flow and the installation in the pipe make it difficult to maintain the sealing, especially under high-pressure conditions. While flow photography is non-intrusive and non-invasive, the identification results are greatly influenced by the subjectivity of observer. Although there are merits and weak points in each method identifying the flow regime with void fraction PDF (Pan et al., 2016) using a conductivity probe is not practical for the present condition due to the limitation of inserting the instrumentation into the high-pressure experimental apparatus. Therefore, identifying the flow regime by the image acquired from the visualization port is necessary. However, the visual identification of flow regime tends to be subjective, and an objective identification method is required. Hence, in the present research, the high-pressure two-phase flow experiment was conducted to obtain flow regimes and an adaptation of the CNN-based deep learning model with high-speed images was considered in order to conduct flow regime identification by overcoming the above two issues. The classification model was developed from the acquired image data to identify the flow pattern in a data-driven approach.

3.1.1 Machine learning and convolutional neural networks

This section will review recently published works on two-phase flow using a machine learning approach. There are several studies on the application of deep learning to bubble detection in bubbly flows. Poletaev et al., 2020 used the convolutional denoising autoencoder for preprocessing and CNN to detect bubbles and calculated the bubble diameter distribution. Haas et al., 2020 have established the BubCNN bubble detector that have learned bubbles generated by BubGAN (Fu and Liu, 2019), which enables detection of bubble location and shape. Torisaki and Miwa, 2020a and 2020b, used CNN-based object detection to extract the features of bubbly flow, and calculated the void fraction and surface area of bubbles from the extracted data. These studies have contributed to the application of CNN to gas-liquid two-phase flows by successfully detecting bubbles in bubbly flow. Alternatively, the detection of bubble coalescence and decomposition and the identification of the intermittent flow regime, such as slug flow, pose challenges. Therefore, these methods are difficult to apply to transition from bubbly to slug flow and have not been deployed to identify flow regime such as bubbly flow and slug flow.

On the other hand, some existing works report a technique to reconstruct a single image from the sequential time-frame images to analyze flow conditions. Borhani et al. (2010) and Goda et al. (2019) have created the image merged from the horizontal arrangement of a vertical strip of sequential high-speed images. This method i.e. time-strip methods showed good performance for visualizing interfacial wave structure. However, applying this method for high-pressure two-phase flow conditions remains challenging. A narrow observatory sight window limits the filming range of gas-liquid two-phase flow under high-pressure conditions due to the pressure resistance. Thus, through the devise of the time-strip methods, this approach allows us to capture the intermittent flow regime in static images, which can be combined with CNN to construct the novel flow regime identification methods.

Studies using machine learning to identify the flow regime of gas-liquid two-phase flow from the sequential images in the past are shown here after. Zhou et al. (2008) has identified a two-phase flow regime with machine learning technique after extracting moment invariants from the high-speed sequential images as flow features (Ming-Kuei, 1962). These features were reduced and optimized through rough sets theory (Pawlak, 1982). Shanthi et al. (2017), based on 20 flow regime images, has classified a two-phase flow regime with machine learning using the features extracted by the fuzzy logic (Shi, 2007). Also, Xiao et al, (2018) used the fuzzy logic and support vector machine (SVM) with a principal component analysis (PCA) to identify the flow regime of upward gas-liquid two-phase flow in the vertical mini-channel. Futhermore, Zhang et al. (2020) has identified the flow regime of horizontal gas-liquid two-phase flow using velocity contour images and CNN. In order to deal with the intermittency of slug flow regime from still images, Sasaki et al. (2019) has trained the Convolutional Long-Short Term Memory model with a stack of 30 images obtained from the sequential image and showed reasonable accuracy at atmospheric pressure condition. Although these studies have demonstrated high accuracy of identification for flow regime, the studies that quantify the transitional flow patterns are scarce.

Thus, even though the method for identifying the flow regime through the machine learning approach has merit, few studies have quantified flow regime using CNN, which is less subject and provide high identification accuracy for static images. Hence, this study considers the new flow regime identification method using CNN and the single image generated by the time-strip method (Borhani et al., 2010) applicable for high-pressure two-phase flow conditions. Unlike the conventional studies that uses deep learning to detect bubbles in bubbly flow, this new method merges a portion of sequential images of gas-liquid two-phase flow into single image to capture the dynamics of gas-liquid two-phase flow seen in the sequential images, and identifies the flow regime from the obtained images using deep learning, which shows high identification ability in static images. The newly developed model will be used to classify input database into bubbly, bubbly-slug transition, and slug flow regimes, and its performance will be assessed.

For identifying the flow regime by models in general, the region of each flow regime is delimited by the boundary of flow conditions. When these models are used to identify the flow regimes, it is understood that the flow regime changes instantaneously at the transition boundary, but in reality, the flow regime transition, like bubbly to slug flow, takes place gradually at the boundary. In RELAP5, a safety analysis code for nuclear systems, an accurate theoretical model of flow regime transitions is required for highly accurate safety analysis calculations (Zhang et al., 2017). And given the nature of non-instantaneous flow pattern transitions, complement the theoretical models by quantifying flow regime transitions is important. A similar completion is expected in Hasan and Kabir model, which simulates bottom-hole pressure with flow regimes. In this regard, identifying not only developed flow regimes but also transition states is necessary and transitional region is attracting attention. Thus, the quantitative evaluation of the flow regime transition, which has only been studied through visual observation in the past (Wu et al., 2017), has been performed using a machine learning approach.

3.2 Methodology

The sequential images obtained from the recording were utilized for the CNN model development and the overall diagram of the development, which the detail is shown here after, is depicted in the flow chart shown in Fig. 3.1.

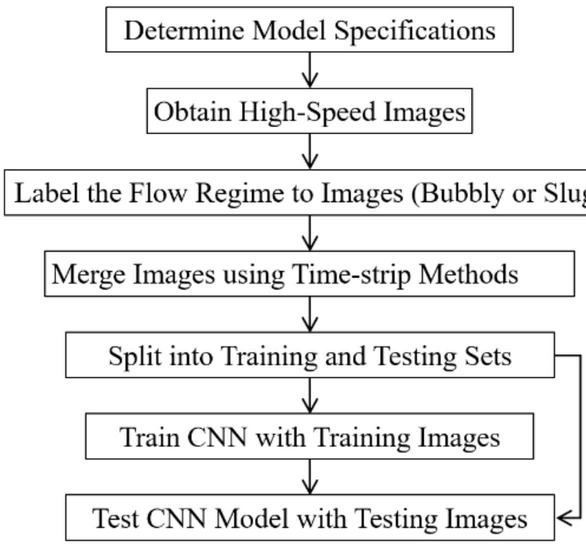

Fig. 3.1. The flow chart showing the overall development of the CNN model for current study.

The illustration of the present identification method is depicted in Fig. 3.2. The unique part of the present method is that the sequential image of the flow regime is converted into a single image and directly used for CNN model development. In the past, several studies using CNN for two-phase flow feature extractions are reported. The previous studies utilizing the object detection techniques using deep learning to slug flow have shown that the CNNs have difficulty identifying cap/ slug bubbles in a single image (Torisaki and Miwa, 2020a, Torisaki and Miwa, 2020b). In the conventional method, hundreds of units, where a single unit is defined as a stack of multiple images decomposed from the sequential image, are suggested for training and identification (Shanthi and Pappa, 2017). In the current method, however, the sequential images of the flow regime are merged into a single image by the time-strip method (Borhani et al., 2010), where a partial image is extracted from each frame and integrated vertically in a time-series order. An advantage of generating a single merged image is that it can contain various features of the gas-liquid interface, such as bubble frequency, interfacial wave evolution, etc. (Kazi et al., 2021). In addition, the intermittent flow behavior seen in the slug flow regime, where Taylor bubble and liquid slug co-exist, can be fully captured using this method (Shibata et al., 2021). In the present study, about 200 merged images were used during the CNN model training. In addition, the model is trained with a single image per unit, unlike conventional methods. The identification result is obtained by inputting the merged image with the time-strip method into the developed CNN model.

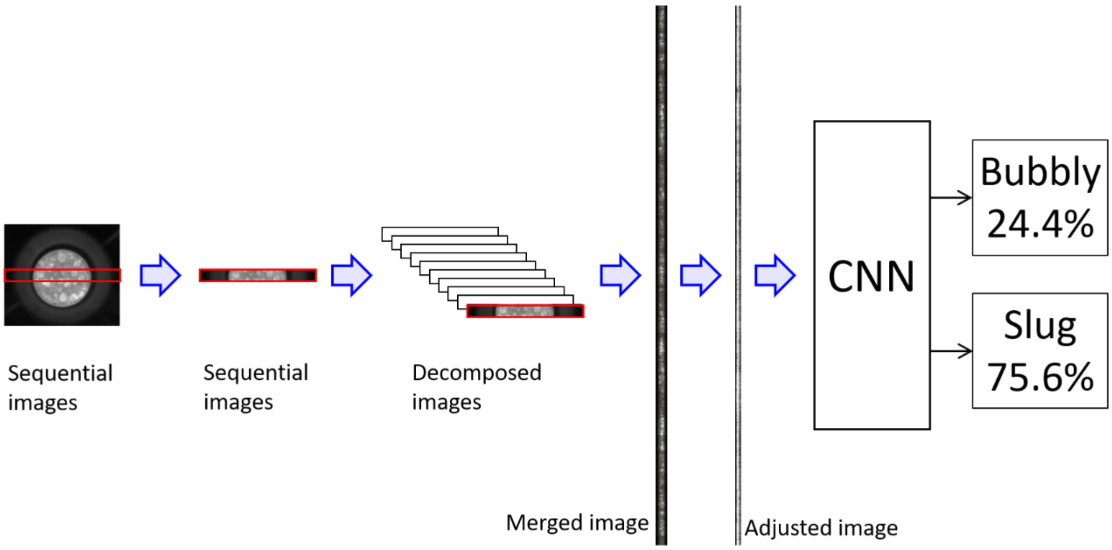

Fig. 3.2. Flow regime identification scheme of current method. The sequential image of the flow regime is merged into a single image before entering to the CNN.

3.2.1 Image pre-processing and CNN training

Fig. 3.3 illustrates the procedure of creating a merged image from the sequential images using the time-strip method. As can be seen, the central regions of sequential images recorded at 2,000 fps with resolutions of 640 x 480 and 1,280 x 1,080 pixels were extracted with the selection of 640 x 6 and 1,280 x 12 pixels, respectively. They were subsequently decomposed into 2,000 images. Then, the extracted images were arranged vertically from top to bottom with respect to time and integrated into single images of 640 × 12,000 and 1,280 × 26,000 pixels, respectively. For converting the image time frame to actual flow velocity, assuming that the flow regime with a total flow velocity of 1.0 m/s is recorded at 2,000 fps, the two-phase flow in the image rises at 0.5 mm/frame. Since the actual length of 6 or 12 pixels in the image corresponds to 0.43 mm, the resulting image has little overlap when the central region of each frame is extracted and combined.

In order to train the CNN with this obtained image, the image is converted into 40 × 4,000 pixels in consideration of the vertical resolution, which is the time-series information of the sequential image. In this process, the image resolution is reduced by the Lanczos filter, in which the input values of the nearby pixels of interest are multiplied with the values weighted by the filter.

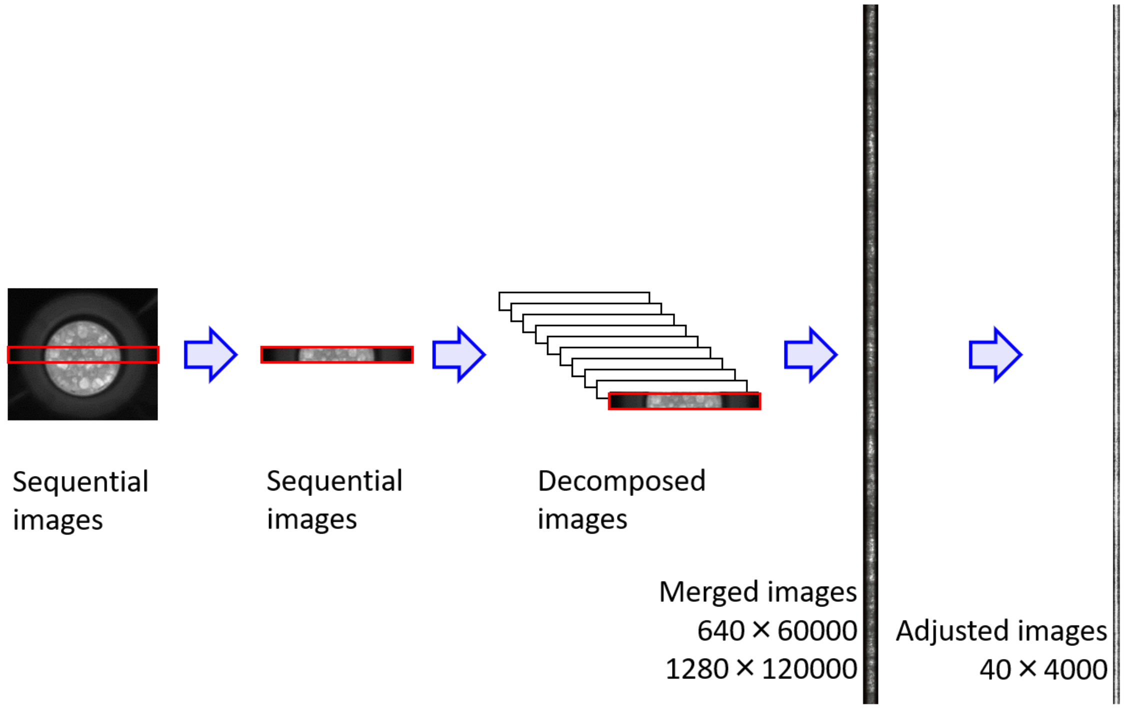

Fig. 3.3. Scheme of image merger with time strip method. Sequential images were extracted with the specific selection and dicomposed before merged to single image.

The CNN model used in this study is shown in Fig. 3.4. The network consists of two convolutional and two neural networks (NN) layers, and each layer consists of 64, 64 feature maps and 384, 192 nodes, respectively. The size of the image after processing each layer are shown in Table 3.1.

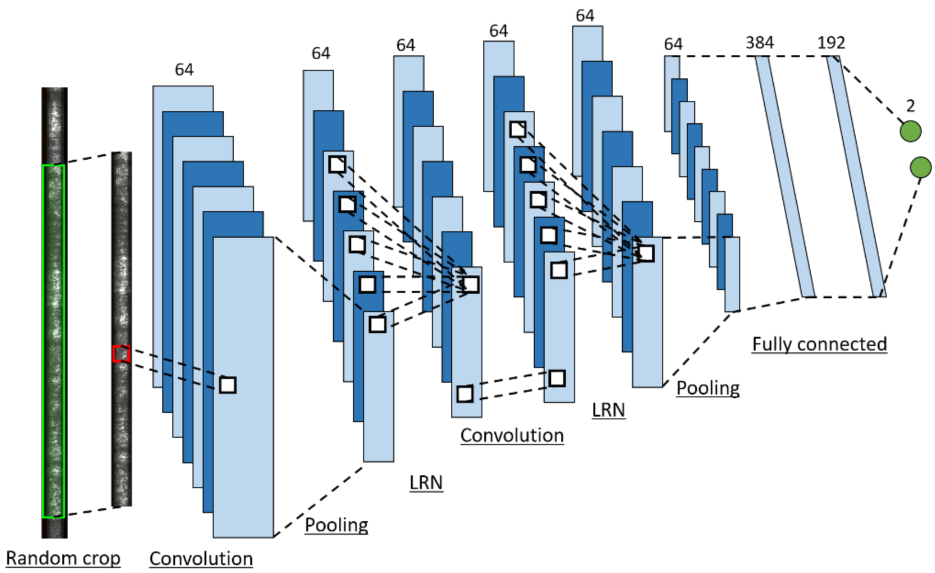

Fig. 3.4. Architecture of the CNN used in the current method, which consists of two convolutional and two neural networks layers.

Table 3.1. Image size after each layer.

Layer	Output size
Convolutions	30×3000
Pooling	15×1500
Local Response Normalization	15×1500
Convolutions	15×1500
Local Response Normalization	15×1500
Pooling	8×750

In order to improve the CNN model performance, an image area of 30 × 3,000 pixels was randomly extracted from the input image and utilized to train the model. The current CNN, referring to Krizhevsky (2009, 2014), introduces Local Response Normalization (LRN) (Krizhevsky et al., 2017), which is effective for static images, such as generated by the present preprocessing, and considers for deep scalability in the future. The number of nodes in the output layer was set to the number of classes. Here, the current method fine-tunes the CNN model by optimizing the model with given input image datasets. Thus, unlike conventional machine learning, where users must select and specify features, the present model enables one to identify the flow regime more objectively. Furthermore, to assess the optimal image length required for the CNN model for identification purposes, the $30 \times L$ (L = 100-3,000) central region of the input image was extracted to train the model, and the model outputs were evaluated (Fig. 3.5). In this evaluation, the training and model evaluation is done by dividing into a small diagram in which the L is set for each batch.

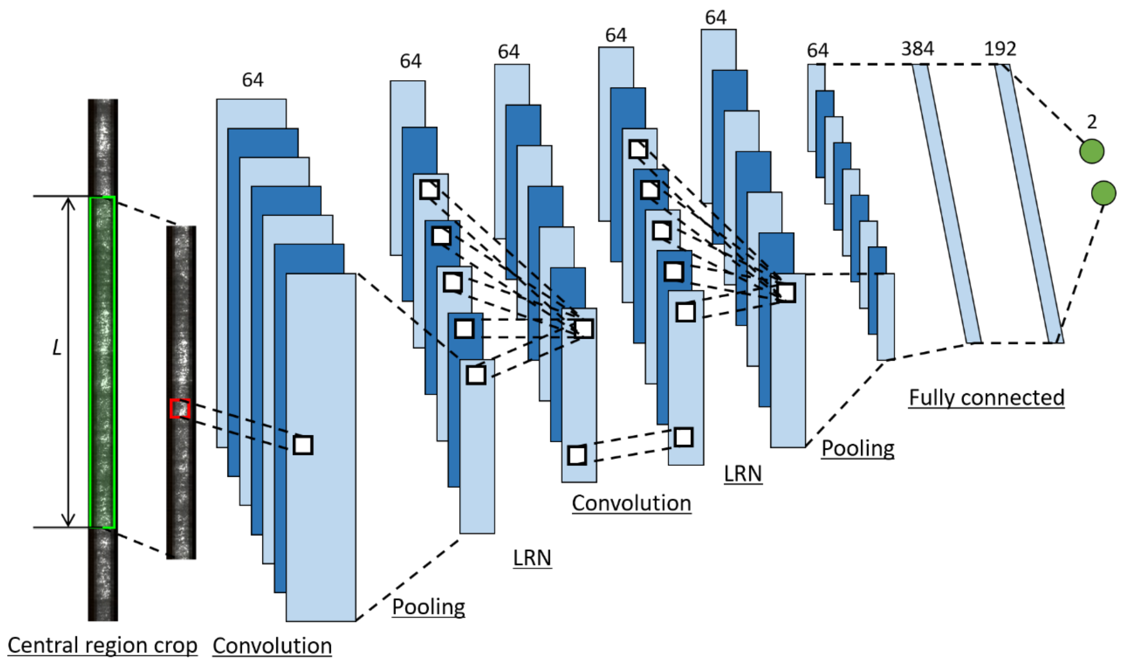

Fig. 3.5. The scheme of current method using the central region of the input image to assess the optimal image length.

3.2.2 Flow regime identification scheme

In this section, the scheme of identifying test images using the CNN model will be explained. The merged image with the time-strip method was utilized and adjusted for the input, similar to the training image. The image's central region, $30 \times L$ (L = 100-3,000) pixels, was extracted for the input data. The accuracy of the identification results can be calculated based on the class labels, namely bubbly and slug flow regimes. The accuracy of the CNN's class output for each output layer was calculated, and the class with the highest precision was selected as the final identification result for the given image.

3.3 Results and Discussion

3.3.1 Training condition

In order to assess the effectiveness of the present flow regime identification method, its capability was evaluated using the sequential images obtained from the experiment. First, the CNN model was newly developed with the output layer node of two to distinguish bubbly and slug flow regimes. The resolution of the images was selected as 40 × 4,000 pixels, and the number of images utilized for the training and validation was 125 (bubbly) and 127 (slug), respectively. The experimental conditions for each flow regimes and the transition criteria are shown in Fig. 3.6.

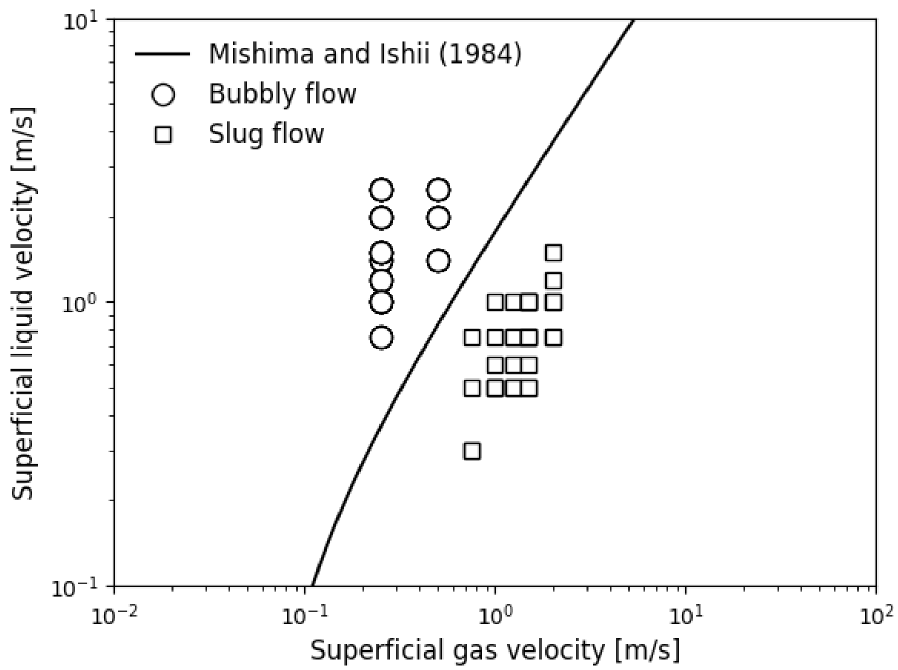

Fig. 3.6. Experimental conditions of bubbly and slug flow's training images shown in the flow regime map.

In this chapter, Mishima-Ishii's flow regime transition criteria (Mishima and Ishii, 1984) has been selected and the details are same as section 2.4.2. The training data are the images that are clearly identified as bubbly or slug flows by visual identification and also that are far from the transition boundaries of the transition criteria. In this study, the image datasets include both developing and fully-developed flow conditions and high-pressure conditions to establish the CNN model with sufficient generalization.

The training conditions are shown in Table 3.2. The batch storing 64 images was used in the training process, and the stochastic gradient descent method was used for the optimization scheme. The calculation was performed on an NVidia graphic board (GeForce RTX 2080) using TensorFlow installed on a Linux environment.

Table 3.2. Learning condition.

Image size	40×4,000 [pixel]
Learning rate	0.1
Learning rate scheduler	×0.1/ 350 [epoch]
Batch size	64
Epoch	3,060

An example of image utilization during the training process is shown in Fig. 3.7 (a). In the sequential image of bubbly flow, bubbles continuously pass through the visualization port (Fig. 3.7 (b)), and even after it is integrated into a single merged image, the bubble's dispersity is continuously captured in the image. Likewise, the cap bubbles can be seen in the image similar to the sequential image of slug flow where Taylor bubbles and liquid slug alternately passing through the visualization port (Fig. 3.7 (b)). Consequently, the flow regime can be visually identified even with the single image obtained from the time-strip method. The intermittent features such as Taylor bubbles of slug flow can also be captured in a single image. The studies by Borhani et al. (2010), Goda et al. (2019), and Kazi et al. (2021) have also shown that the interface structure can be captured by applying the time-strip method to the upward gas-liquid two-phase flow.

(a)

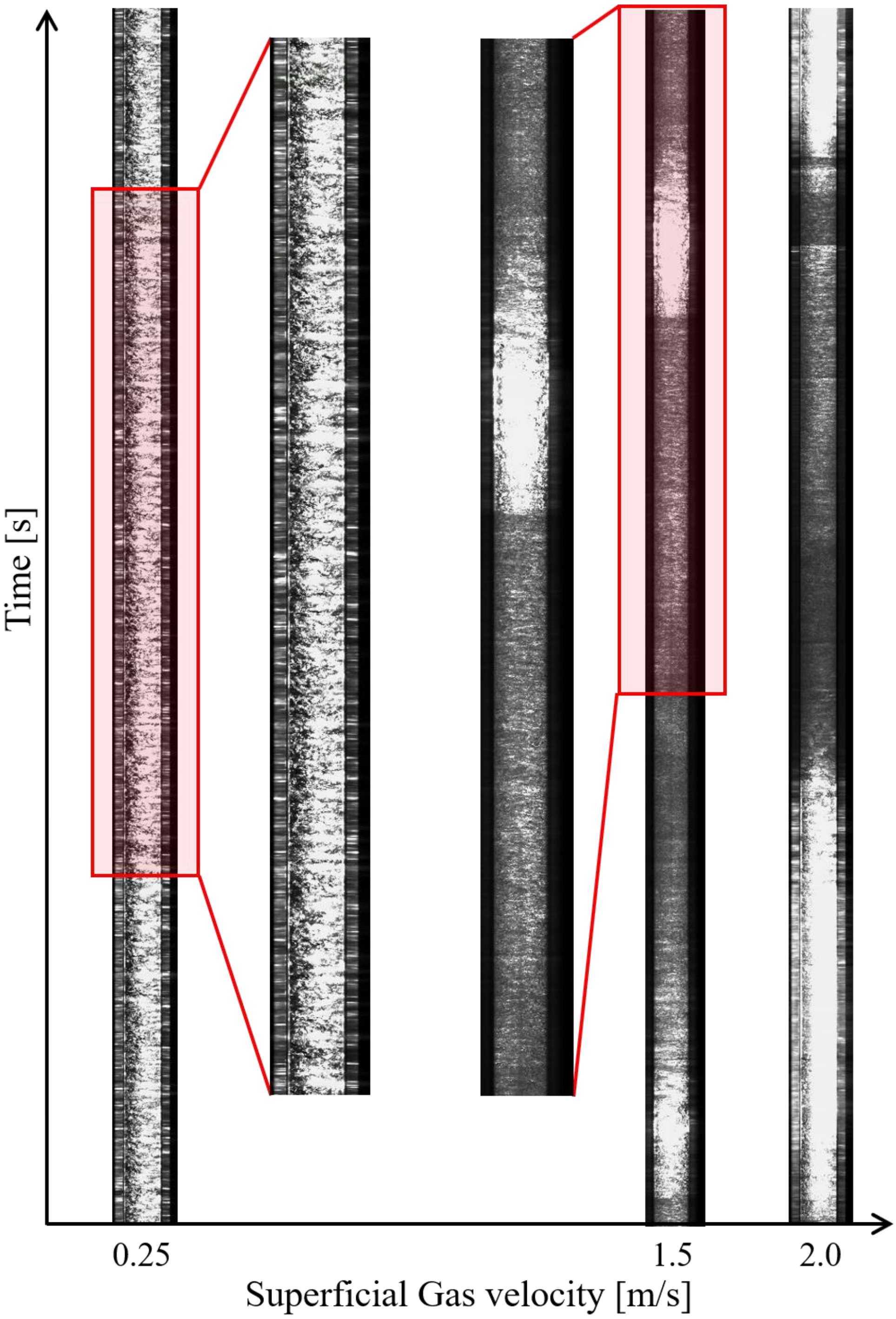

(b)

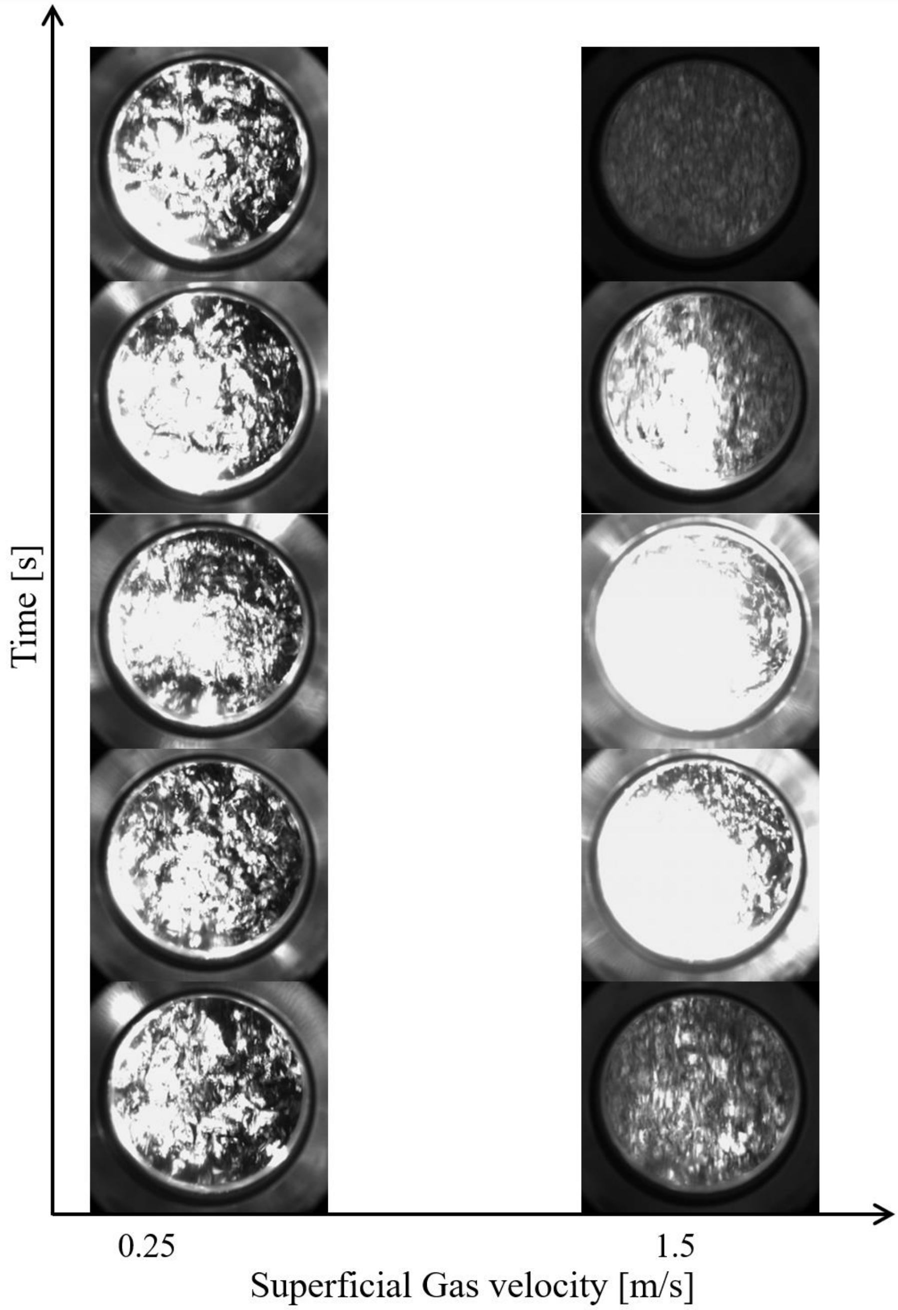

Fig. 3.7. (a) Training image of bubbly (superficial gas velocity of 0.25 m/s) and slug (superficial gas velocity of 1.5 and 2.0 m/s) flow for the CNN at the pressure of 2.8 MPaG and superficial liquid velocity of 1.0 m/s, (b) Orginal sequential image of bubbly and slug flow.

Fig. 3.8 shows the training results of the present CNN model. In this process, the cross-entropy error was selected as the loss function, and 3,060 epochs were performed. The precision with the images of batches was calculated at every 256 epoch. The learning rate was calculated with a decrease in 0.1 at every 350 epoch during the training process. As shown in Fig. 3.8, the loss function flattens out to less than three after 3,000 epochs, and the precision value fluctuates at 0.5 until it rises around 1,500 epochs to reach 97 %. The CNN model obtained by this training process was utilized to identify the flow regime hereafter.

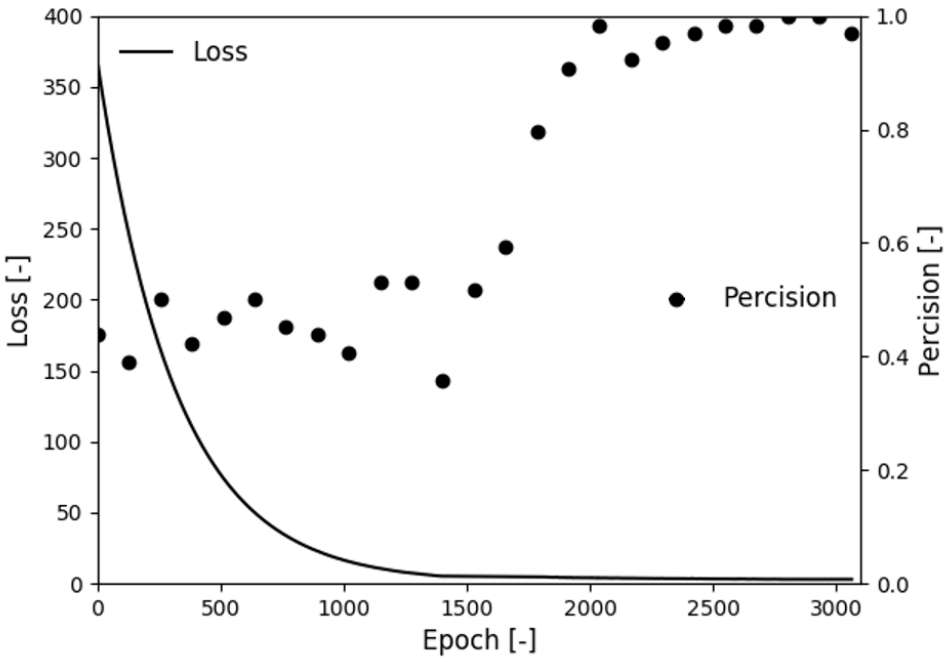

Fig. 3.8. The loss and the precision of batches image as function of ecpoch for CNN training process. The precision was calculated at every 256 epoch.

3.3.2 Test of the model

Evaluated results of the current method are tabulated in Table 3.3. The independent sequential image dataset was utilized for the evaluation, which was not part of the training data. The number of testing sequential images for bubbly and slug flow regimes were 37 each. The flow regimes of these images with different pressure conditions and elevation were first identified visually. The current method outputs the flow regime with high precision among bubbly flow and slug flow for the input image, and the time required for identification was about 30 seconds. As shown in Table 3.3, the flow regime of each sequential images was correctly identified as 91.9 % and 86.5 %, respectively. Therefore, the flow regime of gas-liquid two-phase flow can be identified with the present CNN model using the reconstructed images using the time-strip method. The reason why the precision of slug flow is lower than that of bubbly flow is that the CNN model may have learned the uniform bubbles of bubbly flow, while is not sufficiently learning the intermittency of slug flow.

Table 3.3. Test results of identifying method.

Flow Regime	Precision
Bubbly	91.9 %
Slug	86.5 %

3.3.3 Identification rate of image length

The optimal vertical length of the flow image required for the CNN model for flow regime identification was also investigated in the present study. Fig. 3.9 shows the identification results obtained from the CNN models that were trained with different image lengths.

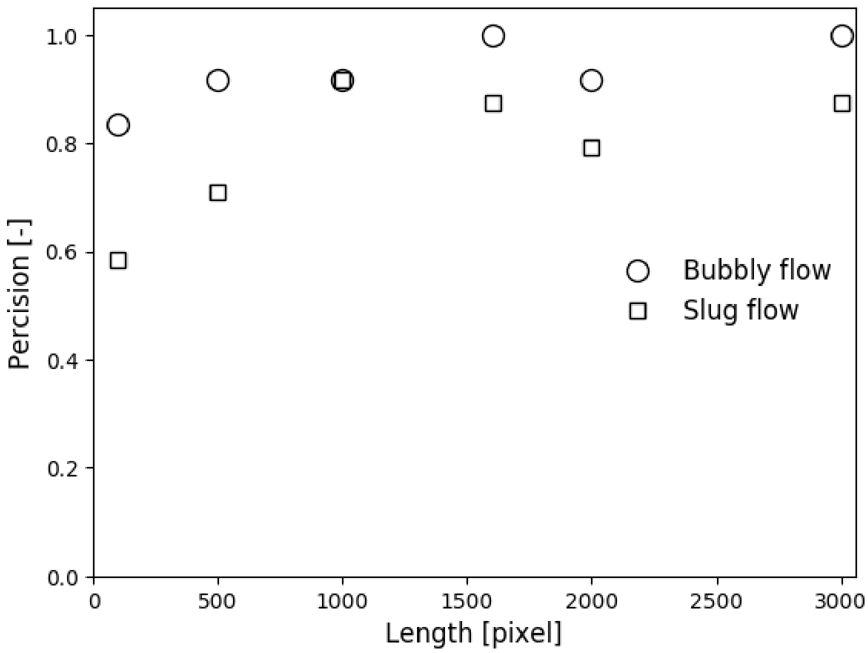

Fig. 3.9. Identification rate of bubbly and slug flow using CNN models trained with different input image lengths.

The identification rate e.g. precision is calculated as $P_i = n_i/N$ where, i is the flow regime of the input image, n_i is the correct number of images predicted by the CNN, and N is the total number of images fed to the CNN model. As shown in Fig. 3.9, the identification rate of bubbly flow and slug flow improves as the length of the image increases and becomes almost constant at a length of 1,600 pixels or beyond. Furthermore, the identification rate of slug flow is lower than that of bubbly flow regardless of the image length. The reason for the identification rate reaching constant beyond 1,600 pixels is that the length is sufficiently long enough to contain entire slug-unit comprised of Taylor bubble and liquid slug. Thus, features needed to identify the slug flow regime is contained in the image, once it exceeds 1,600 pixels in the present case. Since the bubbly flow image has uniform bubbles in any region, the image length is not an influential facor as was the case for the slug flow regime. For slug flow regime, to obtain a high identification rate using images, it is necessary to prepare images that are long enough to include entire slug flow features in the training process. Therefore, if the length of extracted image in the training process is shorter than these lengths, the CNN model shows a lower identification rate due to the insufficient information of slug unit. Thus, the identification rate of slug flow becomes lower than that of bubbly flow due to such limitation.

3.3.4 Measurement of the Taylor bubble length

The length of Taylor bubble in slug flow under high pressure was calculated using existing correlations to compare it with the identification rate of the extracted image length in the training process. The length of Taylor bubbles extracted from the images are summarized in Fig. 3.10.

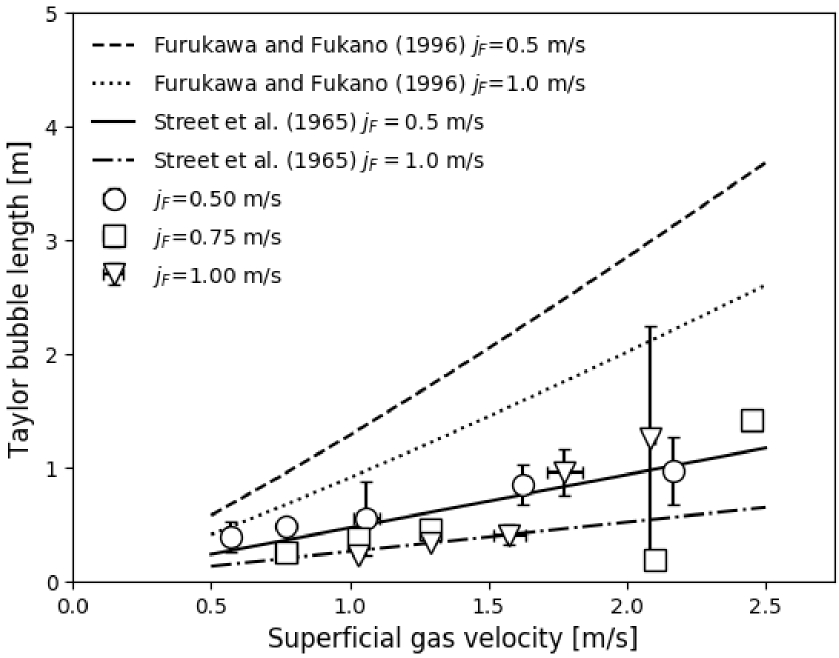

Fig. 3.10. Comparison between the measured length of Taylor bubbles and the calculated results from the model of Street et al. and Furukawa et al. at the fixed superficial liquid velocity.

The calculated slug lengths using correlations proposed by Street et al. (1965) and Furukawa and Fukano (1996) are shown for the comparison.

The length of Taylor bubble $\bar{l}_g$ was calculated by measuring the Taylor bubble passage time t_g from the high-speed image and multiplying the time with the bubble rise velocity u_g obtained from the drift flux model, i.e. $\bar{l}_g = u_g t_g$. The following figure averages the results for equivalent superficial gas-liquid velocities, and shows the standard deviation of Taylor bubble length and superficial gas velocity as error bar. The drift flux model for calculating the bubble rise velocity in slug flow regime is shown as (Zuber andFindlay, 1965; Ishii, 1977),

$$u_g = C_0\left(j_g + j_f\right) + v_{gj} \tag{1}$$

$$C_0 = 1.2 - 0.2\sqrt{\rho_g/\rho_f} \tag{2}$$

$$v_{gj} = 0.35\sqrt{\frac{Dg\left(\rho_f - \rho_g\right)}{\rho_g}} \tag{3}$$

The physical properties of fluids were set regarding the experimental pressure condition and the superficial gas and liquid velocity of recording condition were used. The Taylor bubble length correlations proposed by Street et al. (1965) and Furukawa and Fukano (1996) are expressed as follows.

$$\bar{l}_{g,Street} = \frac{0.29 j_g}{j_g + 0.12} \tag{3-1}$$

$$\bar{l}_{g,Furukawa} = 1.78 Re_f^{0.195} Fr_g^{1.15} Fr_f^{-0.695} D \tag{3-2}$$

Where $Re_f = j_f D/\upsilon$ is Reynolds number of fluids, $Fr_g = j_g/\sqrt{Dg}$ and $Fr_f = j_f/\sqrt{Dg}$ are Froude numbers of gas and liquid phase, respectively. The calculation results of superficial liquid velocity of 0.5 and 1.0 m/s are shown here. The experimental conditions of Street et al. (1965) and Furukawa and Fukano (1996) are shown in the Table 3.4, where the results are obtained under relatively low pressure conditions.

Table 3.4. The experimental conditions of Street et al., Furukawa and Fukano

Authors	Pipe Diameter [mm]	Pressure [MPaG]	Superficial liquid velocity [m/s]	Superficial gas velocity [m/s]
Street et al.	28.6	0.07	0 – 0.65	0.05 – 0.90
Furukawa and Fukano	19.2	0.15	0.1 - 0.5	0.3 – 1.0

As presented in Fig. 3.10, in every superficial liquid velocity, the Taylor bubbles become longer as the superficial gas velocity increases. On the other hand, the length of Taylor bubbles at constant superficial gas velocity condition decreases as the superficial liquid velocity increases. By comparing the experimental results with existing correlations, the results from Street et al. (1965) showed reasonable agreement in the range of 0.5 m/s to 1.0 m/s of superficial liquid velocity and up to 1.58 m/s of superficial gas velocity for the present study. The length of Taylor bubbles for superficial gas velocity over 1.6 m/s tends to fluctuate greatly due to the unsteady nature of the slug flow regime. From this analysis, it can be concluded that the model derived from the results of low-pressure experiment can be applied to the high-pressure condition in certain flow conditions.

The calculation results of slug unit length $\bar{l}_u$, which is comprised of Taylor bubble and liquid slug, is shown in Fig. 3.11.

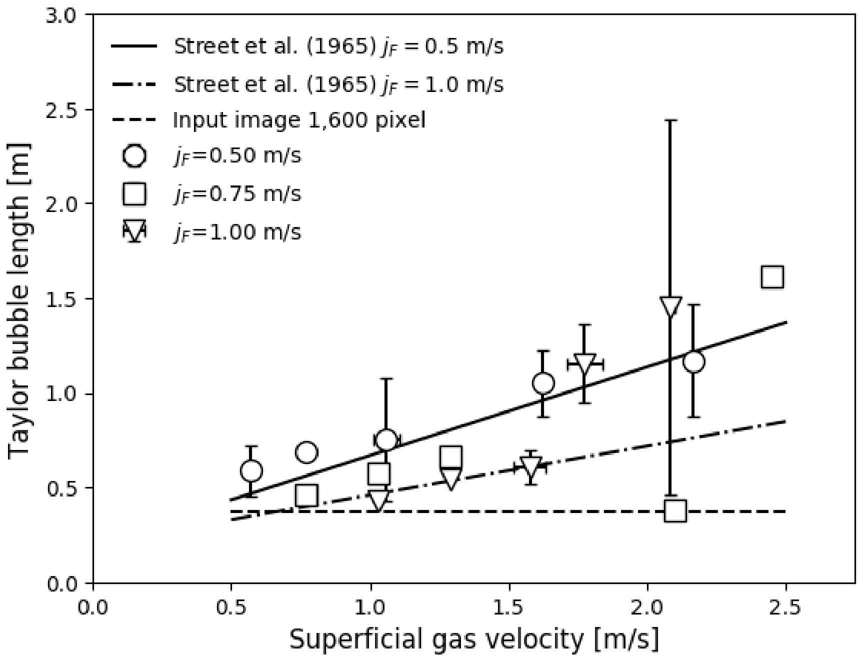

Fig. 3.11. Comparison between the measured length of slug units and the calculated length of input image for stable identification rate of current method.

In the study of Akagawa and Sakaguchi (1966), the length of liquid slug $\bar{l}_f$ was assumed to be constant at 0.2 m regardless to the superficial gas velocity. Therefore, the length of slug unit $\bar{l}_u$ is calculated by adding the constant length value of liquid slug $\bar{l}_f$ to the Taylor bubble length $\bar{l}_g$ i.e. $\bar{l}_u = \bar{l}_g + \bar{l}_f$. In Fig. 3.11, the 1,600 pixel length of input image, where the precision became stable by the flow regime identification method, is shown. Since the unit length of the input image is 0.23 mm/ pixel, the image length in millimeter can be obtained by multiplying the pixel length of the image by the unit length. Fig. 3.11 indicates that the length of slug unit varies from 0.37 m to 2.00 m, while the input image length was kept at 0.35 m. Therefore, the present method shows a reasonable performance in slug flow regime identification by utilizing the image length longer than the minimum length of slug unit.

3.3.5 Transition from bubbly to slug flow regime

In general, both bubbly and slug flows possess unique and distinctive gas-liquid interfacial structures. However, the transition from bubbly to slug flow regime does not occur instantaneously, but rather goes through gradual transition process under coalescence and disintegration of gas-liquid interface. Thus, in this section, bubbly-slug transition with respect to change in superficial velocities is quantitatively assessed using the developed model.

The identification results from the sequential images obtained at 2.8 MPaG and 25.3 m elevation at fixed superficial gas and liquid velocity conditions are summarized in Fig. 3.12. and Fig. 3.13. . The superficial liquid and gas velocities are fixed at 0.5-2.0 m/s and 0.3-2.0 m/s respectively, and the precision of identification results for bubbly and slug flow from the sequential image is plotted. As shown in Fig. 3.12, when the superficial liquid velocity is fixed, the precision of bubbly flow identification is higher at lower superficial gas velocity, and that of slug flow is higher at larger superficial gas velocity for all conditions.

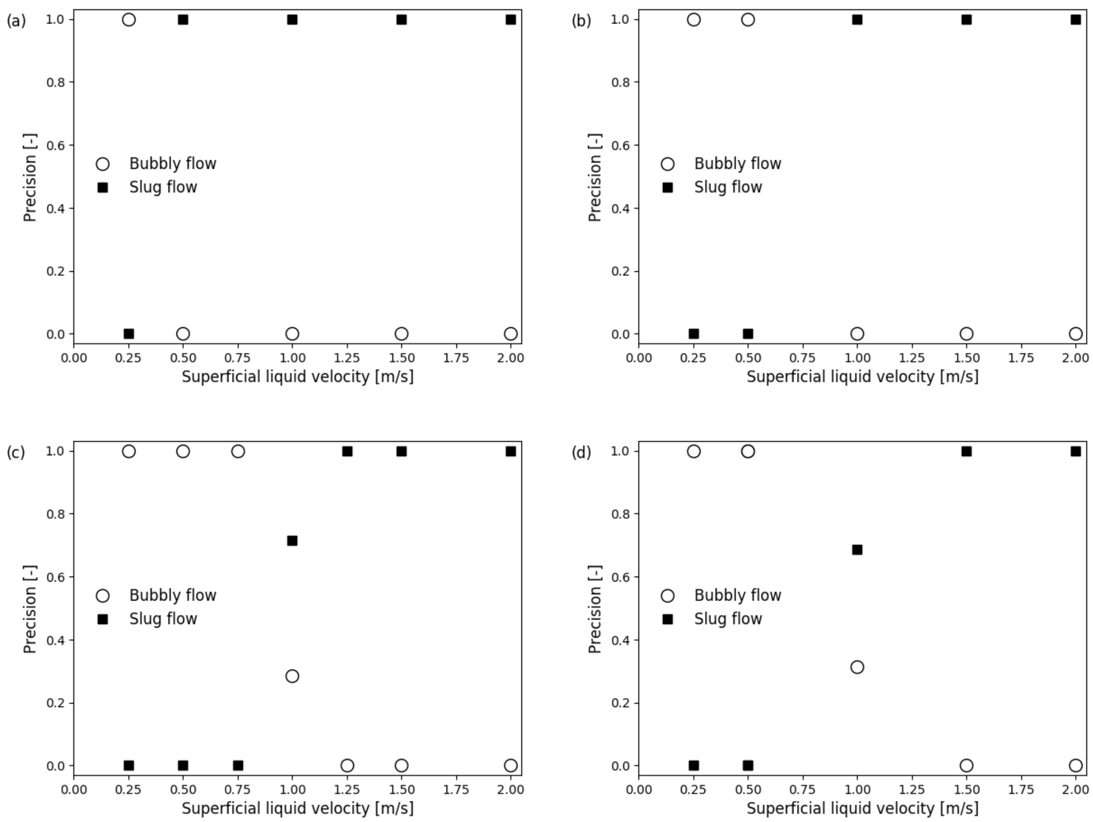

Fig. 3.12. Identified results of transition state using the current method, where the superficial liquid velocity are fixed at(a) 0.5 m/s, (b) 1.0 m/s, (c) 1.4 m/s and (d) 2.0 m/s.

The superficial gas velocity value for the flow regime transition tends to differ at a given superficial liquid velocity condition, as can be also confirmed from the existing flow regime maps. As tabulated in Table 3.5, the superficial gas velocity at flow regime transition tends to increase as the superficial liquid velocity increases.

Table 3.5. Flow regime transition flow rates evaluated from the CNN model

Superficial liquid velocity [m/s]	Superficial gas velocity [m/s]
0.5	0.75
1.0	1.0
1.4	1.25
2.0	1.5

In addition, Fig. 3.12 shows that the flow regime has shifted from bubbly to slug flow instantly at the tabulated superficial gas velocity under the conditions for j_f= 0.5 m/s and 1.0 m/s. Conversely, at the j_f= 1.4 m/s and 2.0 m/s, the precision of bubbly flow and slug flow is less than 90% at j_g = 1.0 m/s, and the precision of slug flow reaches 90% and above thereafter. If the precision for both bubbly and slug flow less than 90% is defined as the transition state, the transition region from bubbly to slug flow can be considered somewhere between $j_{g,b\text{-}s}$ = 0.75-1.25 m/s for $j_{f,b\text{-}s}$ =1.4 m/s, and between $j_{g,b\text{-}s}$ =0.5-1.5 m/s of that for the $j_{f,b\text{-}s}$ = 2.0 m/s. Thus, the results show that the bubbly-slug flow transition region ranges around $j_{b\text{-}s}$ = 0.5-1.0 m/s, from the transition criteria.

As shown in Fig. 3.13, when j_g is fixed at 0.25 m/s, all the test conditions have a high precision for bubbly flow identification. For slug flow regime, however, high precision values are observed for the fixed j_g of 1.5 m/s and 2.0 m/s. In view of the superficial liquid velocity, j_f, the identification precision for slug flow tends to be high at lower j_f. The precision tends to be higher for bubbly flow at the j_f of 1.0 m/s or higher under j_g = 0.5 m/s. From these results, the transition state can be confirmed as j_g = 1.4 m/s for the j_f of 1.0 m/s. It seems to be that there is a region of about 0.5-1.0 m/s apparent transition region from bubbly to slug flow even under the fixed superficial gas velocity condition. Furthermore, the transition region under superficial gas velocity of 1.0 m/s is wider than the fixed j_f condition, thereby implying that the flow regime transits moderately when the j_f increases. In general, flow regime transition from slug to bubbly flow is mostly through disintegration of Taylor bubbles into fine bubbles. This is caused by the larger shear stress due to the higher turbulence intensity promoted by increased local liquid velocity. As shown in the results, the flow regime over 2.0 m/s of j_f can be considered as a trantision state because the liquid velocity was not sufficient for the flow regime to reach bubbly flow regime.

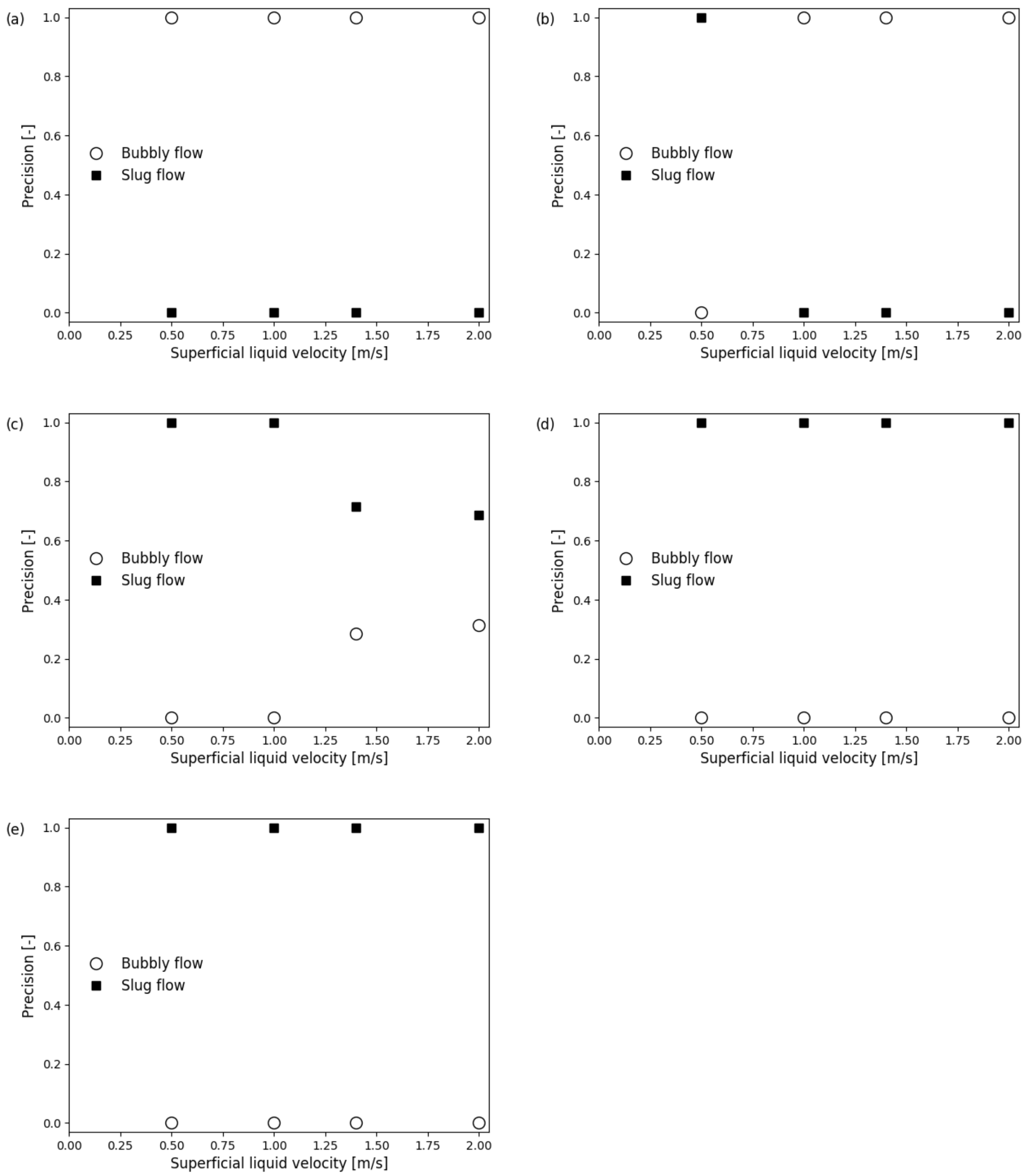

Fig. 3.13. Identified results of transition state using the current method, where the superficial gas velocity are fixed at (a) 0.25 m/s, (b) 0.5 m/s, (c) 1.0 m/s, (d) 1.5 m/s and (e) 2.0 m/s.

3.3.6 Comparison with existing model

The flow regime identification results from current methodology is compared with the Mishima-Ishii's flow regime transition criteria (Mishima and Ishii, 1984) which is mentioned above. The physical properties of fluids were selected according to the experimental pressure condition. The comparison of transition model and results of current method are shown in Fig. 3.14.

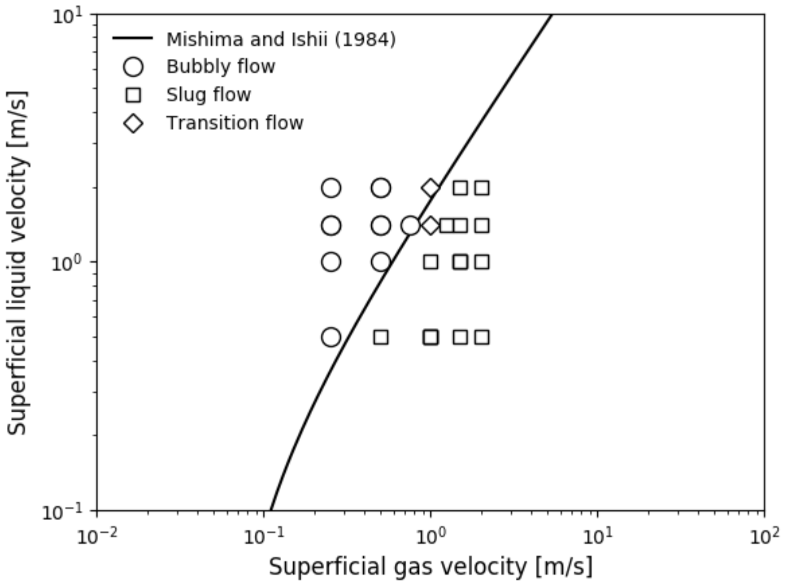

Fig. 3.14. Comparing the identified results from the current method with Mishima-Ishi's flow regime transition criteria by the flow regime map for 2.8 MPaG pressure and 25.3 m elevation.

Legends of current method are labeled as bubbly or slug flow for the results with identification score exceeding 90%. The case is categorized as transition flow for the results with identification score ranging in between 10% to 90%. The Fig. 3.14 shows that flow regime of experimental data is transiting at the superficial velocity of Mishima-Ishii criteria, and the results of current methods and transition model are in good correlation. Furthermore, the flow regime of experimental condition for j_f = 1.4 m/s at 1.0 m/s of j_g, is in transition region, which is included in the region of superficial gas velocity ±0.2 m/s from the Mishima-Ishii criteria. As is shown in the result from the current method, the bubbly flow transit to slug flow at the boundary of transition criteria, which means that the critical superficial gas velocity is larger than that of Mishima-Ishii. Given that Mishima-Ishii uses critical void fraction of 0.3 derived from the tight packing of rigid spheres, the results indicate that the transiting gas void fraction for bubbly-slug flow is possibly larger for the present high-pressure system.

3.4 Conclusions

In this study, a novel the flow regime identification method using the CNN model trained by a single merged image obtained from the time-stripping was proposed. This study is the rare case in which deep learning, highly capable of identifying static images, was applied to processed images, capturing the dynamics of gas-liquid two-phase flow seen in the sequential images. The model is applicable for bubbly-slug transition at high-pressure two-phase flow conditions (0.3-2.8 MPaG) for the j_f = 0.5-2.5 m/s and j_g =0.25-2.0 m/s, at the elevation ranging from 0.6-25.3 m. The identification capability between bubbly flow and slug flow for the current method was investigated. Furthermore, using the presently developed model, quantifiable flow regime transition range was investigated using the identification precision values obtained from the present model. The results were compared with existing flow regime transition criteria proposed by Mishima-Ishii. Based on the results, the following conclusions were drawn:

1. By comparing the measured Taylor bubble length obtained under high pressure experiment with the existing model developed at low pressure conditions, the correlation proposed by Street et al. showed reasonable predictive capability.
2. In the current method, the identification rate became constant at the image length of 1600 pixels, which corresponds to 0.37 m in actual length. Since the minimum length of the measured slug unit was about the same, hence, it can be concluded that the identification performance for slug flow highly depends on the image length. For the selection of image length, it is recommended to check expected slug unit length in the given system.
3. The identification results in the transition region have quantitatively shown that the transition region exists for the bubbly to slug flow. It was found that the bubbly-slug transition region under fixed superficial gas velocity is wider than the fixed superficial liquid velocity condition. This imply that the flow regime transition occurs moderately at the larger superficial liquid velocity.

The identification results of the current method and Mishima-Ishii's flow regime transition criteria were in good agreement, in general. However, some cases showed larger j_g at flow regime transition region compared to Mishima-Ishii equation. This indicates that the critical void fraction for bubbly-slug transition is larger than the theoretical value of 0.3 for some cases.

Bibliography

Akagawa, K., Sakaguchi, T., 1966. Fluctuation of Void Ratio in Two-Phase Flow : 2nd Report, Analysis of Flow Configuration Considering the Existence of Small Bubbles in Liquid Slugs. Bulletin of JSME 9, 104–110.

Besagni, G., Inzoli, F., 2017. The effect of electrolyte concentration on counter-current gas–liquid bubble column fluid dynamics: Gas holdup, flow regime transition and bubble size distributions. Chemical Engineering Research and Design 118, 170–193.

Borhani, N., Agostini, B., Thome, J.R., 2010. A novel time strip flow visualisation technique for investigation of intermittent dewetting and dryout in elongated bubble flow in a microchannel evaporator. International Journal of Heat and Mass Transfer 53, 4809–4818.

Firouzi, M., Howes, T., Nguyen, A.V., 2015. A quantitative review of the transition salt concentration for inhibiting bubble coalescence. Advances in Colloid and Interface Science, Reinhard Miller, Honorary Issue 222, 305–318.

Fu, Y., Liu, Y., 2019. BubGAN: Bubble generative adversarial networks for synthesizing realistic bubbly flow images. Chemical Engineering Science 204, 35–47. https://doi.org/10.1016/j.ces.2019.04.004

Furukawa, T., Fukano, T., 1996. Effect of liquid viscosity on a large gas bubble velocity in a stagnant liquid and flow parameters in a gas liquid slug flow. Japanese Journal of Multiphase Flow 10, 154–170.

Goda, R., Hayashi, K., Murase, M., Hosokawa, S., Tomiyama, A., 2019. Experimental study on interfacial and wall friction factors under counter-current flow limitation in vertical pipes with sharp-edged lower ends. Nuclear Engineering and Design 353, 110223.

Haas, T., Schubert, C., Eickhoff, M., Pfeifer, H., 2020. BubCNN: Bubble detection using Faster RCNN and shape regression network. Chemical Engineering Science 216, 115467. https://doi.org/10.1016/j.ces.2019.115467

Ishii, M., 1977. One-dimensional drift-flux model and constitutive equations for relative motion between phases in various two-phase flow regimes. ANL 77, 67.

Kazi, J., Mori, H., Fukuma, J., Hayashi, K., Kurimoto, R., Tomiyama, A., 2021. Flow Characteristics of Air-Water Two-Phase Flows in a Serpentine Tube. Japanese Journal of Multiphase Flow 35, 85–92.

Krizhevsky, A., 2009. Learning Multiple Layers of Features from Tiny Images (Master’s thesis). University of Tront.

Krizhevsky, A., 2014. One weird trick for parallelizing convolutional neural networks. arXiv:1404.5997 [cs].

Krizhevsky, A., Sutskever, I., Hinton, G.E., 2017. ImageNet classification with deep convolutional neural networks. Commun. ACM 60, 84–90. https://doi.org/10.1145/3065386

Li, H., Sun, B., Guo, Y., Gao, Y., Zhao, X., 2018. Recognition and measurement gas-liquid two-phase flow in a vertical concentric annulus at high pressures. Heat Mass Transfer 54, 353–362.

Mandalahalli, M.M., Wagner, E.C., Portela, L.M., Mudde, R.F., 2020. Electrolyte effects on recirculating dense bubbly flow: An experimental study using X-ray imaging. AIChE Journal 66, e16696. https://doi.org/10.1002/aic.16696

Mishima, K., Ishii, M., 1984. Flow regime transition criteria for upward two-phase flow in vertical tubes. International Journal of Heat and Mass Transfer 27, 723–737.

Ming-Kuei Hu, 1962. Visual pattern recognition by moment invariants. IRE Transactions on Information Theory 8, 179–187.

Nguyen, P.T., Hampton, M.A., Nguyen, A.V., Birkett, G.R., 2012. The influence of gas velocity, salt type and concentration on transition concentration for bubble coalescence inhibition and gas holdup. Chemical Engineering Research and Design 90, 33–39. https://doi.org/10.1016/j.cherd.2011.08.015

Omebere-Iyari, N.K., Azzopardi, B.J., Ladam, Y., 2007. Two-phase flow patterns in large diameter vertical pipes at high pressures. AIChE Journal 53, 2493–2504.

Pan, L., Zhang, M., Ju, P., He, H., Ishii, M., 2016. Vertical co-current two-phase flow regime identification using fuzzy C-means clustering algorithm and ReliefF attribute weighting technique. International Journal of Heat and Mass Transfer 95, 393–404.

Pawlak, Z., 1982. Rough sets. International Journal of Computer and Information Sciences 11, 341–356.

Poletaev, I., Tokarev, M.P., Pervunin, K.S., 2020. Bubble patterns recognition using neural networks: Application to the analysis of a two-phase bubbly jet. International Journal of Multiphase Flow 126, 103194. https://doi.org/10.1016/j.ijmultiphaseflow.2019.103194

Quinn, J.J., Kracht, W., Gomez, C.O., Gagnon, C., Finch, J.A., 2007. Comparing the effect of salts and frother (MIBC) on gas dispersion and froth properties. Minerals Engineering 20, 1296–1302. https://doi.org/10.1016/j.mineng.2007.07.007

Sánchez Mirón, A., García Camacho, F., Contreras Gómez, A., Grima, E.M., Chisti, Y., 2000. Bubble-column and airlift photobioreactors for algal culture. AIChE Journal 46, 1872–1887. https://doi.org/10.1002/aic.690460915

Sasaki, T., Miwa, S., Sawa, K., 2019. Study of two phase flow regime identification using image recognition. Presented at the Multi-phase flow symposium 2019.

Shi, L., 2007. Fuzzy Recognition for Gas-liquid Two-phase Flow Pattern Based on Image Processing, in: 2007 IEEE International Conference on Control and Automation. Presented at the 2007 IEEE International Conference on Control and Automation, 1424–1427.

Shanthi, C., Pappa, N., 2017. An artificial intelligence based improved classification of two-phase flow patterns with feature extracted from acquired images. ISA Transactions 68, 425–432.

Shibata, N., Miwa, S., Sawa, K., Takahashi, M., Murayama, T., Tenma, N., 2021. Identification of Upward Two-Phase Flow Regime Transition Region under High-Pressure Condition Using Deep Learning. Japanese Journal of Multiphase Flow 35, 93–100.

Street, J.R., Tek, M.R., 1965. Unsteady state gas-liquid slug flow through vertical pipe. AIChE Journal 11, 601–607.

Torisaki, S., Miwa, S., 2020a. Robust bubble feature extraction in gas-liquid two-phase flow using object detection technique. Journal of Nuclear Science and Technology 57, 1231–1244.

Torisaki, S., Miwa, S., 2020b. Gas-Liquid Two-Phase Flow Image Analysis Using Bubble Detection Algorithm. Japanese Journal of Multiphase Flow 34, 125–133.

Wu, B., Firouzi, M., Mitchell, T., Rufford, T.E., Leonardi, C., Towler, B., 2017. A critical review of flow maps for gas-liquid flows in vertical pipes and annuli. Chemical Engineering Journal 326, 350–377.

Xiao, J., Luo, X., Feng, Z., Zhang, J., 2018. Using artificial intelligence to improve identification of nanofluid gas–liquid two-phase flow pattern in mini-channel. AIP Advances 8, 015123. https://doi.org/10.1063/1.5008907

Zhang, M., Pan, L., Ju, P., Yang, X., Ishii, M., 2017. The mechanism of bubbly to slug flow regime transition in air-water two phase flow: A new transition criterion. International Journal of Heat and Mass Transfer 108, 1579–1590. https://doi.org/10.1016/j.ijheatmasstransfer.2017.01.007

Zhang, Y., Azman, A.N., Xu, K.-W., Kang, C., Kim, H.-B., 2020. Two-phase flow regime identification based on the liquid-phase velocity information and machine learning. Exp Fluids 61, 212. https://doi.org/10.1007/s00348-020-03046-x

Zhou, Y., Chen, F., Sun, B., 2008. Identification Method of Gas-Liquid Two-phase Flow Regime Based on Image Multi-feature Fusion and Support Vector Machine. Chinese Journal of Chemical Engineering 16, 832–840.

Zuber, N., Findlay, J.A., 1965. Average Volumetric Concentration in Two-Phase Flow Systems. Journal of Heat Transfer 87, 453–468.

4 Objective flow regime identification with unsupervised learning

4.1 Introduction

In chapter 3, the method is proposed to identify flow regime by CNN trained with images derived from time strip method, and has quantified the transition region of flow regime. However, this method requires training the CNN with enough labeled images in advance, and some transition regions did not show quantitative results. Therefore, present chapter identifies flow regimes of high-pressure upward gas-liquid two-phase flow and quantifies the transition with classification by unsupervised learning, which does not require labeled images. In detail, merged images are derived using time strip method and classified using unsupervised learning such as principal component analysis (PCA) (Jolliffe, 2002), k-means method (MacQueen, 1967), and Gaussian mixture models (GMM) (Yu et al., 2010).

4.2 Methodology

4.2.1 Theory and calculation condition

The unsupervised learning methods used in this study are PCA, k-means method and GMM. PCA is a method for reducing the dimension of the input while preserving the feature of input values. In the present study, the method is used to diminish the resolution of image $i \in \{1, \ldots, l\}$ to lower dimension, which equation is as follows:

$$\boldsymbol{V}\boldsymbol{u_k} = \lambda_k \boldsymbol{u_k} \tag{4-1}$$

The obtained component $k \in \{1, \ldots, n\}$ of image i is unique feature of the image and the method calculates the component k and its contribution λ_k to maximize the features, which the resulting components can be interpreted as features of each image.

The k-means method classifies points distributed in multidimensional space into arbitrary number of clusters and the method is used to classify the feature of each image obtained from PCA in the present study, which equation is as follows:

$$E = \sum_{j=1}^{m} \sum_{x_i \in V_j} \left\| \boldsymbol{x}_i - \boldsymbol{W}_j \right\|^2 \tag{4-2}$$

This method classifies each image into clusters $j \in \{0, \ldots, m\text{-}1\}$ by minimizing the distance E between the distributed images and the center of each cluster. Since the result of PCA is the feature of each image, these can be classified by clustering with similar feature, which relates to flow regime.

GMM is the clustering method similar to k-means method, assuming that the points are distributed as gaussian distribution from the center of each cluster. Here the image features resulting from PCA are classified and the attribution probability to each cluster is obtained. The probability $P(\boldsymbol{j}|\boldsymbol{x_i})$ calculated by GMM that image i belongs to cluster j is as follows

$$P(\boldsymbol{j}|\boldsymbol{x_i}) = \frac{\varepsilon_j N(\boldsymbol{x_i}|\boldsymbol{\mu}_j, \boldsymbol{V}_j)}{\sum_{j=1}^{m} \varepsilon_j N(\boldsymbol{x_i}|\boldsymbol{\mu}_j, \boldsymbol{V}_j)} \tag{4-3}$$

$$N(\boldsymbol{x_i}|\boldsymbol{\mu}_j, \boldsymbol{V}_j) = \frac{1}{(2\pi)^{\frac{l}{2}}} \frac{1}{|\boldsymbol{V}_j|^{\frac{1}{2}}} \exp\left\{-\frac{1}{2}(\boldsymbol{x_i} - \boldsymbol{\mu}_j)^T \boldsymbol{V}_j^{-1}(\boldsymbol{x_i} - \boldsymbol{\mu}_j)\right\} \tag{4-4}$$

This method determines the cluster center point by calculating the maxima of the mixing coefficient ε_j, the mean column vector $\boldsymbol{\mu}_j$, and the variance-covariance matrix $\boldsymbol{V}_j$ using the expectation-maximization algorithm (hereafter EM method) (Dempster, 1977). GMM, as with k-means method, classifies each image by forming clusters based on images features obtained by PCA. In general, the k-means method has characteristic of classifying distributed points in multidimensional space into spheres with the center point of cluster, while the EM method can classify distributed points with complex shapes. (Kamishima, 2003).

In this study, the images merged by time strip method are reduced in size and are classified with k-means method or GMM after the image dimension is diminished by PCA. In detail, the image is reduced to 50 x 2550 pixel, 127500 pixel is diminished to n=300 components by PCA, and q=10 components out of 300 components are input to k-means method or GMM. For classification of flow regime, 149 and 151 images of bubbly and slug flow are used respectively, and 48 images are used as evaluation images including transition region. Note that the evaluation image includes 2.8 MPaG pressure and 25.3 m elevation. The calculation conditions for k-means method and GMM are shown in Table 4.1.

Table 4.1. Calculation conditions for k-means method and GMM.

	k-means method	GMM
Cluster number (m)	4	4
Input component number (q)	10	10
Maximum number of reallocating clusters	1000	1000
Convergence rate	0.0001	0.0001

4.2.2 Processed image

The image obtained from section 3.2.1 contains data other than flow regime, such as outer edge of observation port, and since the PCA method calculates all pixels of the image, the unnecessary areas are included in flow regime classification. In this study, the PCA is applied to original image and processed image with 30% reduction on both sides of the image to examine the effect of unnecessary regions (Fig. 4.1).

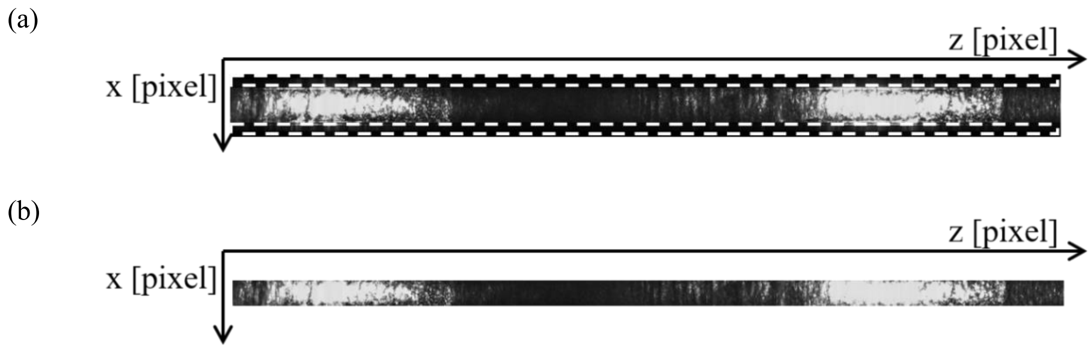

Fig. 4.1. Example of (a) original and (b) processed images. Unnecessary areas are indicated with dotted lines.

4.3 Results and Discussion

4.3.1 Results of PCA

The summation of features belonging to *k* component obtained by PCA with image data set are shown in Fig. 4.2, and the values are shown in Table 4.2. Here are the results of original and processed images. As shown in Fig. 4.2, the summation of features increases with the number of component k in both original and processed images. Also, Table 4.2 shows that the summation of features in processed image is average 0.024 larger than that of original image up to k=50 components, but is average 0.012 smaller for k=100 components or more. Therefore, classification with less components might improve using processed images.

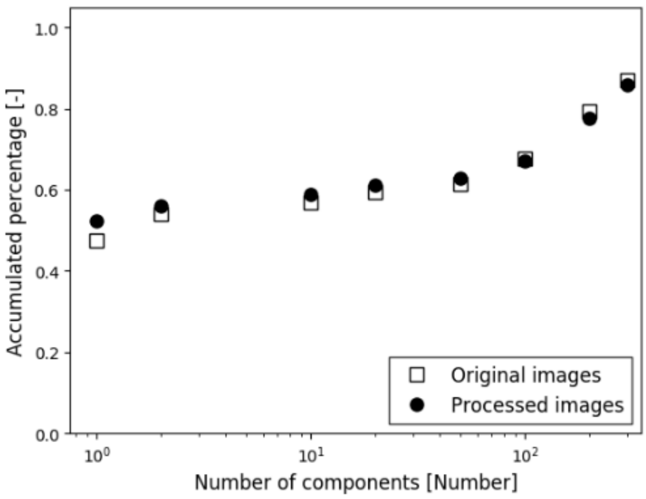

Fig. 4.2. Accumulated percentage of features for classification from PCA results of original and processed images.

Table 4.2. Accumulated percentage of features for original and processed images.

Number of components (k)	Original images	Processed images
1	0.475	0.523
2	0.540	0.559
10	0.568	0.590
20	0.594	0.610
50	0.613	0.628
100	0.677	0.672
200	0.792	0.775
300	0.869	0.857

Next, Fig. 4.3 shows the scatter plot with k=1 and 2 as axes among the components of each image obtained by PCA. Here are the results with processed images. The results show that 86.5% of bubbly flow are located in -1 to 2 for k=1 component and -1 to 1 for the k=2 component, and 84.1% of slug flow are in -2 to 1 for the k=1 component and -2 to 2 for the k=2 component thus, feature of different flow regime is clear with two components. Therefore, the images resolution is diminished to lower dimension by inputting the images into PCA, while retaining the image features for classification.

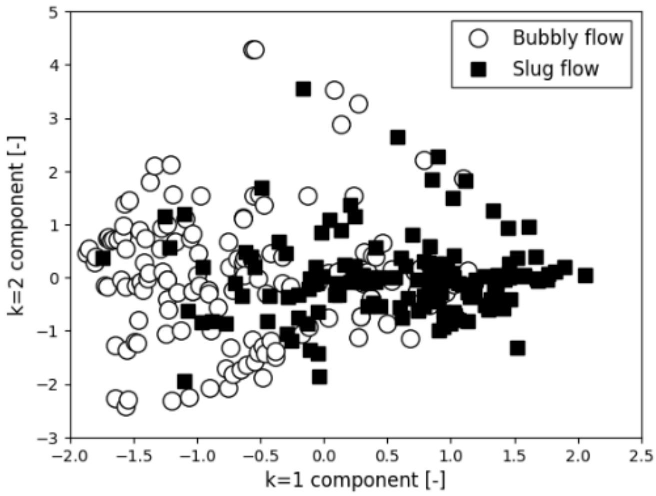

Fig. 4.3. Plots of k=1 and 2 components of PCA.

4.3.2 Results of k-means method

Fig. 4.4 shows the inertia of k-means method when number of clusters j is increased for the q=10 component of each image obtained by PCA. Inertia is the sum of within-cluster variance for all clusters, indicating higher classification with smaller values.

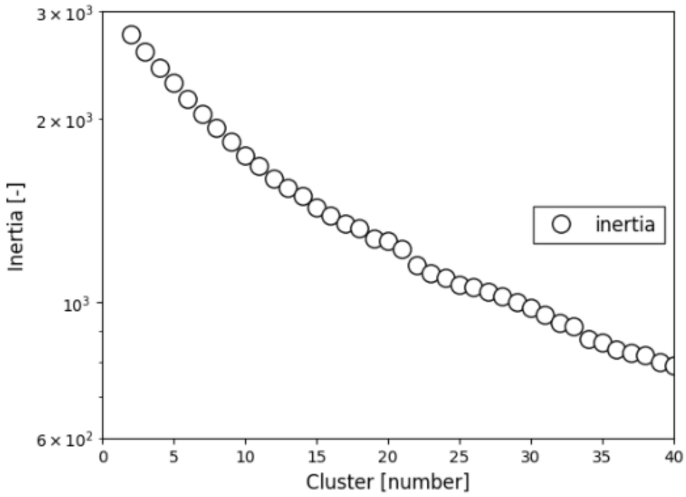

Fig. 4.4. Inertia of k-means method with different cluster numbers.

Fig. 4.4 shows that inertia decreases consistently as the number of clusters j increases. Since classifying by multi-clusters with small inertia is desirable in k-means method and the clusters of each image cannot be clearly defined when classifying into many clusters, hence, this study classifies with m=4 clusters.

The number of class and recalls $R_{r,j}$ of bubbly flow and slug flow, classified into m=4 clusters by k-means method with q=10 components obtained by PCA are shown in Table 4.3. Here, the recall $R_{r,j}$ is calculated as follows:

$$R_{r,j} = C_{r,j}/T_r \tag{4-5}$$

As shown in Table 4.3, the bubbly flow images are mostly classified into cluster 1, for slug flow images into clusters 0, 2, 3, and assuming that cluster 1 as bubbly flow and clusters 0, 2, 3 as slug flow, the recall for each flow regime is 75.2 % and 86.8 % respectively. Therefore, flow regime is identified through classification of upward gas-liquid two-phase flows flow regime by applying PCA and k-means methods to merged images derived from time strip method.

Table 4.3. Summary results of k-means method.

	Number of class of Bubbly flow [number] (Recall [-])	Number of class of Slug flow [number] (Recall [-])	Total number of cluster [number]
j= 0 cluster	0 (0)	15 (0.099)	15
j= 1 cluster	112 (0.752)	20 (0.132)	132
j= 2 cluster	0 (0)	22 (0.146)	22
j= 3 cluster	37 (0.248)	94 (0.623)	131
Total number of class (T_r) [number]	149	151	300

4.3.3 Classification of evaluation images including transition regions

The number of class and recalls of bubbly flow, slug flow, and evaluated images including transition regime, classified into m=4 clusters by GMM with q=10 components obtained by PCA are shown in Table 4.4. As shown in Table 4.4, the bubbly flow images are mostly classified into cluster 1, for slug flow images into clusters 0, 2, 3, and for evaluation images into clusters 0, 2. Assuming that cluster 1 as bubbly flow and clusters 0, 2, 3 as slug flow, the recall for each flow regime is 78.5 % and 97.3 % respectively, which is better than the classification accuracy of the k-means method. GMM has improved classification accuracy compared to the k-means method, due to the features of EM method which can complexly classify points distributed in a multidimensional space.

Table 4.4. Summary results of GMM with evaluation image.

	Number of class of Bubbly flow [number] (Recall [-])	Number of class of Slug flow [number] (Recall [-])	Number of class of Evaluation image [number] (Recall [-])	Total number of cluster [number]
j= 0 cluster	7 (0.047)	92 (0.609)	20 (0.417)	119
j= 1 cluster	117 (0.785)	4 (0.026)	7 (0.146)	128
j= 2 cluster	25 (0.168)	47 (0.311)	20 (0.417)	92
j= 3 cluster	0 (0)	8 (0.053)	1 (0.021)	9
Total number of class (T_r) [number]	149	151	48	348

In order to examine the flow regime transition, the results of evaluation images were organized into a flow regime map as shown in Fig. 4.5. This is the flow regime map of 2.8 MPaG pressure and 25.3 m elevation with developed upward gas-liquid two-phase flow.

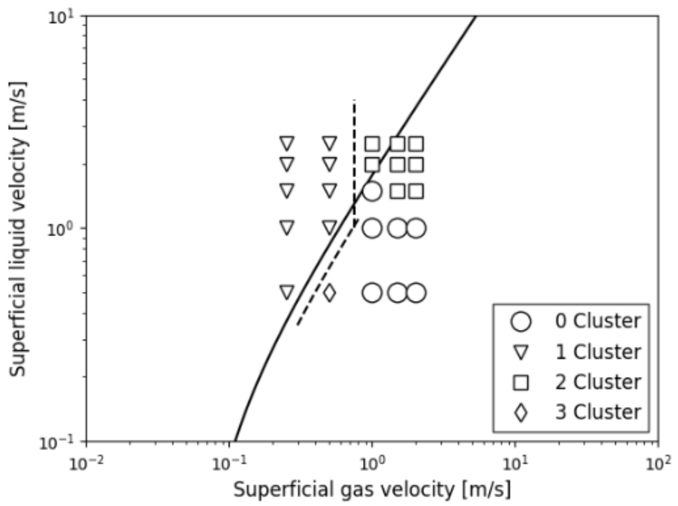

Fig. 4.5. Classification results of evaluation image in flow regime map.

In this chapter, Mishima-Ishii's flow regime transition criteria is also shown in Fig. 4.5 and the details are same as section 2.4.2. As shown in Fig. 4.5, each image is mostly classified into 0, 1, or 2 clusters, and each cluster has grouped in the region as follows: above j_g = 0.5 m/s and below j_f = 1.0 m/s for 0 cluster, below j_g = 0.5 m/s for 1 cluster, and above j_g = 0.5 m/s and above j_f = 1.0 m/s or higher for 2 cluster. Referring to the results in Table 4.4, cluster 1 and clusters 0, 2, 3 are analyzed as bubbly and slug flow respectively, indicating the flow regime transits between the dott line shown in Fig. 4.5. This result is in good correlation with the Mishima-Ishii transition equation shown in the figure, except for the j_g = 1.0 m/s above j_f = 2.0 m/s.

Here, the merged image of j_f = 2.5 m/s, j_g = 1.0 m/s are shown in Fig. 4.6. In this image, the projected light from the back is periodically appearing, although continuous bubbles, which is the feature of bubbly flow, are also shown. Thus, the image is classified as the intermittent of Taylor bubbles (Shibata et al., 2021), which is the feature of slug flow.

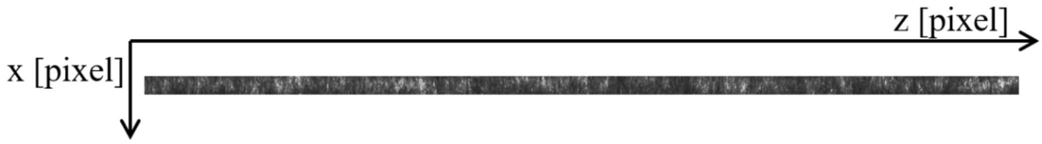

Fig. 4.6. Evaluation image of j_f =2.5 m/s, j_g =1.0 m/s condition (right as top).

The attribution probability for bubbly or slug flow when the gas superficial velocities are increased under fixed liquid superficial velocity j_f = 0.5 - 2.5 m/s, are shown in Fig. 4.7. Since, the GMM output the probability of attribution to 1 - 4 clusters for each image, the attribution probabilities of bubbly and slug flows is calculated by summing the probabilities attributed to the 0, 2, and 3 clusters for each image, as the 1 or 0, 2, 3 clusters are aggregation of bubbly or slug flows according to Table 6. As shown in Fig. 4.7, when the superficial liquid velocity is fixed, the precision of bubbly flow identification is higher at lower superficial gas velocity, and that of slug flow rises with the decrease of bubbly flow as superficial gas velocity increases for all conditions. If the transition state is defined as a result where the probability of both bubbly and slug flow are less than 90%, the conditions j_f = 1.0 m/s and j_g = 0.5 m/s is transition state and the transition region is considered as j_g = 0.25 - 1.0 m/s for the j_f = 1.0 m/s condition. Similarly, Zhang et al. (2017) have conducted the study of transition from bubbly to slug flow. The study has shown that the slip ratio has minimum in the transition from bubble flow to slug flow which corresponds to transition boundary and the slug flow is first observed as the slip ratio increases, when liquid superficial velocity is fixed and gas superficial velocity increases. When the transition region is defined as from the minimum to where the slug flow is first observed, the transition region is j_g = 0.56 - 0.74 m/s for j_f = 0.64 m/s and the range expands as the liquid superficial velocity increases. The present results are similar with those of Zhang et al. and suggest that the transition region is wide due to the high liquid superficial velocity.

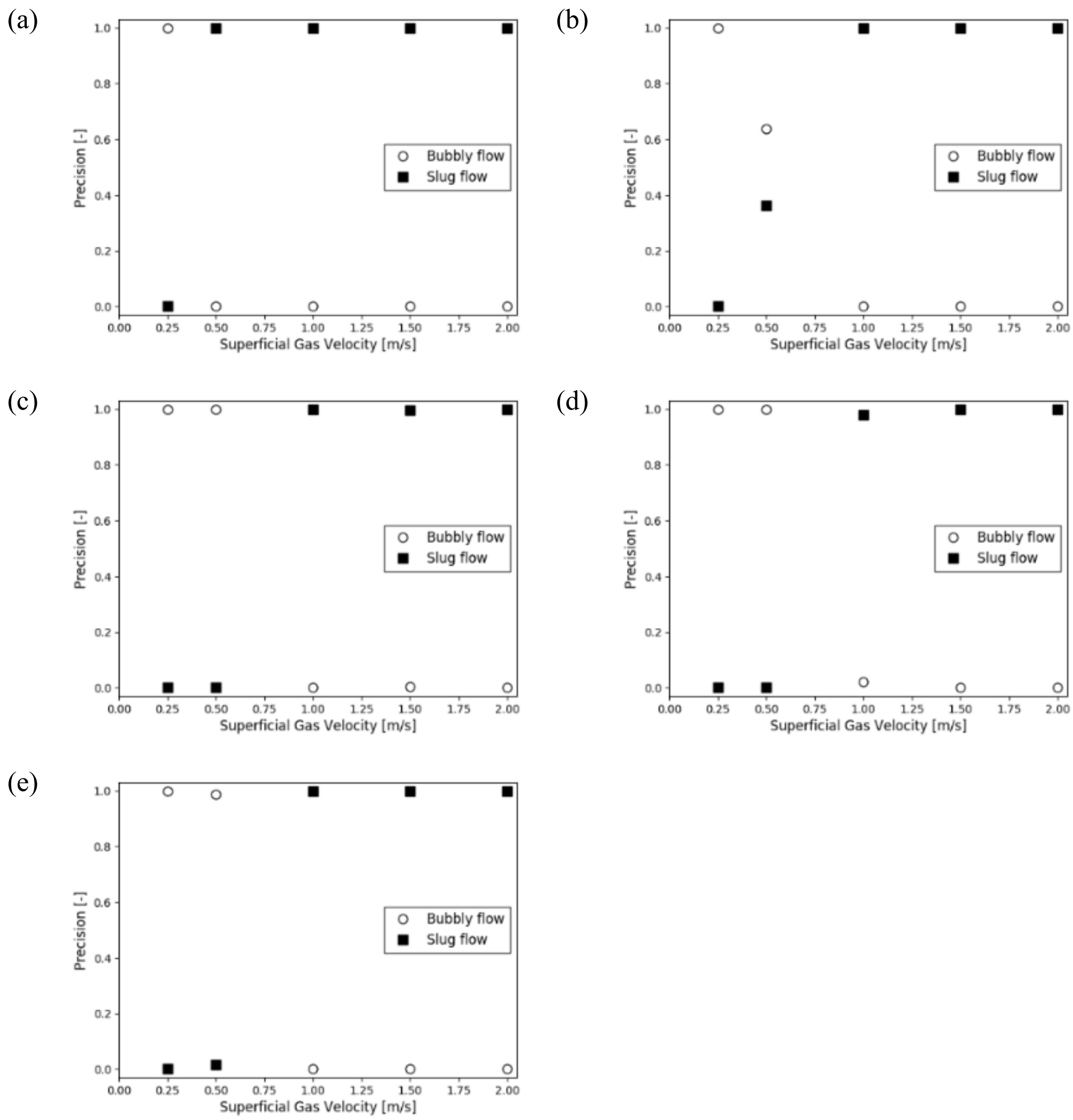

Fig. 4.7. Probability of affiliation to the specific flow regime for j_f =(a) 0.5 m/s, (b) 1.0 m/s, (c) 1.5 m/s, (d) 2.0 m/s and (e) 2.5 m/s.

The flow regime images defined as the transition state are shown in Fig. 4.8. As the image shows, the intermittency of slug flow is seen from the macroscopic view, while the continuous bubbles are shown from the microscopic view. Therefore, unsupervised learning is classifying flow regimes based on the features of the transition state.

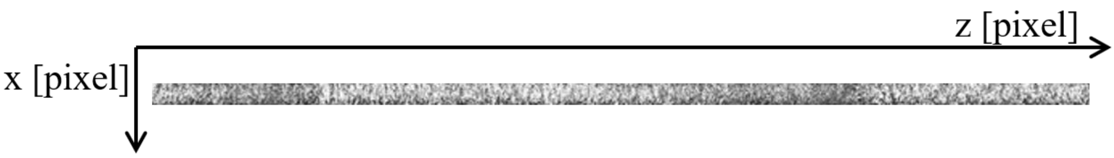

Fig. 4.8. Evaluation image of j_f =1.0 m/s, j_g =0.5 m/s classified as transition state (right as top).

4.4 Conclusion

In present chapter, the unsupervised learning PCA and k-means methods were applied to database images of flow regime which are merged into a single image by the time strip method. Also, the classification of flow regime including transition regime was performed by PCA and GMM, and the findings were as follows:

1. PCA has shown the difference of bubbly flow and slug flow as separate regions with the input of merged image.
2. The features necessary for classification can be improved by trimming unnecessary regions of the image input to PCA.
3. Bubbly and slug flow can be classified more than 72% recall with the present method.
4. The flow regime map derived with PCA and GMM results correlate well with Mishima-Ishii transition, except for certain conditions
5. Identified transition regimes in certain conditions based on present method quantification of flow regime transitions.

The present chapter has shown that the flow regime of upward gas-liquid two-phase flow under high-pressure can be identified with classification using unsupervised learning and merged images. Moreover, the flow regime transitions were quantified using unsupervised learning.

Bibliography

Borhani, N., Agostini, B., Thome, J.R., 2010. A novel time strip flow visualisation technique for investigation of intermittent dewetting and dryout in elongated bubble flow in a microchannel evaporator. International Journal of Heat and Mass Transfer 53, 4809–4818. https://doi.org/10.1016/j.ijheatmasstransfer.2010.06.011

Dempster, A.P., Laird, N.M., Rubin, D.B., 1977. Maximum Likelihood from Incomplete Data via the EM Algorithm. Journal of the Royal Statistical Society. Series B (Methodological) 39, 1–38.

Goda, R., Hayashi, K., Murase, M., Hosokawa, S., Tomiyama, A., 2019. Experimental study on interfacial and wall friction factors under counter-current flow limitation in vertical pipes with sharp-edged lower ends. Nuclear Engineering and Design 353, 110223. https://doi.org/10.1016/j.nucengdes.2019.110223

Jolliffe, I.T., 2002. Principal Component Analysis, 2nd ed, Springer Series in Statistics. Springer-Verlag, New York. https://doi.org/10.1007/b98835

Kazi, J., Mori, H., Fukuma, J., Hayashi, K., Kurimoto, R., Tomiyama, A., 2021. Flow Characteristics of Air-Water Two-Phase Flows in a Serpentine Tube. Japanese Journal of Multiphase Flow 35, 85–92. https://doi.org/10.3811/jjmf.2021.013

Kamishima, T., 2003. A survey of recent clustering methods for datamining. J. Jpn. Soc. Artificial Intelligence 18, 59–65.

MacQueen, J., 1967. Some methods for classification and analysis of multivariate observations. Proceedings of the Fifth Berkeley Symposium on Mathematical Statistics and Probability, Volume 1: Statistics 281–297.

Mishima, K., Ishii, M., 1984. Flow regime transition criteria for upward two-phase flow in vertical tubes. International Journal of Heat and Mass Transfer 27, 723–737. https://doi.org/10.1016/0017-9310(84)90142-X

Pan, L., Zhang, M., Ju, P., He, H., Ishii, M., 2016. Vertical co-current two-phase flow regime identification using fuzzy C-means clustering algorithm and ReliefF attribute weighting technique. International Journal of Heat and Mass Transfer 95, 393–404. https://doi.org/10.1016/j.ijheatmasstransfer.2015.11.081

Shibata, N., Miwa, S., Sawa, K., Takahashi, M., Murayama, T., Tenma, N., 2021. Identification of Upward Two-Phase Flow Regime Transition Region under High-Pressure Condition Using Deep Learning. Japanese Journal of Multiphase Flow 35, 93–100. https://doi.org/10.3811/jjmf.2021.014

Yu, G., Sapiro, G., Mallat, S., 2010. Solving Inverse Problems with Piecewise Linear Estimators: From Gaussian Mixture Models to Structured Sparsity. arXiv:1006.3056.

5 General Conclusion

The present study has conducted the foundation of nitrogen-brine two-phase flow behavior under low and high-pressure to contribute for the estimation of process condition. The study includes (1) void fraction and frictional pressure drop model and (2) objective flow regime identification method using machine learning technique. The achievements are summarized as follows.

In chapter 2, the void fraction and frictional pressure drop of nitrogen-brine two-phase flows through long channel length at high-pressure and high-superficial gas velocity were investigated. The present experimental conditions simulate the offshore methane hydrate production test. The experiment is conducted with j_g =0.25-3 m/s of inlet superficial gas velocity and superficial liquid velocity of j_f = 0.5-2.5 m/s under low and high pressure (0-2.8 MPaG) condition, and the elevation ranges from 2.7 - 25.3 m. The results of void fraction and frictional pressure drop were compared with conventional models and a new model for high-pressure brine is also developed with these results. The gas velocity in the bubbly flow regime determined by the void fraction from experiments was lower than the conventional model for all conditions under brine. With the inhibition of coalescence by brine, the gas velocity is lower because of the uniformity of bubble distribution and lower bubble rise velocity due to the reduction in bubble diameter. Thus, a new model with $C_0 = 1$ and $v_{gj}^{+} = u_b$ based on dimensionless drift flux model, is proposed. As for frictional pressure drop, the two-phase flow friction multiplier increases with elevated height, while decreases with increased system pressure, and the new model with Z' based on Chisholm parameter was developed to reflect these results. The flow regime has shown that the transitioning superficial gas velocity of bubbly to slug flow in brine is faster than tap water condition. This is due to the increase of critical void fraction that transits from bubbly to slug flow resulting from the decrease of bubble diameter caused by added salts.

In chapter 3, the flow regime identification method using the CNN model trained by a single merged image obtained from the time strip method was considered. In this study, deep learning, highly capable of identifying static images, was applied to processed images, capturing the dynamics of gas-liquid two-phase flow seen in the sequential images. The model is applicable for bubbly-slug transition at high-pressure two-phase flow conditions and its identification capability between bubbly flow and slug flow was investigated. Furthermore, quantifiable flow regime transition range was investigated using the identification precision values obtained from the present model. The results were compared with existing flow regime transition criteria proposed by Mishima-Ishii. The identification results in the transition region have quantitatively shown that the transition region exists for the bubbly to slug flow. It was found that the bubbly-slug transition region under fixed superficial gas velocity is wider than the fixed superficial liquid velocity condition. This imply that the flow regime transition occurs moderately at the larger superficial liquid velocity. The identification results showed larger j_g at flow regime transition region compared to Mishima-Ishii equation for some cases. This indicates that the critical void fraction for bubbly-slug transition is larger than the theoretical value of 0.3. In the current method, the identification rate became constant at the image length of 1600 pixels, which corresponds to 0.37 m in actual length. Since the minimum length of the measured slug unit was about the same, hence, it can be concluded that the identification performance for slug flow highly depends on the image length.

In chapter 4, the unsupervised learning PCA and k-means methods were applied to flow regime images derived by the time strip method. Also, the classification of flow regime including transition regime was performed by PCA and GMM. The results of PCA have shown the difference of bubbly flow and slug flow as separate regions with the input of merged image and the features necessary for classification can be improved by trimming unnecessary regions of the images. The flow regime transitions were quantified based on PCA and GMM results and the transition regimes in certain conditions were identified.

With these findings, nitrogen-brine two-phase flow behavior under low and high-pressure has partially found and established the baseline for stimulating the process conditions that reflects the flow behavior in the wellbore. Hence, the present study will contribute not only to the stable gas production through the proper specification and design of downhole and control equipment, but also to the progress of Multiphase flow engineering and to the design of many industrial systems including nuclear power plants.

List of Publications

Publications included in this thesis

Chapter 2

The void fraction and frictional pressure drop of upward two-phase flow under high pressure brine condition.
Shibata, N., Miwa, S., Sawa, K., Moriya, H., Takahashi, M., Murayama, T., Tenma, N.,
Chemical Engineering Science 268, 118399. 2023.

Chapter 3

Identification of high-pressure two-phase flow regime transition using image processing and deep learning.
Shibata, N., Miwa, S., Sawa, K., Takahashi, M., Murayama, T., Tenma, N.,
Journal of Natural Gas Science and Engineering 102, 104560. 2022.

Chapter 4

Unsupervised learning for classification of flow regime in high-pressure gas-liquid two-phase flow including transition region.
Shibata, N., Miwa, S., Sawa, K., Murayama, T., Takahashi, M., Tenma, N.,
Transactions of the JSME (in Japanese) 88, 21-00307-21–00307. 2022.